2014-01-01

Effect Of Multi-Tube Injector Geometry On Flame Stability And NOx Emission In A High Pressure Gas Turbine Combustor

Sudipa Sarker
University of Texas at El Paso, ssarker@miners.utep.edu

EFFECT OF MULTI-TUBE INJECTOR GEOMETRY ON FLAME STABILITY AND NO_X EMISSION IN A HIGH PRESSURE GAS TURBINE COMBUSTOR

SUDIPA SARKER

Environmental Science and Engineering

APPROVED:

Norman D. Love, Ph.D. ,Chair

Ahsan R. Choudhuri Ph.D., Co-Chair

Chintalapalle V. Ramana, Ph.D.

Jose Espiritu, Ph.D.

Bess Sirmon-Taylor, Ph.D.
Interim Dean of the Graduate School

Dedication

This dissertation is dedicated to all my family members

EFFECT OF MULTI-TUBE INJECTOR GEOMETRY ON FLAME STABILITY AND NO_X EMISSION IN A HIGH PRESSURE GAS TURBINE COMBUSTOR

by

SUDIPA SARKER

DISSERTATION

Presented to the Faculty of the Graduate School of

The University of Texas at El Paso

in Partial Fulfillment

of the Requirements

for the Degree of

DOCTOR OF PHILOSOPHY

Environmental Science and Engineering

THE UNIVERSITY OF TEXAS AT EL PASO

May 2014

Acknowledgements

At first I would like to express my gratitude to my supervisors Dr. Norman Love and Dr. Ahsan Choudhuri for allowing me the opportunity to work at cSETR. Dr. Norman Love always worked closely with me to enhance my technical expertise. I also earned valuable knowledge during working with him. I also like to thank my supervisors to give me financial support towards earning my PhD degree. I would like to thank to other committee members Dr. Chintalapalle V. Ramana, and Dr. Jose Espiritu for giving me their valuable suggestions and recommendations to make this dissertation possible.

A special thanks to the students of the Center for Space Exploration Technology Research (cSETR) who have also helped me to conducting my research: Jesus Nunez, Sergio Maldonado, Sarzina Hossain, Martin de la Torre. A portion of this work was supported by Mike Loya innovation fund.

Abstract

Future generation gas turbine combustors for power production are expected to have the capability of operating on high hydrogen content fuels. To ensure the implementation of high hydrogen content (HHC) fuel in a power generation unit without negotiating with operational or emission advantages, the study of the flame stability regime and behavior of (HHC) fuel under gas turbine condition leads to the necessity of the development of an optically accessible high-pressure combustor. This dissertation first presents the design of an optically high-pressure combustor facility based on 500 kW power and 1.5 MPa pressure which is the representative pressure of a real gas turbine. The combustion chamber is designed to accommodate multiple geometrical configurations including a non-swirl stabilized and center-body stabilized swirl flow. The combustor is made of stainless steel 410. It has four primary modular parts: outer stainless steel chamber, inner quartz chamber, front cap and end cap. It has three optically accessible windows and three instrumentation ports for a broad range of investigation techniques. Finite element analysis has performed to get the wall thickness. The test chamber is also fitted with a variable area flow restrictor to control the desired pressure across the combustion chamber. Cooling system is also included in the design to extract heat and avoid structural failure. The outer stainless steel chamber will be equipped with copper coiling using cooling water as a driving fluid and inner quartz chamber will be convectively cooled using nitrogen. The use of a variable throat area restrictor, multiple cooling systems, as well as removable modular sections and optical access will allow the combustor to be compatible to work in a wide range of operations and have the flexibility operating with variable syngas compositions. This will allow analysis of the flame stability, flow field characterization, pollutant emissions in high hydrogen content fuel under realistic gas turbine conditions.

The ignition and control systems of this high pressure combustor have also been developed in the present work. LabVIEW was used as the controlling interface that controls the proportional valves, and solenoiod valves. A modified spark plug was used as an ignition source. In order to ignite the main fuel-air stream, a diffusion flame was used. Functional test of the equipment, leak test and pressure testing were carried out prior to conducting the ignition experiments. The system has the capability to withstand the maximum pressure allowed by the air compressor which is 758 kPa.

The high-pressure combustion chamber design allows for testing in realistic gas turbine conditions. Fuels that show promise as an energy source are high-hydrogen content fuels derived from coal which have a much higher specific heat, higher diffusivity, flammability limits and higher laminar flame speed compared to other hydrocarbons. These properties induce flame flashback especially when the hydrogen content in the fuels is high. A multi-tube injector has been designed to mitigate the flashback of high hydrogen content fuel.

The present work studies the blowout characteristics of syngas mixtures emitted from a novel multi-tube injector. Compositions are varied for syngas from 10% to 30% hydrogen concentration by volume in carbon monoxide (CO). Three different conditions were tested for these compositions: 1) where jet velocity was greater than the laminar flame speed 2) where the jet velocity was equal to the flame speed and 3) where jet velocity was less than the laminar flame speed. Results were used to model the blowout behavior of the designed injector. The critical velocity gradient g_B which was defined as the ratio of laminar burning velocity to blow-off distance was used to make a correlation between blowout behavior of different syngas compositions. A dimensionless parameter, Peclet number, was used to capture the blowout

characteristics of the injector. Results showed that the degree of blowout tendencies decreased with increasing hydrogen concentration for this multi-tube injector. The Peclet model showed a good agreement yielding approximately similar correlation constants for different syngas compositions at different conditions. A cold flow numerical simulation of the designed multi–tube injector was also done to characterize the fluid flow behavior of the injector and assist in the present and future design of similar injector systems. Also presented in this paper is a numerical simulation of NOx emission. The models used for syngas fuel combustion consist of the k-ε model for turbulent flow, mixture fractions/PDF model for partially premixed premixed gas combustion, and P-1 radiation model. Numerical results revealed the flame location and maximum NOx emission values of 4, 42 and 52 ppm were measured at an equivalence ratio of 0.5, 0.75 and 1 respectively.

Table of Contents

List of Figures

List of Tables

Chapter 1 : Introduction and Background

1.1 Introduction: The growing concern of reducing emissions of NO_x, CO and CO_2 that are emitted during power generation is a key issue to counteract the effect of global warming which has led to the interest for the development of low emission combustion systems. It is expected that over the next 10 to 20 years, the demand of power will increase dramatically because of population growth and economic expansion. Based on these issues, future generation gas turbine combustors are expected to operate with fuel compositions ranging from natural gas to different syngas compositions. Approximately half of the electricity generated in United States comes from the coal –fired power plants. According to Defense of Energy fact sheet, coal is abundant and relatively inexpensive, however contains a large number of impurities. Coal-fired power plants emit 66% of sulfur oxides (SO_x, or acid rain), 40% of carbon dioxide (CO_2), 33% of mercury and 22% of nitrogen oxides (NO_x) and emit 3 pound of CO_2 for every pound of coal burned. Coal, biomass, or waste products can be used in power generation systems to produce low emissions with the development of advanced technologies which can be achieved through the Integrated Gasification Combined Cycle (IGCC). To produce synthetic gas, different types of gasifiers are used to gasify the solid fuels (coal, biomass or waste products). Gasifiers convert coal and oxygen into synthesis gas. After gasification, hot syngas is cleaned to remove sulfur compounds, mercury and particulate matters. The clean syngas is used to fuel a combustion turbine generator which produces electricity. The heat from the exhaust gases is recovered to generate additional steam. Both this steam and the steam from the syngas process then drive a steam turbine generator to produce additional electricity. Using different gasification process

technologies, the IGCC systems can produce syngas fuel with different compositions from solid fuel feedstock.

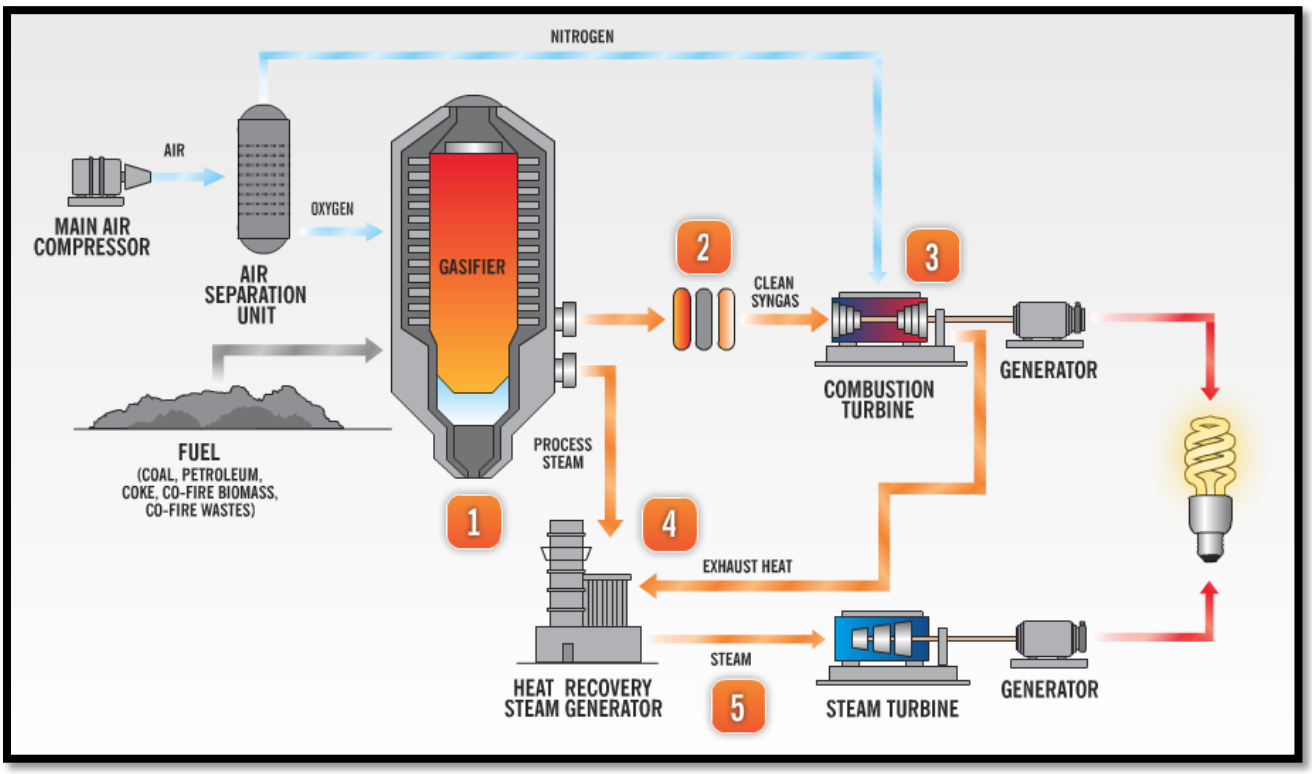

Figure 1.1 : working principle of IGCC power plant [Edwardsport Integrated Gasification Combined Cycle plant]

1.2 Fuel variability: Generally gas turbines are designed to be fueled with natural gas and coal. In this respect it brings certain challenges regarding the efficient burning of syngas fuel with different chemical compositions. Combustion dynamics of the flame depend on the compositions of the fuel, geometry of combustor, equivalence ratio, temperature and pressure. Fuel variability greatly changes the flame characteristics like flame speed, flame shape, flame stability and the variation of these properties may bring some drawbacks such as flashback,

blow-off, and instabilities. It is very important to study the combustion characteristics of various fuels in order to understand the impact of fuel in gas turbine combustor.

There are three important parameters that influence the properties of flame stability: firing input, hydrogen content and extinction characteristics. Combustion dynamics of fuels are also greatly related to these properties. The extinction limit determines the flammability range of the combustion of the fuel. Figure 1.2 shows the impact of hydrogen and carbon mono oxide on the burning velocity of gas mixtures.

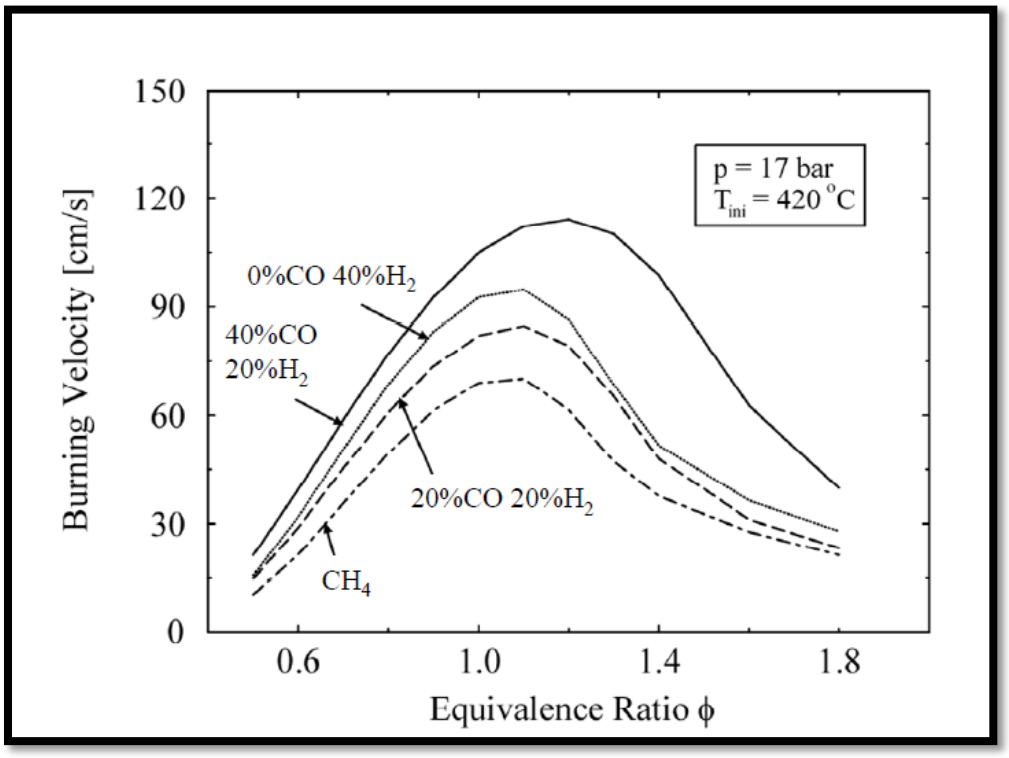

Figure 1.2: Burning velocities of various fuel mixtures compared to methane [Mcmillan et al., 2008]

Compared to other hydrocarbons, hydrogen content fuels behave differently because of much higher specific heat, higher diffusivity, and flammability limits which means hydrogen has a

wide range of volume concentrations over which it is flammable, and a higher laminar flame speed. These properties induce the flashback in case of high hydrogen content fuel.

1.2.1 Flashback: During flashback, the flame propagates upstream into the premixing section which causes hardware damage, unsafe operating conditions and increased pollutant emissions. Settlemayer et al. (2003, 2004) discussed a number of flashback modes taking place in a swirl stabilized lean premixed turbine combustor. Flashback occurs due to boundary layer flame propagation, turbulent flame propagation, combustion instabilities and combustion induced vortex breakdown (CIVB). In the case of boundary layer flame propagation, the flame propagates upstream when its normal burning velocity exceeds the local flow velocity. This type of flashback generally occurs close to the wall where a no slip boundary condition exists. CIVB flashback occurs due to complex interactions of flow field, heat release processes. Fuel composition, unburned mixture conditions, local stoichiometry strongly influences the CIVB flashback behavior. Ardha et al. (2011) found that a main challenge is the concentrations of hydrogen which have been shown to significantly affect flame characteristics even when only 5% vol. hydrogen is present. Some fundamental characteristics of flame of these fuels such as laminar flame speed, flame stability, and emissions characteristics have been investigated in some other studies. Davu et al. (2005) showed that although flame velocity and stoichiometry are generally the main reasons for flashback for hydrocarbon blends, the kinetics of the hydrogen dominates the flashback characteristics of syngas fuels where the experiments were done using a tubular burner. To analyze the influence of flow field and chemistry on flame flashback, Dam et al. (2011) did some experiments using a center-body swirl stabilized lab-scale gas turbine

combustor with similar fuel compositions and found that the percentage of H_2 in the fuel mixture rather than increasing swirl number influenced flame flashback more.

1.2.2 Lean combustion and NO_x emission: In order to prevent flame flashback and reduce NO_x three basic concepts have been experimentally studied earlier for fuel lean combustion: lean-premixed prevaporized (LPP), the rich-burn/quick-quench/lean-burn (RQL), and the lean-direct-injection (LDI) combustors. These concepts are shown in Figs 1.3 and 1.4.

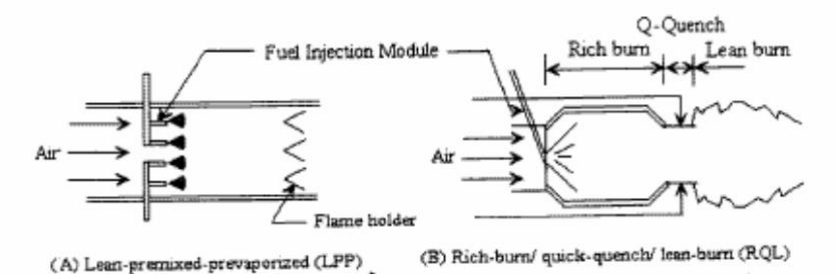

Figure 1.3: Sketches of LPP, RQL and LDI Combustor

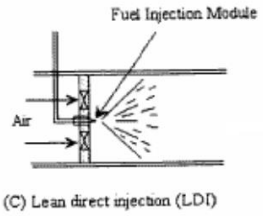

Figure 1.4 : and LDI Combustor

According to Ripplinger et al. (1998) and Cai et al. (2002), auto-ignition and flashback in the premixed zone are potential disadvantages of a LPP system. Compared with LPP, overall NOx emissions of RQL are higher because of the stoichiometric temperatures and production of NOx during the quench step. Since in the LDI system fuel is directly injected into the burning zone, it has an advantage in that it prevents flashback and auto-ignition. As there is no premixed section

in the LDI concept, it is necessary ensure uniform and quick mixing of fuel and air in order to produce lower flame temperature which facilitates lower NOx emission.

1.3 Background

1.3.1 Design of the optically accessible high-pressure combustor

Sato et al. (1988) used a combustion chamber which is basically a cylindrical section with an inner diameter of 500 mm and a length of 600 mm. Removable electric heater is used for ignition and combustion tests. The combustor has nine optical windows on the chamber walls to observe the combustion and fuel spray. Operational pressure ranges from ambient gas pressures up to 20 MPa and temperature up to 900 K. The fuel spray system in this facility includes high pressure pump, accumulator, and fuel injection rate control unit and solenoid valves.

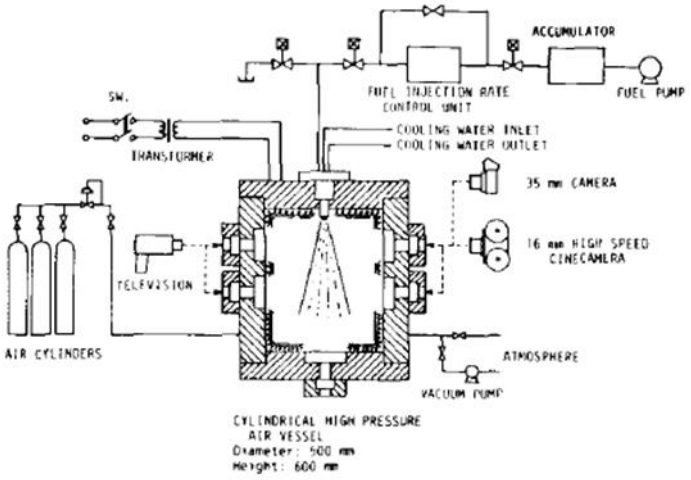

Figure 1.5: Schematic of experimental apparatus [Sato et al., 1988]

In Frank et al. (1995), the authors developed an optically accessible combustor for planar laser induced fluorescence measurements. The combustor utilizes commercial styled gas-turbine fuel

injectors and has the capability of operating at pressures up to 50 MPa. Current work has been limited to operating at 2 MPa with a maximum flow rate of 0.4 kg/s. The combustor design consists of four main components: a pressure vessel with inlet and exhaust flanges, fuel injection support and linear system, water cooled exhaust orifice, and a water cooled exhaust test section. The combustion gases are contained using a ceramic liner that protects the chamber from the heat load of the flame. The region between the liner and outer pressure vessel is purged with nitrogen flow. As the exhaust gas exists the chamber, it is water cooled in the exhaust section.

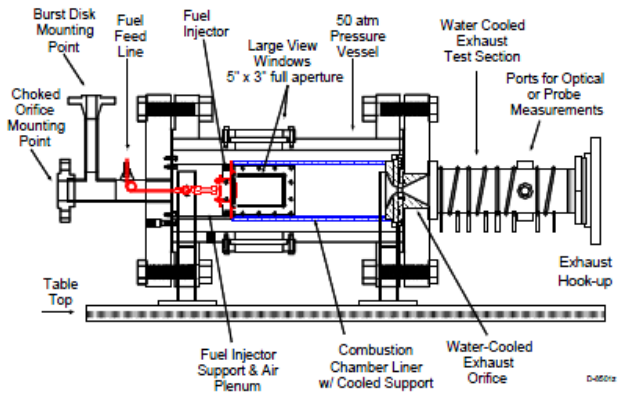

Figure 1.6: Diagram of the high-pressure combustor assembly [Frank et al., 1995]

Tomezak et al. (2002) used a combustor that can operate under duel fuel operation (liquid and gaseous) allowing 1MPa Pressure. An axial swirler device was used operating with 8 holes for fuel injection. The test rig consists of an alloy steel pressure vessel, designed in modular form, utilizing a lamination valve at the exit to control the pressure in the combustor.

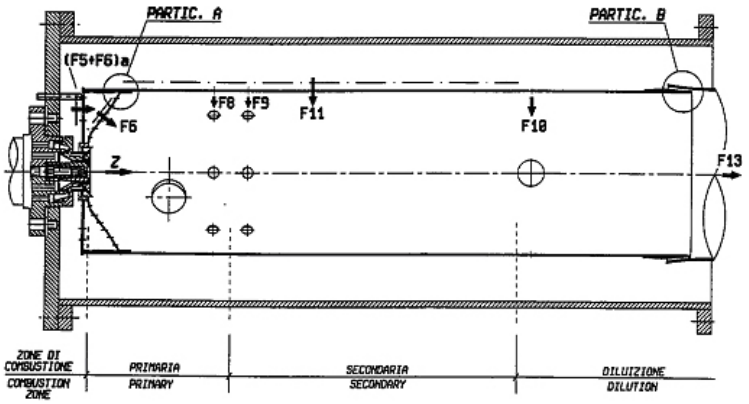

Figure 1.7 : Reverse-flow combustion system [Tomezak et al., 2002]

The flame is stabilized using a combination of a swirler as well as recirculation of air. The test rig consists of an alloy steel pressure vessel, designed in modular form, utilizing a lamination valve at the exit to control the pressure in the combustor. The combustor metal temperature, air flow, and burner exit temperatures are recorded using thermocouples with an operating range of 400 to 1200 °C. The use of pressure taps is also implemented to monitor pressure drops and high frequency response pressure transducers to measure pressure fluctuation.

Lieuwen et al. (2007) used a facility consisting of three main sections: inlet/premixer, combustor, exhaust. The easy removal of center body and swirler makes the nozzle modular. The nozzle ends up with the square combustor followed by an exhaust section that is water-cooled. An adjustable bypass valve is used to maintain the desired combustor pressure.

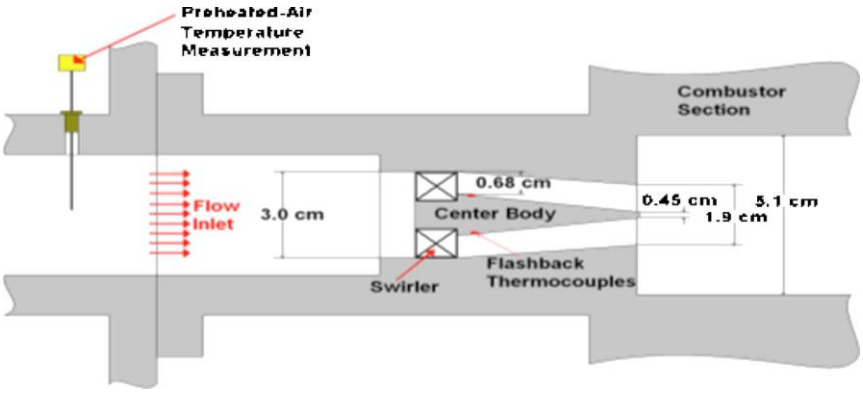

Figure 1.8: Cross section of premixer assembly [Lieuwen et al., 2007]

Jansohn et al. (2010) used a high pressure combustor rated up to 500 kW of thermal power, 2000 K temperature and pressure 3 MPa with maximum airflow rate of 0.3 kg/sec. The combustor also contained an inner cylindrical liner consisting of two coaxial quartz glass tubes that are convectively cooled by air. A hydrogen torch igniter was used to ignite the premixed air/fuel mixture.

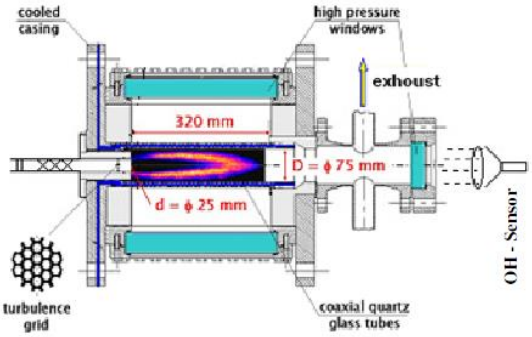

Figure 1.9: High-pressure combustor with OH-Chemiluminescence sensor [Jansohn et al., 2010]

Currently, there is an operational optically accessible combustor operating under ambient conditions at cSETR, UTEP. Some of the design parameters of the high pressure combustor presented in this dissertation have been taken from this atmospheric combustor.

Figure 1.10: Atmospheric combustior facility at cSETR [Dam et al., 2011]

The combustor rig has three configurable modules: (i) inlet manifold with static mixture, (ii) swirl burner with mixing tube, and (iii) optically accessible combustion chamber.The swirl burner module is fitted with three quartz windows that are needed for the high speed imaging of flashback inside the premixer. To ensure proper mixing of air and fuel, the fuel and air enter the inlet manifold through five alternate injection holes and then passes through the static mixture section. The burner module can accommodate both centerbody and hubless swirlers.

The Cambridge Intermediate Pressure Combustion Facility (CIPCF) has been designed to operate up to 873 K temperature, pressures of up to 1 MPa and air mass flow rates through the injector of up to 0.7 kg/s at full pressure. The current combustor section consists of a 200 mm long, 135 mm diameter inner shell surrounded by cooling air inside a pressure vessel. Full optical access is provided through 100 mm square windows at three right angles that allow a

whole range of laser imaging diagnostics to be used. Basically, the facility is equipped for liquid fuels, but bottled gaseous fuels can be accommodated as well.

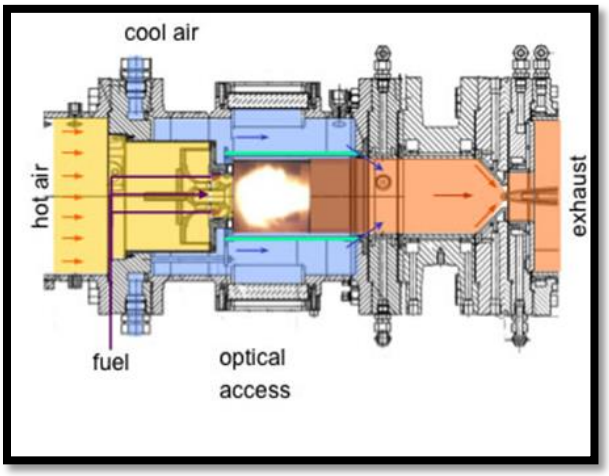

Figure 1.11: High pressure combustion facility [Cambridge Intermediate Pressure Combustion Facility]

Two pressure vessels are available at the University of California Irvine Combustion Laboratory (UCICL) that features similar capabilities. The first facility has been used for a variety of high pressure spray and combustor experiments. It also features significant optical access along with full traversing, allowing detailed in-situ measurements to be obtained. No traversing has also been developed for the second facility which also has less optical access over the past decade with the purpose of providing long duration reacting experiments for exposure testing and durability evaluations. This facility can also serve as a combustion performance test rig (e.g., Emissions and stability assessment).

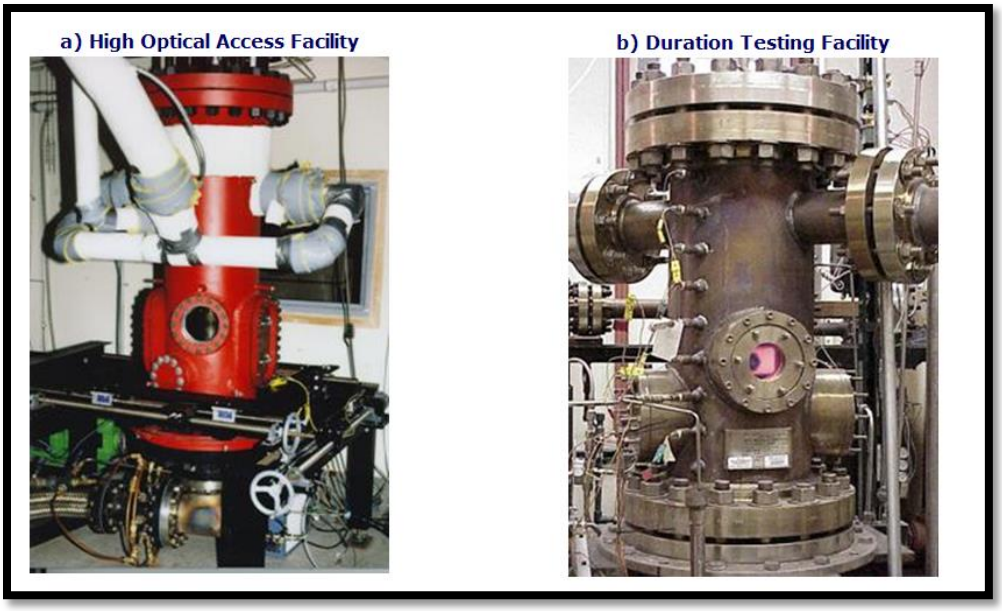

Figure 1.12: Elevated pressure facility [University Of California Irvine Combustion Facility]

The operation of the vessels is maintained by the facility control system. The control system is used to route fuel and/or air flows to either vessel that controls air flow rates up to 1.0 kg/sec, pressures of 1.5 MPa, and temperatures up to 649°C (1200°F) and this facility can also provide a high-pressure supply of liquid fuel and natural gas.

The National Energy Technology Laboratory (NETL) has two operational high-pressure combustor facilities. One is a dynamic gas turbine test rig with optical access and operating pressures of up to 1 MPa and air flow of 0.75 kg/s which is capable of running both natural gas and liquid fuels. The second combustion facility (SimVal Test Rig) has optically accessible combustor allowing the mass flow rate of maximum 1.4 kg/s combustion air, 53.5 g/s natural gas, 5.4 g/s hydrogen and pressure of 2.2 MPa and maximum temperature of 700 K and it is used for computational fluid dynamic testing and modeling of combustion.

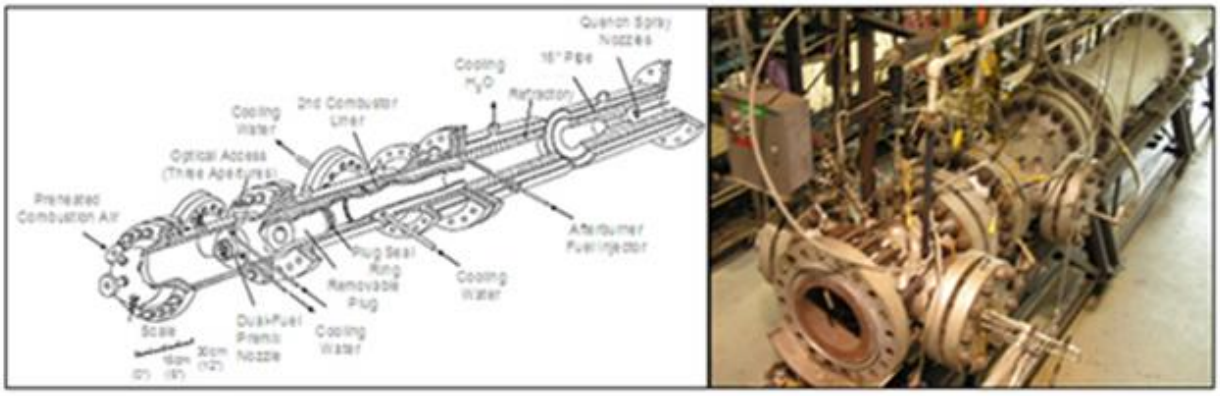

Figure 1.13: Dynamic Gas Turbine Combustion Test Rig (cross-section) [NETL]

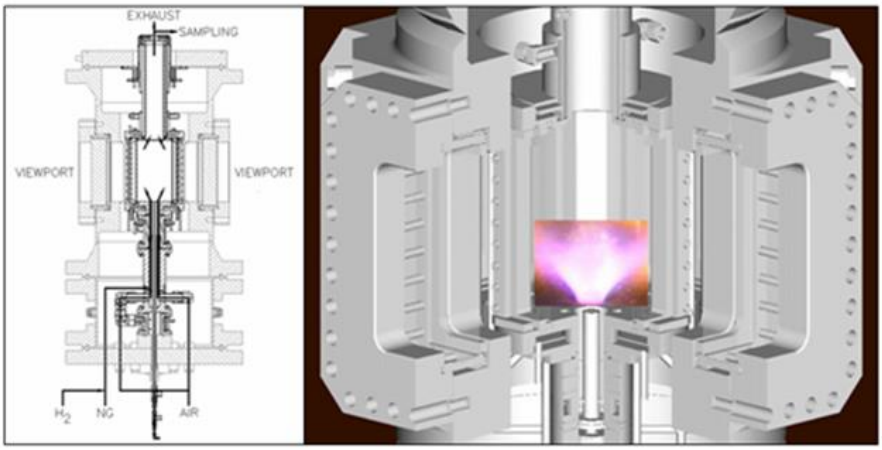

Figure 1.14: SimVal Test Rig (cross-sections) [NETL]

Pennsylvania State University's High Pressure Combustion Lab performs a wide variety of experimental testing and theoretical analyses for the characterization of combustion behavior of energetic materials. Three stand burners are available to test these solid propellants. The Solid Propellant Strand Burner (SPSB) is a windowed chamber which allows the imaging of the burning strand at pressure up to 65.5 MPa along with the temperature ranging from -80 °C to 80°C .The Ultra High Pressure Strand Burner is used for pressures up to 206.8 MPa. A double -

ended windowed strand chamber is used for controlling the gap width between the two adjacent burning propellants.

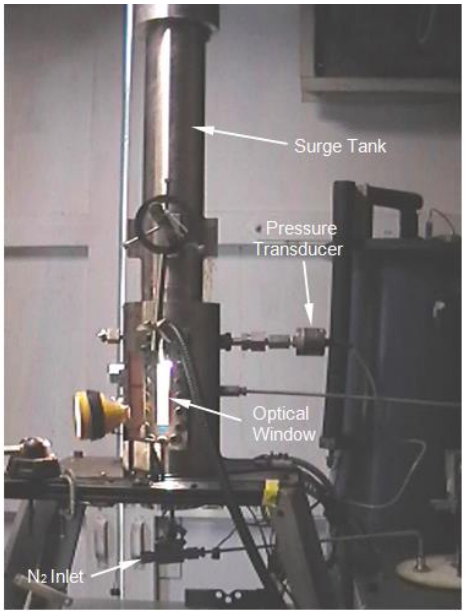

Figure 1.15: Solid Propellant Strand Burner at the HPCL [Pennsylvania State University's High Pressure combustor]

Figure 1.16: Double-Ended-Windowed Strand Burner at the HPCL, and opposing burning solid propellants [Pennsylvania State University's High Pressure combustor]

1.3.2 Flashback and blow out of syngas:

R. W. Schefer (2001) studied a premixed swirl-stabilized flame in order to determine the stability characteristics after hydrogen addition under fuel-lean conditions. The burner consisted of a centerbody with an annular, premixed methane/air jet. A swirler with 45-degree vanes was used for introducing the swirl to the flow. Combustion was carried out within an air-cooled quartz chamber at atmospheric pressure. PLIF measurements of the OH radical were used to understand the effects of hydrogen enrichment on methane flames close to lean blow out where instantaneous and time-averaged data were measured. The addition of hydrogen to the fuel lowered the lean stability limit. The improved stability with hydrogen enrichment is speculated to be a direct result of increasing H, O, and OH radical concentrations that increases several key reaction rates. Results showed that a significant increase in the OH radical concentrations was obtained by using moderate amounts of hydrogen enrichment. Though the addition of up to 13.8% hydrogen causes a 44% increase in the maximum OH concentration, further increases result in partly higher radical concentrations for the conditions tested.

Tomezak et al. (2002) investigated a gas turbine combustion system fired with mixtures of natural gas and hydrogen. The main objective was to analyze hydrogen flame features and on its behavior in order to make adjustments and modulations of gas turbine combustion processes and to verify operability and environmental aspects. Numerical and experimental results are completely aligned with the general thermodynamic aspects. Better flame stabilities have been confirmed along with the tendencies of NO_x and CO pollutant emission. High NO_X emission was measured at the combustor outlet. Pure hydrogen leads to the design of a new combustion system including NO_X emission reduction techniques.

Bell et al. (2006) numerically studied the Lewis number effect on non-premixed turbulent flames where they studied hydrogen, methane and propane flames. Experimental results suggest that simulations were able to capture the basic structure of the flames. Local burning rate in the methane flame were relatively insensitive to the flame curvature compared to propane and hydrogen flames. Burning was enhanced in regions of large negative curvature indicating that the flame is thermo- diffusively stable. Unstable hydrogen flame burning was enhanced in regions of positive curvature for the thermo-diffusivity and showed pockets of local extinction when curvature is negative that lead to the formation of breaks in the flame surface. Rather than reignite, the extinction regions participated to form a single pocket.

Noble et al. (2006) reported experimental data on flashback and lean blowout characteristics of $H_2/CO/CH_4$ mixtures. Data were analyzed over a wide range of fuel compositions up to 4.4 atm and 470 K inlet reactant temperature. Results showed that blowout characteristic can be captured by using classical Damköhler number. Two different flashback mechanisms were observed in this paper- rapid flashback into the premixer and movement of the static flame position towards upstream along the cenetrbody. Results also showed that flashback can also occur even though the flame speed is not enough to propagate upstream because flame can be reinforced by the region of vortex breakdown imposing an adverse pressure gradient ahead of the flame

Bouvet et al. (2007) investigated the flame speed characteristics of Syngas (H_2-CO) with straight burners for laminar premixed flames. A study of laminar flame speeds of undiluted syngas (H_2/CO) mixtures was studied at atmospheric conditions using chemiluminescence and Schlieren

techniques for a straight cylindrical burner apparatus. A wide range of mixture compositions, from pure H_2 to 1/99 % H_2/CO was investigated for lean premixed syngas flames. In order to achieve a better flame stabilization and reduce flame flashback propensity, two nozzle burners of different sizes were designed and fabricated for further studies. Laminar flame speeds of various syngas mixtures were compared to results from predictions of recent syngas mechanisms. For mixtures with higher hydrogen contents, flame flashback and flame tip opening phenomena strongly limited the equivalence ratio range for investigation at ultra-lean condition.

Zhang et al. (2007) described the measurements of the dependence of lean blowout limits upon fuel composition for H_2 /CO/CH_4 mixtures. Blowout limits were obtained at fixed flow velocity, reactant temperature, and combustor pressure at different conditions. Results showed that the percentage of H_2 in the fuel drives the mixture blowout characteristics. That means flames can be stabilized at lower equivalence ratios, adiabatic flame temperatures, and laminar flame speeds with increasing H_2 percentage. Additionally, the blow off phenomenology qualitatively changes with hydrogen levels in the fuel. It was observed that the effects of fuel composition variability on blow off limits can be captured by standard well stirred reactor based correlations, based upon a Damköhler number with a diffusivity ratio correction.

Daniele et al. (2009) have done the experimental investigation of lean blow out (LBO) limits, NO_x emissions, and turbulent flame speed for lean premixed syngas/air flames in a generic combustor. The experiments were performed for a wide range of parameters including an inlet velocity varying from 40 to 80 m/s, operating pressures between 5 and 15 bar and adiabatic flame temperatures up to 1950 K. Results show that at leaner condition, the higher amount of H_2

in the fuel mixture induces LBO flame extinction. The NO_x emissions of all fuel mixtures were found to be exponentially dependent on the adiabatic flame temperature. Syngas mixture coupled with methane showed significantly lower NO_x emissions.

Hu et al. (2009) carried out experimental and numerical study on laminar burning velocities and flame instabilities of hydrogen–air mixtures at elevated pressures and temperatures. Laminar burning velocity increases for fuel-lean mixture combustion and decreases in the case of fuel-rich mixture combustion for the increase of equivalence ratio. The maximum value of laminar burning velocity was presented at the equivalence ratio of 1.8. With the increase of dilution ratio, laminar burning velocity decreases, and the position of peak value of laminar burning velocity move slightly to the lean mixture direction. With the increase of equivalence ratio, the flame stability was increased and Markstein length increased monotonously with the increase of equivalence ratio and slightly decreased with the increase of dilution ratio. Laminar burning velocity increased as the initial temperature increased and decreased with the increase of initial pressure. With the increase of initial pressure, advancement of onset of cellular instability was presented and Markstein lengths were decreased, indicating the increase of hydrodynamic instability with the increase of initial pressure. Suppression (or enhancement) of overall chemical reaction with the increase of initial pressure temperature was because of the decrease/ increase of H and OH mole fractions in flames. Strong correlations existed between laminar burning velocity and maximum radical concentrations of H and OH radicals in the reaction zone of premixed flames. High laminar burning velocity corresponds to high radical concentration in the reaction zone.

Wang et al. (2009) carried out the numerical study of the effect of hydrogen addition on methane–air mixtures combustion. PREMIX code in CHEMKIN II programmed with GRI-Mech 3.0 was used to calculate the stoichiometric methane–hydrogen–air flame as it freely propagated laminar premixed flames. The effect of hydrogen addition on methane–air combustion was examined by rate of production analysis of the selected species. The potential of emission reduction with addition of hydrogen to methane was analyzed. The promotion of chemical reaction with hydrogen addition was observed due to the increase of H, O and OH mole fractions in the flame. The mole fraction of CH_2O and CH_3CHO was decreased because of the addition of hydrogen which gives a potential to reduce the aldehydes emissions of methane combustion with hydrogen addition. As hydrogen was added, the methane oxidation reaction paths move toward the lower carbon reaction path that gives a great potential to reduce the soot formation and chemical kinetics effect of hydrogen addition has a little influence on NO formation of methane combustion.

Chaouki Ghenai (2010) investigated the numerical simulation of the combustion of syngas fuel mixture in gas turbine can combustor. They studied the impact of the variability in the alternative fuel composition and heating value on combustion performance and emissions. The composition of the fuel burned in can combustor was natural gas (methane) and syngas fuel with hydrogen to carbon monoxide (H_2/CO) volume ratio ranging from 0.63 to 2.36. The computational model used for syngas fuel combustion consists of the k-ε model for turbulent flow, mixture fractions/PDF model for non-premixed gas combustion, and P-1 radiation model. The gas temperature for all syngas compositions showed a lower gas temperature compared to the temperature of methane where the gas temperature reduction depends on the lower heating value

and the combustible constituents (hydrogen, carbon monoxide, and methane) and non-combustibles (inert) constituents in the syngas fuel. When methane was replaced with syngas fuel, results showed a reduction (30% to 49%) of CO_2 mass fraction at the exit of the can combustor.

Daniele et al. (2010) investigated the flashback propensity for syngas mixtures at operative conditions typical for gas turbine applications. The boundary layer flashback mechanism was used for the actual experimental configuration. Dependence of flashback on pressure, inlet temperature and inlet velocity was described. The results showed strong pressure dependence; the pressure trend narrowed dramatically the operational window for high pressures. Flashback propensity was found almost independent of bulk velocity. Reduction of the inlet temperature was identified as an effective step to mitigate flashback propensity. A local reduction of the inlet temperature is particularly suggested for syngas applications. This paper also reported the architecture and the logic of an automatic control system for flashback. The control system showed fast response and capability of avoiding damages which controls the back propagation of the flame by reestablishing it in the combustion chamber without the need of shutting down the rig.

Wang et al. (2010) investigated the effect of hydrogen addition on early flame growth of lean burn natural gas–air mixtures experimentally and numerically. They used a constant volume vessel and schlieren photographic technique in order to obtain the propagating photos of premixed combustion and direct-injection combustion. Different hydrogen fractions (from 0% to 40% in volumetric fraction) at overall equivalence ratio of 0.6 and 0.8, respectively were used to

get pressure derived initial combustion The results showed that as hydrogen is added to natural gas, the initial combustion process of lean burn natural gas–air mixtures was enhanced for both premixed combustion and direct-injection combustion. Hydrogen addition enhanced the initial combustion process significantly for both laminar premixed and direct-injection turbulent combustion at lean mixture condition. The OH and O mole fraction is increased by hydrogen addition and the position of maximum OH and O mole fraction moves close to the unburned mixture side. Spark ignition enhancement of lean natural gas–air mixtures with hydrogen addition can be attributed to the increase of OH and O mole fraction in the flames.

Dam et al. (2011) investigated the flashback propensity of syngas fuels. Results showed that with the increase in H_2 content in the mixture, boundary layer flashback propensity of H_2–CO and H_2–CH_4 flames changes nonlinearly. In fuel rich mixtures, with the increase in H_2 concentration, H_2–CO flames flashback propensity g_f values increase abruptly. An increase of H_2 in the mixture for fuel mixtures above 9% concentration did not affect the critical boundary velocity gradient significantly. A higher order g_F vs. (SL, α) scaling formulation was used to capture both fuel and burner effects.

Yousefian et al. (2011) carried out a numerical investigation of extinction limits (quenching and blow-off) and laminar flame speed for synthetic gas (syngas) premixed flame structure. These properties are important for the design and modeling of gas turbines combustion chambers and burners. Variations in syngas composition, the content of its dilution, and operating condition have direct impact on engine performance. The counterflow premixed flame model was used for calculation of extinction limits. Laminar flame speed was calculated by using the PREMIX code and OPPDIF code for estimation of quenching and blow-off limits. With an increase in reactant

preheat temperatures, the laminar flame speed rises significantly. Addition of nitrogen decreases the laminar flame speed. For extinction limits calculations, at high strain rates, the maximum flame temperatures increase and the blow-off limits are extended to higher strain rates because of increased inlet temperatures. Results indicate that blow-off limit is extended for is higher ambient pressure. Since at higher pressure, the molar concentrations of reactive species are larger, the overall reaction rate is increased. The effects of CO_2 addition is important as dilute effect, chemical effect, and radiation effect. Nitrogen plays a role as a passive diluent and its addition decreases the extension of blow-off and quenching limits.

Eichler et al. (2012) measured turbulent boundary layer flashback limits for fully premixed hydrogen-air flames at atmospheric mixture temperature and pressure for different geometrical configurations. The velocity gradients at the wall during flashback were analyzed as a measure for the critical boundary layer state. At the time of stable operation, the results for a tube burner with an unconfined flame burning into the free atmosphere agreed well to literature results obtained. For second set of experiments, the safety-critical situation of a confined flame burning inside the duct was investigated. Two experimental rigs were used—a tube burner and a rectangular channel with high aspect ratio. The confined tube burner contained a backward-facing step with a fixed height as flame stabilization. The channel setup was comprised of either a backward- facing step or a stabilization right inside the boundary layer by means of a hot ceramic tile flush with the channel walls. The flashback limits obtained from the confined experiments were relatively higher than the well-established unconfined results. A good match was observed between the confined tube burner and the channel results. The quenching distance between flame and wall, the resulting geometry-dependent leakage flow and the associated flame base shift as well as the reduction of the local pressure gradient in the boundary layer region by

the leakage flow are the determining factors in order to analyze differences between confined and unconfined flames. It was summarized that the distribution of the flame backpressure and the flame position itself were key parameters for the determination of meaningful turbulent boundary layer flashback limits.

Zhang et al. (2012) investigated the combustion characteristics of syngas micro mixing injection combustion flames diluted by CO_2 and the characteristics of the flames under the different dilution ratios and different C/H ratios. Results showed that the temperatures around the nozzles decrease with increasing CO2 dilution amount. The higher the CO_2 dilution amount, the lower the temperature. So combining CO_2 dilution and the micro mixing injection combustion approach could reduce the high nozzle exit temperature problem associated with micro mixing injection combustion. Both NO_x emissions and CO emissions could be reduced below 3 ppm by adjusting the ratio of the fuel and the air. Results showed that when the dilution ratio is constant, increasing the C/H ratio increases the nozzle exit temperature and the NO_x emissions and the CO emissions increase.

Zhu et al. (2012) conducted an experimental study of lean blowout with hydrogen-enriched fuels. Combustion of pure methane and blended methane-hydrogen with hydrogen-levels up to 80% by volume was carried out in a swirl stabilized premixed combustor. Particle imaging velocimetry (PIV) and OH* chemiluminescence imaging was used in this study. Results showed that there was a single-ringed structure of internal recirculation zone (IRZ) in the non-reacting flow, but there is a more complex flow pattern with a two-celled IRZ structure in which the axial velocity near the center-axis is oriented downstream. The width of IRZ decreases in methane flames with

decreasing equivalence ratio, but it increases in hydrogen-enriched flames, and the flame shape changes from conical to an elongated columnar shape. There were two different types of vortex breakdown observed, spiral mode in methane flames and bubble mode in hydrogen-enriched flames. The differences in the mechanisms of LBO in pure methane and hydrogen-enriched premixed flames were examined and explained here.

Shaffer et al. (2013) studied the fuel composition effects of flashback using a confined Jet Flame Burner. They used a jet burner configuration to develop systematic data for a wide range of compositions under turbulent flow conditions. The burner consisted of a quartz burner tube that is confined by a larger quartz tube. Various fuel compositions of hydrogen, carbon monoxide, and natural gas were used. They captured Schlieren and intensified OH* images at high speeds during flashback that allowed the understanding of what is occurring during the highly dynamic process of flashback. The authors analyzed confined and unconfined flashback data by comparing data collected in their present study with existing data in the literature. From the Schlieren and intensified OH* images, flashback was observed to be occurring through the boundary layer mechanism. This illustrates that turbulent conditions lead to considerable variability relative to the physical location of flashback inception and consistency for larger tubes and turbulence levels. While the Schlieren imaging techniques were applied without confinement, the intensified OH* images show that flashback was also occurring through the boundary layer mechanism when the confinement was installed. Higher hydrogen content and higher adiabatic flame temperature are responsible to higher flashback propensity. Adding methane or carbon monoxide hindered flashback to a different extent.

Fu et al. (2013) studied on laminar flame speed and flame structure of syngas with varied compositions using OH-PLIF. Hydrogen fractions ranging from 20% to 80% and equivalence ratios from 0.5 to 1.2 were studied. Kinetic simulations were done using CHEMKIN-II. Flame structures and radiation spectrum were examined using a PLIF system and spectrograph. OH-PLIF Bunsen flame method was used to measure the laminar flame speeds in a temperature-uncontrolled burner. Hydrogen fraction in syngas affects the laminar flame speed and flame shape and a good correlation was achieved between the experimentally measured laminar flame speeds and simulated ones. Kinetic analysis on intermediate radicals and sensitivity analysis showed that hydrogen plays very important role in accelerating combustion. Difference in flame color of varied H2 mixture was because of their difference in radiation spectrum of the intermediate radicals produced in combustion.

Khalil et al. (2013) investigated hydrogen addition effects on high intensity distributed combustion.8% hydrogen enriched methane fuel under different equivalence ratios showed great promise for different applications. Novel premixed combustor design, demonstrated low emission of both NO and CO for hydrogen enriched methane fuel. The combustor demonstrated 3.2 ppm of NO and 9 ppm of CO at an equivalence ratio of 0.5. This is a significant reduction of CO and a very little increase in NO as compared to the methane fuel only (2.2 ppm NO and 650 ppm CO) that indicates that the combustor is able to operate at leaner conditions without being suffered from lean combustion instabilities or incomplete combustion. The OH chemiluminescence intensity distribution with 8% hydrogen enrichment for the premixed combustion mode showed that the reaction zone location is not altered with the change in equivalence ratio. As compared to pure methane case, the flame was observed to be less volume

distributed. The addition of hydrogen improved the lean stability limit. No unsteadiness was observed in global imaging for the flame with hydrogen addition. CHEMKIN-PRO was used to make a correlation for NO emission of 8% hydrogen enrichment case and the results provided good agreement with the experimental data that indicates the possibility of good prediction on emissions from different hydrogen enrichments amount using measurements from pure methane.

Ferrières et al. (2013) investigated the kinetic effect of hydrogen addition on natural gas premixed flames. Structure of a reference laminar premixed natural gas flame and a natural gas/hydrogen flame were investigated at atmospheric pressure with the same carbon to oxygen ratio. Gas chromatographic analysis (GC-TCD-FID) and FTIR were used to obtain experimental mole fraction profiles for stable species. Twelve C_2 to C_4 intermediate species were detected. GDF-Kin 3.0 which is recently developed kinetic model for natural gas combustion was used to model the mole fraction profiles for reactants, intermediates and products. The model was used to identify major reaction pathways. Good agreement was found between model predictions and experimental results. The C1 oxidation sequence is reinforced because of the recombination of H and C_2H_5 yielding methyl radicals in natural gas/hydrogen system. At the same time C2 sequence was disfavored and a reduction of mole fraction of acetylene and ethylene was observed. In natural gas flames, H-abstraction reactions are dominated mainly by OH radicals, whilst H-abstraction by H-atoms dominates in natural gas/hydrogen flames. GDF-Kin 3.0 can also reproduce recent burning velocities of hydrogen/air and natural gas/hydrogen flames.

1.3.3 NO_x emission of syngas studies

Rizk et al. (1991) studied lean low NO_x combustion concept evaluation. Testing was done under wide variation of flow parameters and primary/dilution air split in order to evaluate the impact of effect of variable geometry. Data analysis showed that the residence time and the chemical reaction rates are the primary factors to control the NO_x formation. Entrance of more air through the dilution holes increased the formation of relatively high temperature region inside the primary zone that is prone to produce NO_x.

In Oliver et al. (2000) thermo acoustic modes were investigated and controlled in an experimental low-emission swirl stabilized combustor. Proportional acoustic actuation and fuel modulations were used in an experimental low-emission swirl stabilized combustor where the acoustic boundary conditions were modified to obtain unstable operation and two unstable modes were investigated in fully premixed combustion: axisymmetric and helical. Unstable modes were associated with flow instabilities that are related to the recirculation region on the combustor axis and shear layer instabilities at the sudden expansion. The axisymmetric mode showed large variation of heat release and helical modes showed azimuthal variations of maximal heat release during one period of oscillations. Closed loop active control systems were used to suppress the thermo-acoustic pressure oscillations maintaining low NO and CO emissions. Mixing process between fuel and air were varied by the acoustic excitation and the combustion products. An open loop control system was utilized by modulations of a secondary pilot flame.

Richard et al. (2001) investigated the issues for low-emission, fuel-flexible power systems. This paper reviewed the technical issues concerned with using variable-composition gaseous fuels in low emission energy systems. In gas turbines, premixed combustion has become a popular choice in order to reduce NO*x* emissions. Although premixed combustion has an advantage of lower emissions, flame position and stability may be affected by changes in fuel composition. Flame flashback, autoignition, dynamic oscillations and lean blowout are the concerning factors as potential complications for the changes in fuel composition. Specific considerations were noted for medium and low heating value fuels compared to natural gas and fuels containing ammonia that are typical of gasification.

Tacina et al. (2002) investigated a low NOx Lean-Direct Injection, multipoint Integrated module combustor concept for advanced aircraft gas turbines where they used a multipoint (25- and 36-fuel injectors), lean-direct injection concept. Testing was carried out up to 810 K inlet temperature, inlet pressures up to 2760 KPa, and flame temperatures up to 2100 K and a correlation was formulated relating the NOx emissions with the inlet temperature, inlet pressure, fuel-air ratio and pressure drop. The NOx emissions using, the correlation from flame-tube tests, were estimated to be less than 20 percent of the 1996 ICAO Standard by assuming that 10 percent of the combustion air would be used for liner cooling and using a hypothetical engine cycle.

Guo et al. (2004) investigated the effect of hydrogen addition on lean counterflow CH_4/air premixed flames and their extinction limits. This study also investigated the characteristics of NO_x emission by numerical simulation where they used detailed chemistry and complex thermal

and transport properties. Results showed that the addition of hydrogen can enlarge the flammable region and extend the flammability limit to a lower equivalence ratio. At the same time, if equivalence ratio is kept constant, the addition of hydrogen increases the emission of NO in a flame because of the enhancement in the rate of the NNH or N_2O intermediate NO formation route. The addition of hydrogen causes a decrease in the formation of NO_2 and N_2O at relatively higher equivalence ratio.

Giles et al. (2006) investigated the NO_x emission characteristics of counterflow syngas diffusion flames with airstream dilution. Counterflow syngas flames were simulated using two representative syngas mixtures, 50% H_2/50% CO and 45% H_2/45% CO/10% CH_4 by volume, and three diluents, N_2, H_2O, and CO_2. The effectiveness of these diluents were characterized in terms of their ability to reduce NO_x in syngas flames. Results showed that syngas non- premixed flames are characterized by comparatively high temperatures and high NO_x concentrations and emission indices and using of methane in syngas decreases the peak flame temperature but increases the formation of prompt NO significantly. For both mixtures, CO_2 and H_2O were shown more effective than N_2 in reducing NO_x in syngas flames. H_2O is the most effective diluents on a mass basis because the effectiveness of H_2O is because of its high specific heat that decreases the thermal NO and also it has the ability to significantly reduce the concentration of CH radicals that decreases the prompt NO.

Griebel et al. (2007) investigated lean blowout limits and NO_x emissions of turbulent, lean premixed and hydrogen-enriched methane/air flames at high pressure. Results showed that premixing of hydrogen extend the lean stability limit significantly. Results showed that

equivalence ratios, where LBO is observed, are lower with hydrogen enrichment because of a higher OH radical concentration that leads to a higher global reaction rate and a higher flame speed. It was also seen that LBO limit is linearly dependent on the hydrogen content of the fuel. Because of higher bulk velocities, decreasing the turbulence intensity in the combustor inlet results in slightly lower LBO limits compared to LBO limits of the high-turbulence grid that could be attributed to lower flame stretch effects due to lower turbulence intensities in the jet core. A strong positive impact of the LBO extension on the emission characteristics of lean premixed flames was found due to H_2 enrichment. Lower minimum NOx emissions could be obtained because of a lower flame temperature at lower equivalence ratios.

Som et al. (2008) presents a numerical and experimental investigation of the combustion and NO_x characteristics of syngas fuel with varying composition, pressure and strain rate. Experiments were performed at atmospheric conditions and the simulations were done at different pressures. Both experiments and simulations showed that stable non-premixed and partially premixed counterflow flames (PPFs) can be obtained for a wide range of syngas compositions and strain rates. Three chemical kinetic models, GRI 3.0 that used by Davis et al. (2005) and Mueller et al. (1999) were used. Davis et al. (2005) mechanism agreed with the experimental data the best. Thermal NO was found to be the dominant route for NO production, and a reburn route is also important at high pressures. The amount of NO formed in syngas PPFs first increases rapidly with pressure, and then levels off at higher pressures.

G.L. Juste (2012) evaluated the effects of hydrogen injection as an addition fuel in gas turbine combustor. This paper showed making the primary zone more lean, increasing the primary air, is

an efficient means to reduce NO*x* emissions. However this method decreases efficiency, because CO and HC emissions increase. By injecting small quantities of hydrogen to lean primary zones, the amount of CO can be reduced without a relevant increase in NO*x*. The CO reduction depends on hydrocarbon substitution and mainly to chemical kinetics. Also, addition of small quantities of hydrogen contributes substantially to the reduction of the emissions of CO_2. CO_2 emissions, is very important.

1.3.4 Multiport burner studies:

Marek et al. (2005) tested multiple injector configurations, Fig 1.17, based on LDI technology with multiple injection points and they concluded that NO_x emissions are comparable to that of the Jet -A LDI concepts. Tacina et akl.(2002) described a multi-point, lean direct injection concept (Fig 1.23) where they tested a different number of fuel injectors and swirlers. They concluded that the NO_x levels of 36-point injector with co-rotating swirler are lower than 25-injector configuration as a result of the greater number of small mixing sites. Cai et al. (2002) concluded that the co-swirler array has longer recirculation zone and similar turbulent kinetic energy level compared with counter –swirler array that ensures combustion stability.

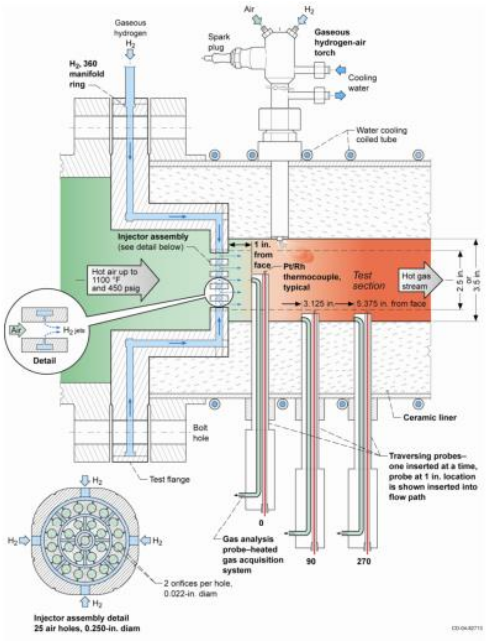

Figure 1.17 : Sketch of NASA low emissions LDI hydrogen combustor [Marek et al., 2005]

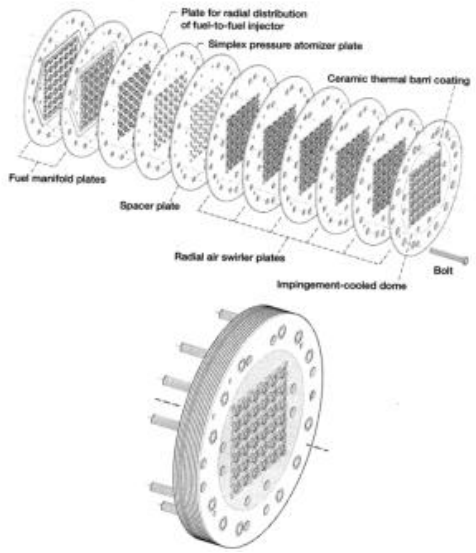

Figure 1.18 : Multi-point integrated module: etched plates (top), flame tube configuration (bottom) [Tacina et al., 2002]

Hariharan et al. (2006) carried out an experimental study on turbulent hydrogen flames from circular and elliptic burners with varying degrees of premixedness. Results showed that the liftoff velocity of the elliptic burner flames was lower than that of the circular burner flames. At all air equivalence ratios, except for diffusion flames, the elliptic burner flames were shorter than circular burner flames. For both circular and elliptic burner flames global NO concentration decreased with the increase in air equivalence ratio. For diffusion flames, the elliptic burner flames showed higher NO concentration at stoichiometric condition and lower at equivalence ratio of 1.33 (fuel-lean) and 0.25 (fuel-rich) conditions than in circular burner flames. Radiant fraction of heat release of elliptic burner flames were lower than in the circular burner flames. Elliptic burner flames showed lower peak axial NO concentration than in the circular burner flames.

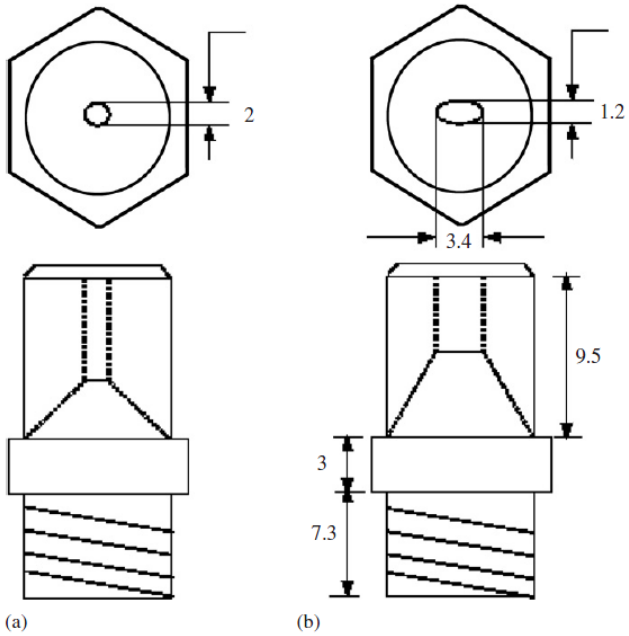

Figure 1.19 : Schematic diagram of the burners employed in this study (all dimensionsare in mm): (a) circular burner and (b) elliptic burner with 3:1 aspect ratio. [Hariharan et al., 2006]

Wu et al. (2007) studied advanced gas turbine combustion system development for high hydrogen fuels. Detailed combustion system testing was carried out during 2005 and 2006 with syngas/hydrogen fuels derived from different feed stocks and gasification processes. Fuel transfer capability to and from natural gas that is the startup and backup fuel, and syngas was studied over the operating range. Optimization studies were done with different diluent (H_2O and N_2) addition rates in order to determine the effect on emissions and operability. Main objective was to ensure that only combustion system modifications are key parameters for successful enriched hydrogen syngas fuel combustion. This paper summarized the results from Siemens combustion system development programs and mentioned that low emissions and wide engine operating range can be achieved on hydrogen fuel operation in advanced 50 Hz and 60 Hz gas turbines in IGCC applications with carbon dioxide capture

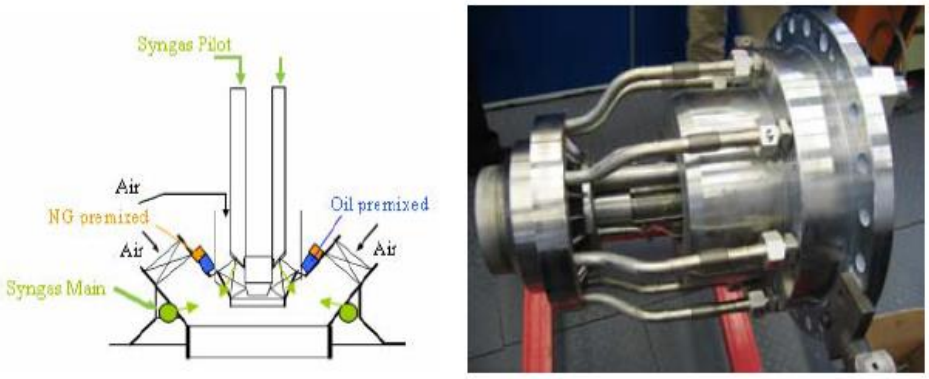

Figure 1.20: SGT5-4000F Triple-Fuel Syngas Combustor [Wu et al., 2007]

Hollon et al. (2011) used a micro-mixing lean premixed system for ultra- low emission hydrogen/syngas combustion. Small size and rapid mixing of air and fuel ensure a premixed fuel air mixture at the cup exit in a short time. They conducted a detailed experiment on combustion efficiency, lean stability and emission using multi mixing cup. They were able to meet the program goal of 2 ppm NOx emission

adiabatic flame temperature of 1750 K for a fuel mixture containing 50% hydrogen. The micro-mixing fuel injector operated with fuel mixtures ranging from 100% natural gas to 100% hydrogen without flashback and showed a great promise to use in future gas turbine engines.

Figure 1.21: Parker micro mixing cup

York et al. (2013) studied the development and testing of a low NO_x hydrogen combustion system for heavy-duty gas turbines. A fuel injector was designed especially for low-NOx combustion of high-hydrogen fuels like carbon-free syngas. The multitube mixer utilizes jet-in-cross flow mixing of the fuel and air inside of small-diameter tubes at many locations. Before testing this concept, entitlement NO_x emissions from perfectly-premixed combustion rig were measured for pure hydrogen, blends of hydrogen, nitrogen, and carbon monoxide. A 60%H_2-40%N_2 fuel produced the lowest entitlement NO_x of the fuels tested because of the presence of N_2 diluent. NO_x emissions were increased moderately with pressure and residence time over the full flame temperature range tested. The multitube mixer was tested in a small-scale single nozzle rig where realistic gas turbine conditions were used. For 60%H_2-40%N_2 fuel, flashback-free operation was observed for flame temperatures of over 1900K having a fairly low air-side

pressure drop of 3.5% across the premixer. Its single nozzle NO_x emissions were higher than a perfectly premixed combustion experiment with the same H_2-N_2 fuel because the MT mixer is not designed to fully premix the fuel and air. Aggressive flame holding testing was carried out with an upstream torch that provides an ignition event in the multitube mixer. In order to prevent the premixer from holding flame internally, a very small percentage of methane in the H_2-N_2fuel was needed and that amount of required methane increased with pressure. On flame holding boundary, small percentages of CO and CO_2 added to the fuel blend were found to have a negligible effect. The multitube mixer concept was employed in full-can combustion system designed for high-hydrogen fuel based on encouraging single nozzle emissions and operability. The scale up to a multinozzle combustor was successful for 100 hrs of operating experience with more than 90% hydrogen in the reactants. With 60%H_2-40%N_2 fuel, full-can NOx emissions were below 10 ppm at F-class conditions.

Using nitrogen caused NOx to fall significantly. 3 ppm NO_x @ 15% O_2 was measured in the target temperature range by using only 20% additional N_2. Results from both single nozzle and full-can experiments indicate that small-scale, jet-in-crossflow mixing approach in tubes is a robust, low- NO_x method of combusting high-hydrogen fuels in advanced gas turbines.

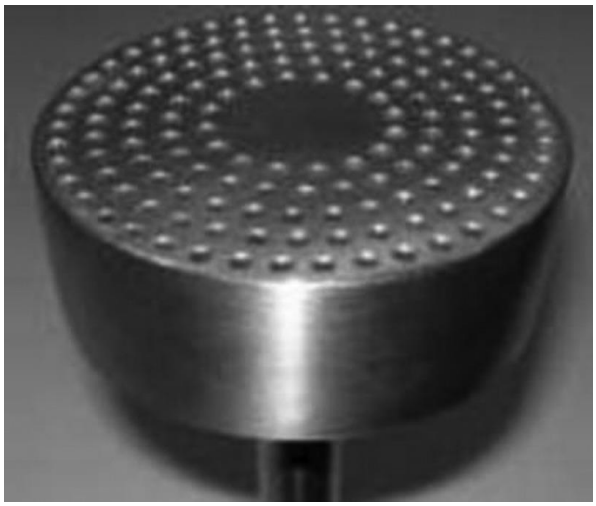

Figure 1.22 : Larger-scale multitube mixer used for single nozzle rig flame operability testing [York et al., 2013]

Dodo et al. (2013) measured the performance of a multiple-injection dry low NO_x combustor with hydrogen-rich syngas fuels. In order to demonstrate the feasibility of dry low-NOx combustion of hydrogen-rich fuels, the combustion characteristics of the prototype multicluster combustors were experimentally studied under medium pressure where the experiments were focused on the effects of fuel distribution and fuel composition. The tested combustors allowed stable combustion of fuels simulating 0%, 30%, and 50% carbon dioxide capture and storage (CCS). A convex perforated plate swirler was effective in suppressing combustion oscillation that allowed the NO_x emissions to be less than 10 ppm at fuel compositions simulating 0%, 30%, and 50% CCS.

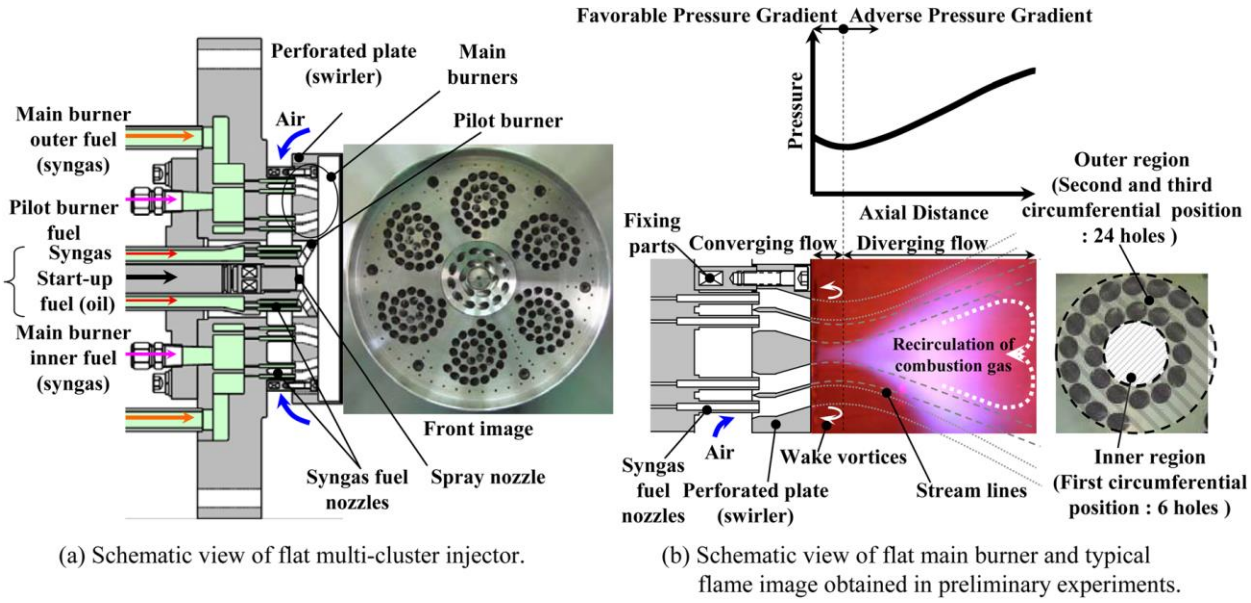

(a) Schematic view of flat multi-cluster injector.

(b) Schematic view of flat main burner and typical flame image obtained in preliminary experiments.

Figure 1.23 : Schematic view of the flat multicluster injector and its main burner [Dodo et al., 2013]

1.4 Flame ignition studies:

An external ignition is necessary in the form of heat to ignite the mixture. External ignition sources have been studied extensively.

Lewis et al., 1949 studied minimum ignition energy of hydrocarbons where they used spark circuit with low capacity high voltage condensers and the study was based on the minimum energies for igniting hydrocarbon gases with various oxygen-nitrogen atmospheres for short durations. The charge from the power unit to the spark circuit is transferred by the resistor. Gas is introduced and ignited to a test bomb followed by the using of electricity. They found that the energies shift toward the rich side as the number of carbon atoms is increased.

Kono et al.1977 carried out a long duration composite spark. They investigated the effects of gap width, electrode configuration, mixture strength, spark duration, and energy distribution between the two components on the minimum ignition energy by using a quiescent propane-air mixture. For a dc-discharge spark, the well-defined optimum spark duration varied from about 50 to 300 micro sec and the minimum ignition energy for spark durations larger than the optimum increases in different modes that are dependent on the mixture strength and the quenching effect of spark electrodes. For an ac-discharge spark, the optimum condition for ignition is as same as for a tic-discharge spark. But the minimum ignition energy and the spark duration are always proportional to each other above the optimum. Flash-schlieren photographic observations of the initial behavior of the spark kernel showed that such differences in the mode of minimum ignition energy are related to electrostatic attraction by the negative electrode.

Ptasinski et al. (2001) tested multiple capacitor discharges to investigate methane-air mixtures. They carried out multiple capacitor discharges with controlled and methane-air mixtures of various compositions have been examined. Ignition tests were done by using conditions of continuous flow of the mixture. The charge transferred in a single discharge pulse and the voltage before each pulse was recorded and Based on the values, the energy has been estimated. The measurements of discharge courses and incendivity testing were also done under different conditions, such as: time intervals between the successive pulses, methane concentration, capacity of the discharged capacitor and resistance of the decoupling resistor.

Morsy et al. (2003) investigated multi point ignition. They used a multi-point ignition technique with a single-shot laser and tested its feasibility experimentally in a constant volume chamber

filled with premixed hydrogen/air mixture. Two conical cavities were installed on combustion chamber walls that are aligned with laser. By directing unfocused laser beam into the first cavity that has an opening near the apex, part of the incident laser energy passes through the opening and irradiates into the second cavity. Simultaneous two-point ignition was achieved at each cavity. A simultaneous three-point ignition technique was based on directing focused laser beam into the two-cavity arrangement that produces additional ignition at the center of the chamber through laser-induced spark ignition. They demonstrated advantages of the proposed techniques over single-point ignition techniques through significant reduction in total combustion time. Shadowgraphs of the early stage of combustion process showed that hot gaseous jets were ejected from the cavities that results in rapid combustion. They also found that increase in incident laser energy accelerates jet ejection from the cavities.

Weinrotter et al. (2005) investigated laser ignition for hydrogen-air mixture at high pressure. Experiments were carried out in a high pressure, constant volume chamber (up to 25 MPa pressure and initial temperature of 473 K). They investigated laser induced ignition of different hydrogen–air mixtures, using different filling pressures (P = 0:5–4:2 MPa), different ignition energies (pulse energy PE = 1–50 mJ), different chamber temperatures (T = 393–473 K) and different focal length lenses (f = 60, 120 mm). They used a Q-switched Nd: YAG laser at 1064 nm with pulse duration of about 5 ns. The minimum pulse energy was decreasing with increasing initial pressures.

1.5 Dissertation Objective: To ensure the implementation of high hydrogen content (HHC) fuels for future power generation without negotiating with operational or emission advantages.

This study focuses on the flame stability and behavior of (HHC) fuels under gas turbine conditions. Based on these needs the main objectives are to

1. Design and develop an optically accessible fuel flexible high pressure gas turbine combustor system. This includes the ignition an external control system.

2. Design and test a novel fuel injector in order to investigate the effect of multi-tube geometry on flame stability and NO_x emissions of syngas fuels by using the designed high pressure combustor

Chapter 2 : Technical Approach

2.1 Design Methodology: This chapter discusses the methodology towards the design of the high pressure combustor which includes the steps used in designing. In the design approach, the first step was the determination of wall temperature followed by the calculation of adiabatic flame temperature. After calculation of the wall temperature, finite element analysis was carried out to obtain the wall and window thickness.

2.1.1 Adiabatic flame temperature: Syngas which is the mixture of carbon monoxide (CO), hydrogen (H_2) was taken into consideration to calculate the adiabatic flame temperature. Equation (1) was used to calculate the adiabatic flame temperature where 70% CO and 30% H_2 fuel mixture was used.

$$0.7\,CO + 0.3H_2 + 0.5(O_2 + 3.76\,N_2) -> 0.7CO_2 + 0.3\,H_2O + 1.88\,N_2 \qquad (2.1)$$

This composition was selected based on the analyzing of the range of syngas compositions across different types of gasifier; this mixture represents the maximum amount of hydrogen expected for testing in the combustor.

STANJAN, a chemical equilibrium solver written by Professor William Reynolds of Stanford University was used to calculate the adiabatic flame temperature (AFT).The adiabatic flame temperature of 30 % syngas was found to be 2400 K. This calculated temperature was then used to get the final wall temperature of the combustor.

Table 2.1 : Syngas composition across different gasifier type and feedstock

Source:http://www.netl.doe.gov/technologies/coalpower/gasification/gasifipedia/4-gasifiers/4-3_syngas-detail.html#

Range of Syngas Compositions Across Different Gasifier Type, and Feedstock Produced by the Gasification of Coal Feedstocks

Gasifier	General[1]	E-Gas[2]	Shell[3]	Shell[3]	GE[3]	KRW[4]	Air Blown – Trans-port[5]	Oxygen Blown – Trans-port[5]	E-Gas[6]	Wellman-Galusha (Air Blown)[7]	E-Gas[8]	GE[9] (Oxygen Blown)	GE[9] (Air Blown)	PREN-FLO[10]	TRIG (Trans-port Gasifier)[11]	TRIG (Trans-port Gasifier)[11]	BGL[12]
Facility	-	Wabash	-	-	-	Pinon Pine Power Project	-	-	Wabash	Pilot	Wabash	-	-	Puertol-lano	-	-	-
Coal	General	Several	General	General	General	Several	Several	Several	Several	Sulcis	Several	Unknown	Unknown	Coal/ Petcoke	Wyoming PRB	North Dakota Lignite	Several
CO	30-60	42.2-46.7	56.4	49.6	15.6	23.91	1-14	4-14	27.4	31.03	45.3	39.09-43.44	13.89-20.14	59.9	39.7	35.6	57.2
H_2	25-30	32.31-34.40	29.7	26.3	15.1	14.58	2-8	8-16	27.7	18.38	34.4	28.94-32.91	10.14-14.73	21.7	28.5	25.6	30.8
CO_2	5-15	14.89-17.13	1.4	1.3	7.3	5.45	7-14	12-14	16.5	2.54	15.8	9.32-13.53	6.09-8.85	2.9	14.3	17.5	4.9
H_2O	2-30	-	7	18.1	61	5.45	6-14	17-40	26.6	11.77	-	13.11-19.91	8.18-12.00	-	12.6	14.4	-
CH_4	0-5	1.04-2.29	-	-	-	1.35	1-2	2-5	0.0939	2.97	1.9	.02-.03	.02-.05	<0.1	4.3	6.1	6.2
Ar	0.2-1	-	0.7	0.6	0.8	0.56			0.7	0.51	0.6	0.06	.60-.66	14.4	.08	.07	-
N_2	0.5-4	-	4.53	3.86		48.68	54-72	30-55	0.6	43.02	1.9	.41-.45	49.50-54.11		.09	.09	-
H_2S	0.2-1	17.28-107.2 ppm	0.24	0.21	0.12	-	100-1300 ppm	2000-3000 ppm	0.1399	1.48	68 ppm	.58-.64	.26-.32	1.1	750 ppmV	2007 ppmV	-
COS	0-0.1	9.03-162.13 ppm	0.02	2		-	-	-	0.0061	0.08	-	.03-.04	0.02		40 ppmV	106 ppmV	-
Others	0-0.3	-	0.01	0.01	0.08	0.02	-	-	0.2	-	-	-	-	-	-	-	-

2.1.2 Wall Temperature: Wall temperature of the combustion chamber needs to be known to apply it as a boundary condition in the finite element analysis model. The calculated adiabatic flame temperature was used as a parameter to determine the wall temperature. Since the combustion chamber consists of modular parts that are made of different materials, separate analysis of wall temperature was conducted for each individual part –one is for outer stainless steel chamber and another one is for inner quartz chamber. Considering only convection inside the combustion chamber, heat transfer differential equation was solved to calculate wall temperature.

$$\dot{Q} = \dot{m} C_p \frac{dT}{dx} = hA(T_{Ad} - T) \qquad (2.2)$$

$$T = T_{Ad} + (T_{\infty} - T_{Ad}) e^{\left(-\frac{Aht}{C_p \dot{m}}\right)} \qquad (2.3)$$

The temperature profile corresponding to experimental time is plotted in Fig 2.1 and Fig 2.2. All of the properties used in the determination of wall temperature are listed in Table 2.2. Temperature profiles show that the wall of the chamber will reach the temperature of 2400 K which is the adiabatic flame temperature (the maximum temperature that the chamber could attain) within the experimental time of three minutes.

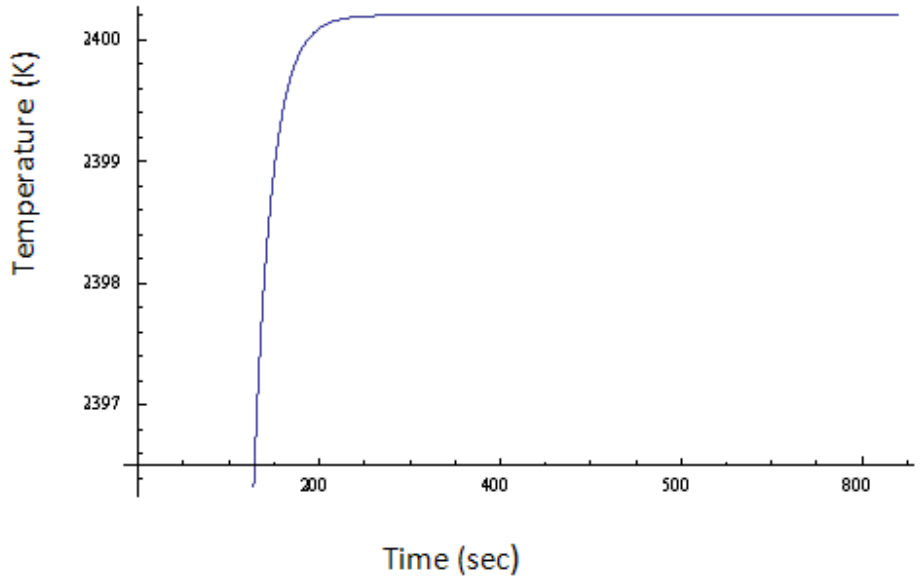

Figure 2.1: Quartz wall temperature as a function of experimental time

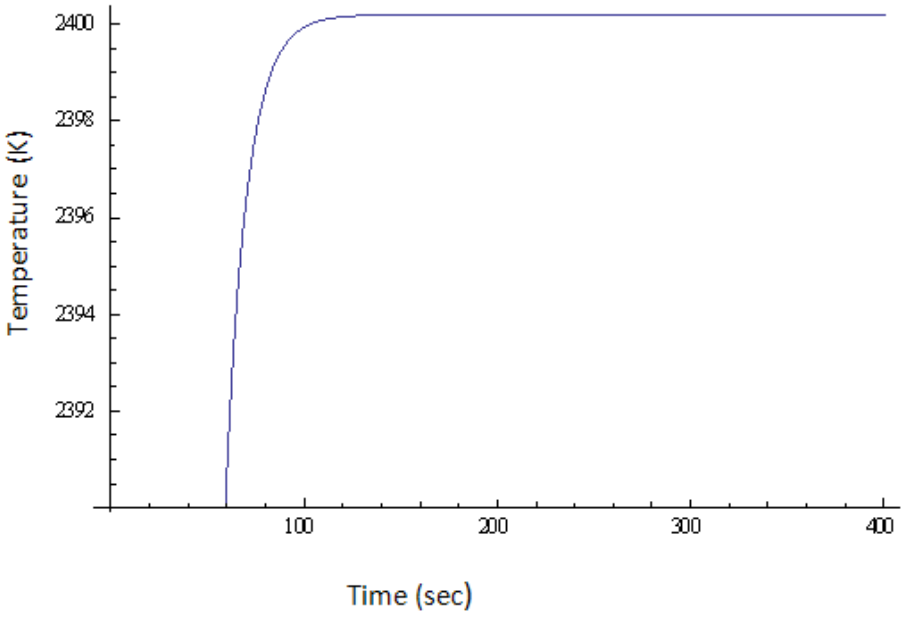

Figure 2.2: Stainless steel wall temperature as a function of experimental time

Table 2.2 : Parameters used for wall temperature calculation

T_{Ad}	**2400 K**
$\dot{m}$	$110\ g/sec$
$A_{stainles}$	$0.63\ m^2$
A_{quartz}	$0.28\ m^2$
$h_{stainless}$	$25\ W/(m^2\ K)$
h_{quartz}	$26\ W/(m^2\ K)$
C_p	$1.34\ J/g.K$
T_∞	298 K

Heat capacity was calculated based on the combustion products using mass weighted average. Mass flow rate was calculated based on thermal power of the combustor where lower heating value of the fuel was used to get the mass flow rate for the respective thermal power.

2.2 Finite Element Analysis: To analyze the stress distribution due to the elevated temperature and pressures, a computational model was developed using finite element analysis. The computational domain consists of the combustion chamber along with the interlocking parts. Material properties were developed based on the materials used to build up the chamber. Finite element analysis was conducted using Nastran 6. The calculated wall temperature was used as a boundary condition to apply as maximum thermal load.

2.2.1 Inner quartz chamber: Wall thickness is a key issue in designing a combustion chamber to avoid structural failure. The first analysis was conducted for the inner quartz chamber. The

material properties used for the chamber are listed in Table 2.3. An iteration method was used to finalize the wall thickness by using different thicknesses while the operating conditions were fixed. Since the quartz tube is constrained at both ends because of the pocket that was made to connect it with front cap and end cap. A 10 node tetrahedral mesh was used for the design simulation where elemental size of 0.01 m was used. At first the calculated wall temperature was used, after several trials 1100 K was used as temperature with a pressure load of 1.5 MPa inside the combustion chamber. Figure 2.3 and Fig 2.4 represent the displacement and stress analysis of the quartz chamber. Yield strength of the fused quartz material is 48 MPa. The resulted maximum stress from the simulation is 33 MPa with maximum displacement of 0.01 mm. Finally the thickness of the quartz was found by using the operating temperature of 1100K. A wall thickness of 58 mm was found that can sustain the temperature and pressure load by implementing the cooling system.

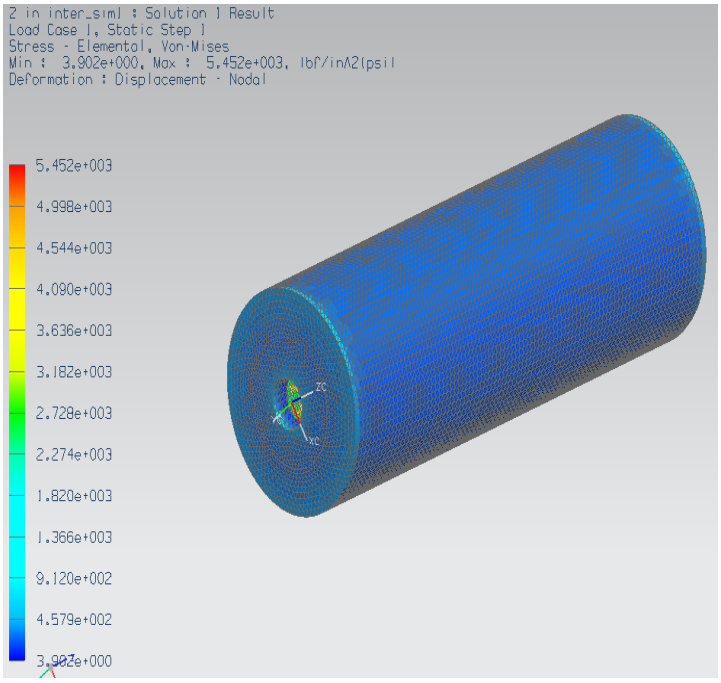

Figure 2.3 : Stress analysis of quartz chamber

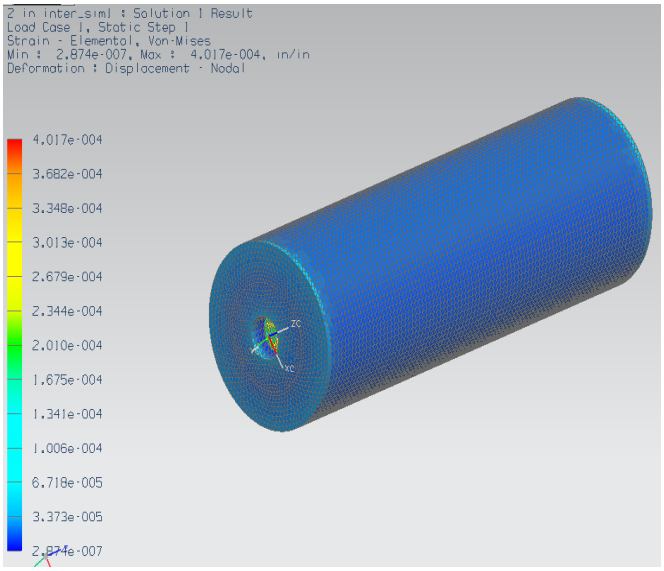

Figure 2.4 : Strain analysis of quartz chamber

Table 2.3**: Properties of fused quartz**

Sources: http://accuratus.com/fused.htm, http://en.wikipedia.org/wiki/Fused_quartz

Mechanical Properties	**Unit of Measure**
Density	2200 kg/m^3
Hardness	8.8 GPa
Tensile strength	48.3 Mpa
Bulk Modulus	37 Gpa
Poisson's Ratio	0.17
Thermal Properties	
Thermal Conductivity	1.3 W/m.K
Coefficient of Thermal Expansion	$5.5 \times 10^{-6}/^0C$
Specific Heat capacity	45.3 J/mol.K

2.2.2 Stainless Steel Combustion Chamber: Finite element analysis was carried out in order to get the wall thicknesses of the combustor that can sustain the buildup pressure and temperature inside the combustion chamber. A 10 node tetrahedral mesh was used for the design simulation along with an element size of 0.01 m. In the model, fixed constraints were used at the outer radial region of the end cap, front cap and bottom part of the combustor that is attached to the connecting curvature of the combustor stand. The stainless steel properties used in the design simulation are listed in Table 2.4. Considering the thickness of the combustion chamber wall of 88.9 mm and the operating temperature of 350K, the expected maximum stress was found. Maximum stresses were noticed at the corners of the window covers and at the edge of the instrumentation ports due to the irregularity of geometry at these locations where stress concentration occurs. The results are shown in Fig 2.5 and Fig 2.6 that illustrate the stress and displacement analysis of the combustion chamber. The maximum stress is 352 MPa and the yield strength is 586 MPa for the stainless steel 410. A maximum displacement of 0.13 mm was found for the stainless steel chamber.

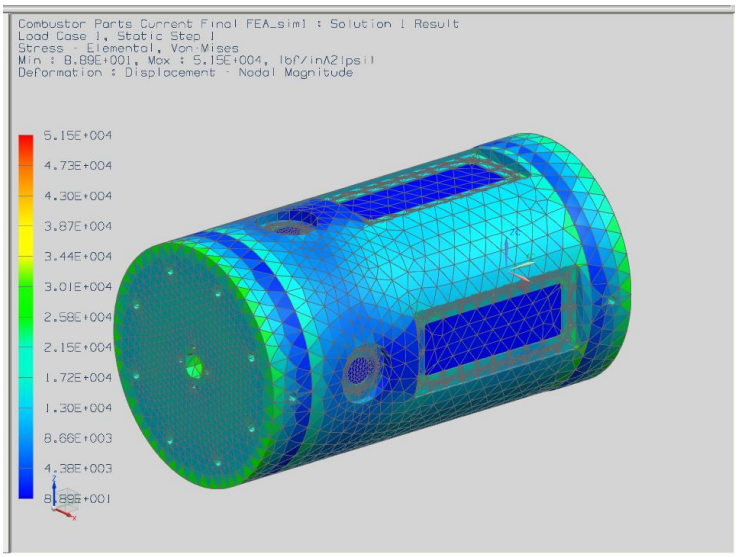

Figure 2.5: Stress analysis of Stainless Steel combustion chamber

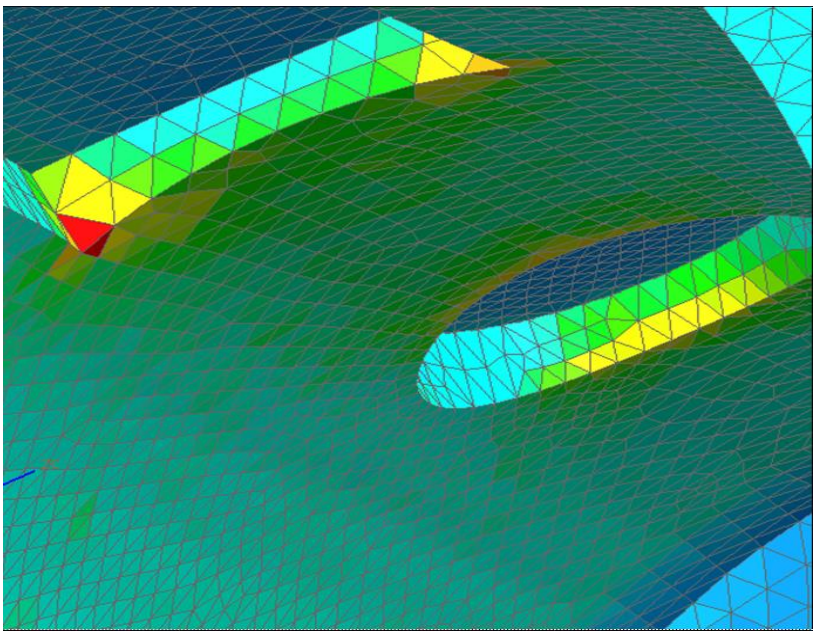

Figure 2.6 : Stress concentration in stainless steel chamber

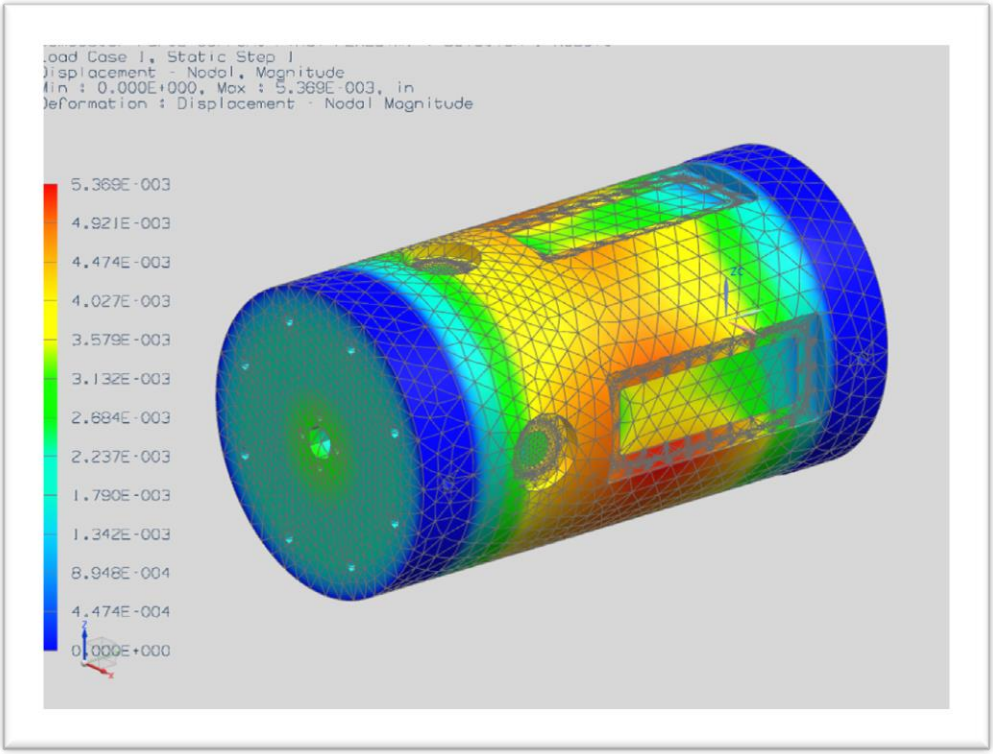

Figure 2.7: Strain analysis Stainless Steel chamber

Table 2.4: Properties of Stainless Steel 410

Source : http://bioenergylists.org/stovesdoc/Aprovecho/Stainlesstemp.pdf

Temperature	304 TS MPa	316 YS MPa	309 TS MPa	309S YS MPa	310 TS MPa	310S YS MPa	410 TS MPa	YS MPa	430 TS MPa	YS MPa
Room Temp	579	289	90	310	620	310	758	586	517	344
477 K	565	248	80	265	579	234	744	586	448	262
588 K	530	220	193	248	565	213	703	565	427	248
699 K	351	193	489	234	537	193	634	551	379	241
810 K	482	179	441	206	482	179	510	482	262	193
922 K	399	158	365	186	406	172	303	275	151	110
1033 K	234	137	241	137	282	165	-	-	68	55
1144 K	165	124	172	137	179	151	-	-	34	27

2.2.3 Window Covers: Finite element analysis of the window covers along with the combustion chamber was done. Stainless steel 410 was used and the properties used in the finite element analysis are listed in Table 2.4. A 10 node tetrahedral mesh was used with element size of 0.01m. FEA results are shown in Fig 2.8 and Fig 2.9 that represents the stress and displacement analysis of rectangular window cover.

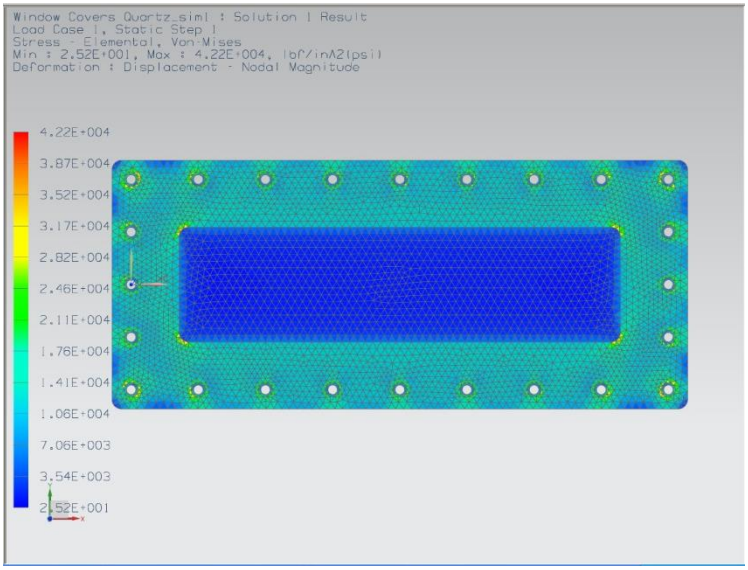

Figure 2.8 : Stress analysis of window cover

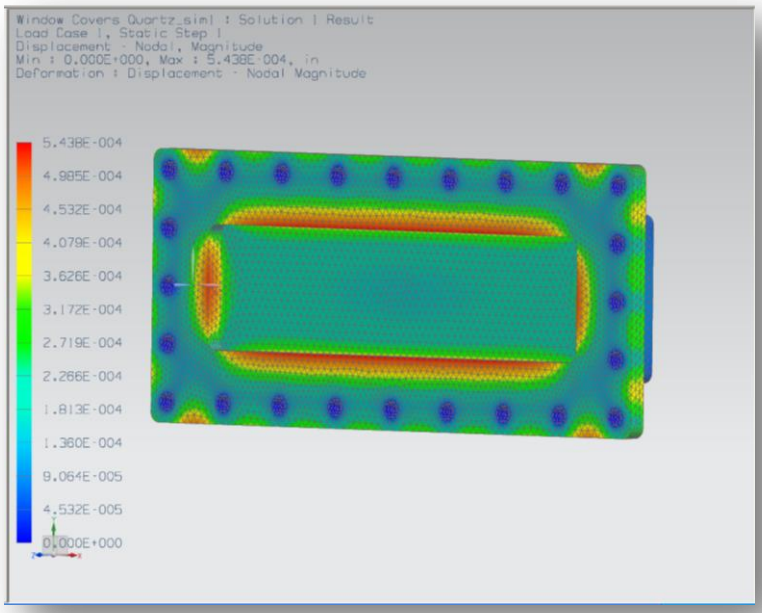

Figure 2.9: Strain analysis of window cover

In the computational model, fixed constraints were placed on the bolt of window covers by which window covers are attached to the combustor. As a boundary condition, temperature of 350 K and 1.5 MPa pressure was used. Results show that maximum stress is 289MPa and the yield strength is 586 MPa for the stainless steel 410.

2.2.4 Finite element analysis of mounting connection of stand: An analysis was carried out for the curvature connection that is attached to the stand and supports the combustor. A 10 node tetrahedral mesh was used along with element size of 0.005m. In the finite element analysis model, Steel A36 was used as a material; the properties are listed in Table 2.5.

Table 2.5 : Properties of Steel A36

Source:http://www.matweb.com/search/datasheet.aspx?matguid=afc003f4fb40465fa3df05129f0e88e6&ckck=1

Physical properties	**English**
Density	7.86 Ib/ In^3
Mechanical properties	400.550 MPa
Tensile Strength, Ultimate	250 MPa
Tensile Strength, Yield	20.0%
Elongation at break	23.0%
Modulus of Elasticity	200 GPa
Bulk Modulus	140GPa
Poissons Ratio	0.260
Shear Modulus	79.3 GPa

Results are shown in Figures 2.10 and 2.11 that represent stress and strain analysis of the curvature connection. Constraints were used at the bottom part of the curvature since this part is wielded with the curvature connection. Thrust (2.68 kN) that is expected to create by combustor was used as a point load for two holes of the curvature by which combustor is bolted. As a boundary condition, total weight of the combustor (76 kN) and a temperature load of 350 K has been used on the bottom surface of the curvature. Yield strength of Steel A36 is 250 MPa. Result shows that maximum stress is 122.7 MPa.

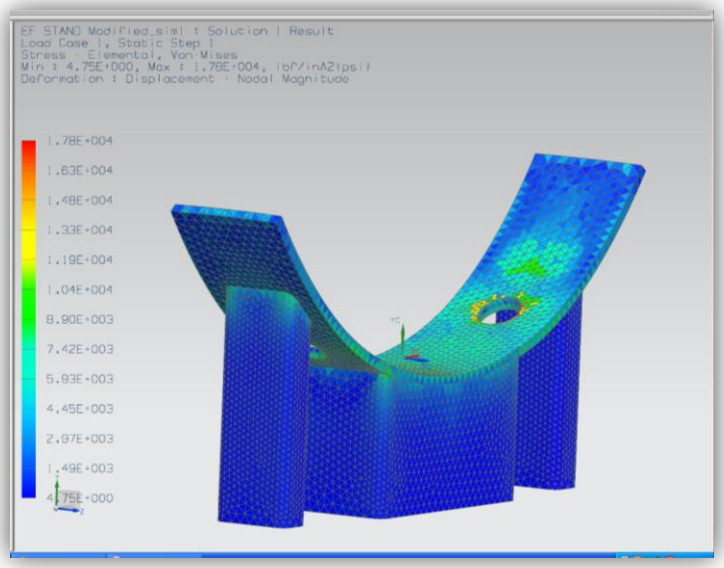

Figure 2.10: Stress analysis of curvature of test mounting

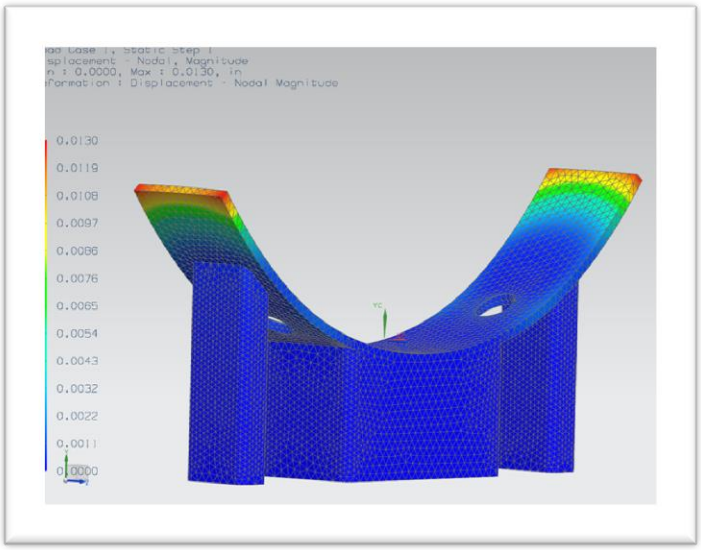

Figure 2.11: Strain analysis of curvature mounting connection

2.3 Safety factor: The main purpose of the finite element analysis done on the test assembly and combustion chamber is to evaluate the safety factor of our design. In our analysis we found that the maximum stress for the inner quartz chamber is 33 MPa while the yield strength of fused

quartz is 48 MPa which gives the safety factor of 1.45. For outer stainless steel chamber, the maximum stress found is 351 MPa and the yield strength of AISI Stainless steel 410 is 586 MPa which yields the safety factor of 1.67. For window covers, we have the safety factor of 2 and for stand assembly, the safety factor is 2. Overall we have the safety factor of over 1 which indicates that our design is safe enough to conduct high pressure combustion test.

2.4 Design Parameters: The design and development of this test rig is based on the parameters mentioned in Table 2.6.The combustor is designed to operate at 1.5 MPa. The operational temperature is the adiabatic flame temperature of 30% H_2 of syngas, although higher temperature based on the hydrogen composition is also allowable because of the developed cooling system.. The combustor is designed to analyze the flame stability and NO_x emission of high hydrogen content fuel.

Table 2.6: Design Parameters

Parameters	Specification
Thermal power	500 kW
Chamber Pressure	1.5 MPa
Temperature	2400K
Mass Flow	Air -81.93 kg/sec,Fuel -35.77 gm/sec
Measurements	Flame stability and NOx emission

2.5 Design and Description: Inlet manifold, front cap and end cap are integral parts of the combustor. Design descriptions are illustrated in the following sections.

2.5.1 Inlet manifold: Inlet manifold has three different sections as shown in Fig 2.12. It is made out of stainless steel 316 having 5 cm inner diameter with 6.35 cm thickness. All three sections are completely modular. Total length of inlet manifold is 54.5 cm. First part of the inlet manifold is 35 cm long and it consists of the fuel-air injection system that is comprised of four fuel injection holes and one hole for air. This is the first mixing section of air and fuel. Mid-section of the manifold is 11.5 cm long that consists of a honeycomb that helps to eliminate the injection induced flow irregularities. Third section acts as a connector with the front cap which is 7.6 cm long. All the three sections are connected by flanges and a disc that is attached to the third section of the inlet manifold and it is used to attach the entire inlet manifold with the front cap by using 6.35 mm bolts.

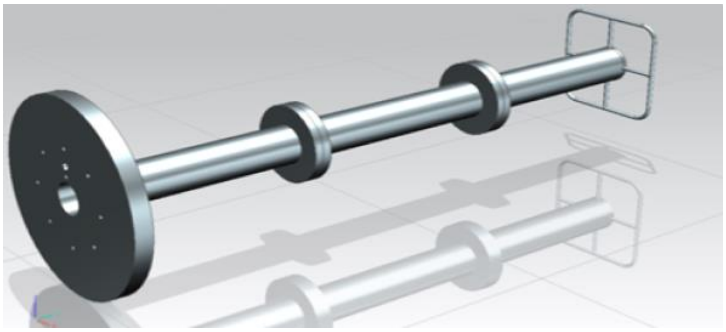

Figure 2.12: Inlet manifold

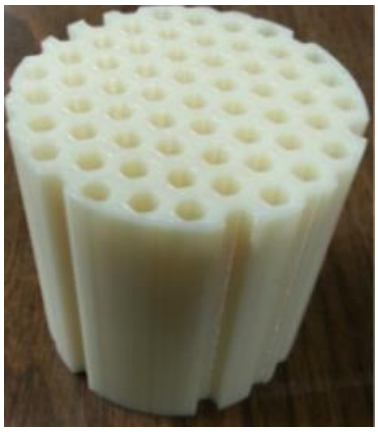

Figure 2.13: Honeycomb

2.5.2 Front Cap of Combustor: The front cap of the combustor serves as a sealant and it connects the inlet manifold with the main combustor chamber. It also houses the ignition system, swirler/ fuel injector and instrumentation holes. A 5.08 cm inner hole located at the center of the front cap houses the swirler /fuel injector. Instrumentation ports can also be made in the front cap that will allow the use of pressure transducer, thermocouples, or any configurable instrumentation device as per need. Front cap is connected to the main combustion chamber by using eight 12.7 mm diameter bolts and inlet manifold is attached to the front cap by using 6.35 mm diameter bolts. An ignition system is designed through the front cap. In order to place inner quartz chamber inside the main combustion chamber, a circular pocket as shown in Fig 2.14 is designed to accommodate the quartz chamber. A complete draft is shown in Fig 2.16.

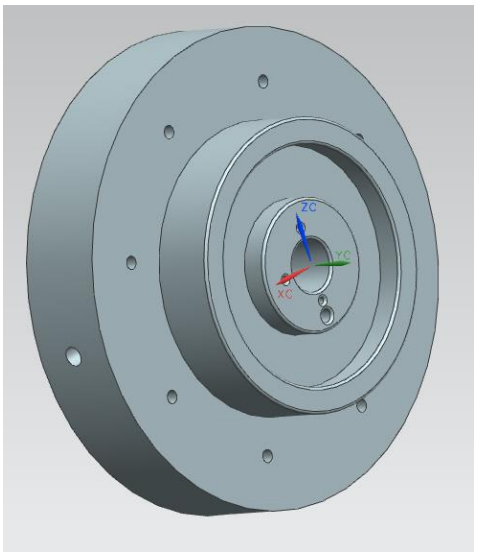

Figure 2.14: Front cap having pocket for quartz chamber

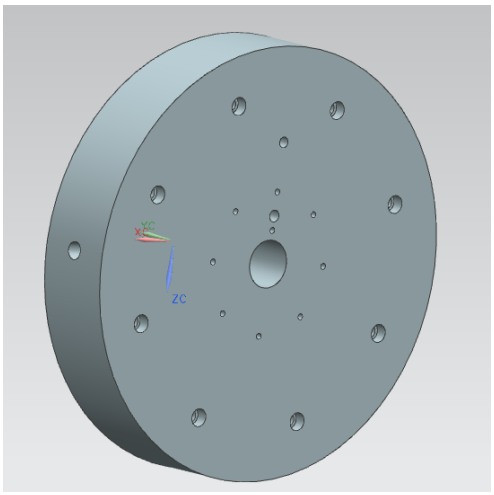

Figure 2.15: Front cap connecting Side for Inlet Manifold

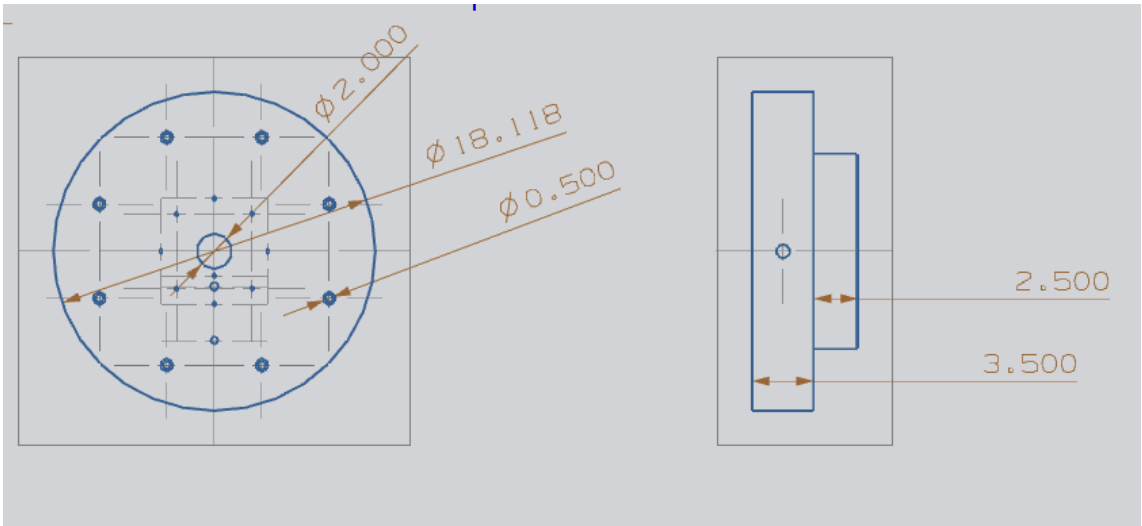

Figure 2.16 : Draft of the front cap of the combustor

2.5.3 Ignition system: A coaxial pilot flame has been integrated into the combustor to be used as the ignition system. An extended spark plug electrode provides the electric discharge that is needed to ignite the fuel. A modification was made in the front cap in order to install the ignition system. A 1.67 cm hole was made at an angle of 10° to facilitate the threaded entrance of the ignition system. 10° angle was maintained in order to make sure that the pilot flame will hit the main fuel-air stream and it will not make any hindrance to accommodate the inner quartz chamber. Figure 2.17 shows the modifications that were made to the front cap.

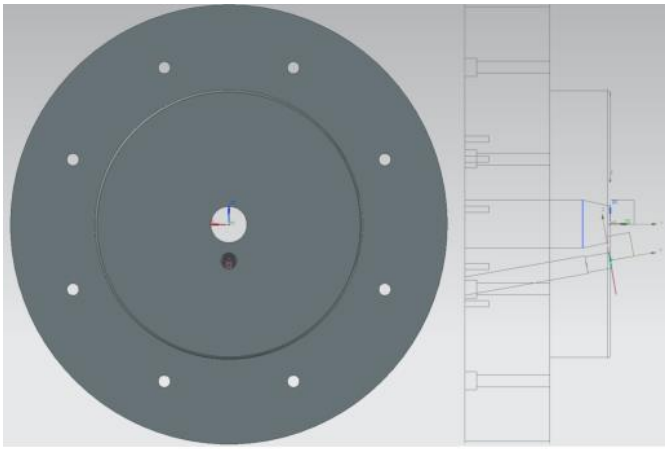

Figure 2.17: Modifications of front cap for igniter.

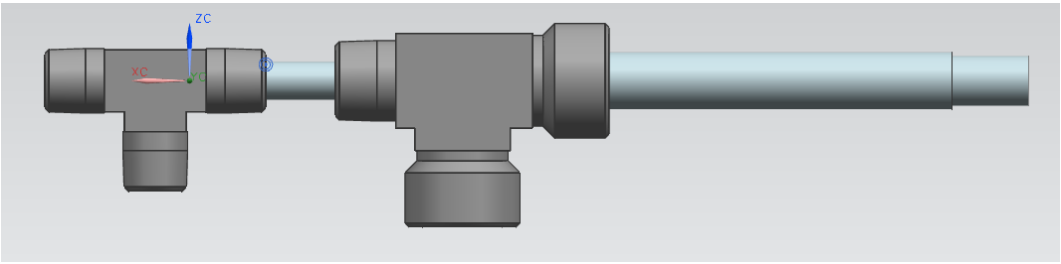

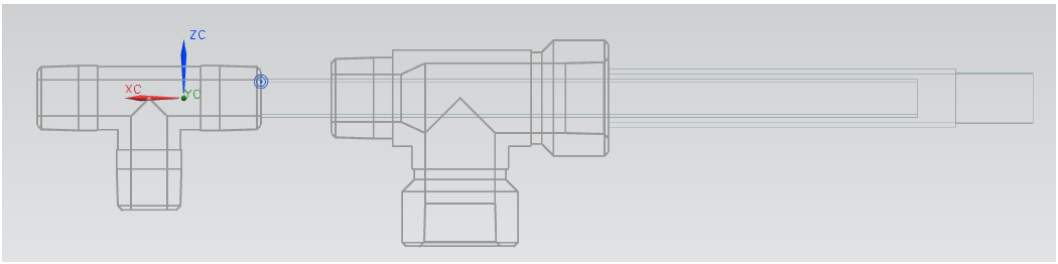

Figure 2.18 : Design of the igniter

A concentric design as shown in Fig 2.18 has been developed for housing the igniter in order to make sure that there will be no premixing with pilot flame gas where the outer tube has the diameter of 1.905 cm and the inner tube has that of 1.27 cm. A housing as shown in Fig 2.19 was

designed to place the spark plug. Spark plug has a diameter of 1.2 cm for the threaded part and the reducer end has that of 1.27 cm by which it is connected to the igniter. The reducer part is then connected to a T connector where the tube for pilot flame is connected too. Spark plug needed to be extended in order to make it applicable for the length of 45.72 cm. Since Haynes 230 has low resistivity and high melting point, it was used as the central electrode material. The Haynes 230 rod was welded (Fig 2.20) to the spark plug. Ceramic insulator was used to insulate the electrode because of its high temperature resistance.

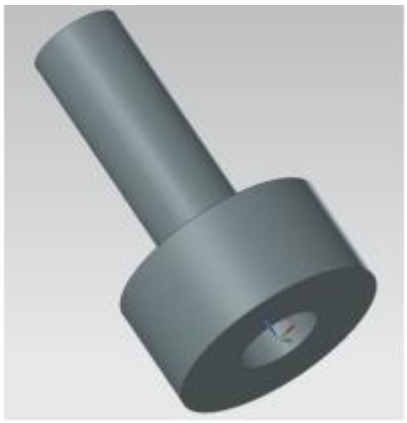

Figure 2.19 Spark plug housing

Figure 2.20: Spark plug components

2.5.4 Stainless Steel Combustion Chamber: The material used for the stainless steel chamber is AISI Stainless Steel 410 and this type of stainless steel is selected because of its high yield stress and other required properties. Total length of the combustor is 0.65 m. Inner diameter of

the combustor is 0.28 m and wall thickness is 88.9 mm. At each end of the combustor, eight 0.01 m diameter threaded holes are positioned in order to make the connection for the front cap and end cap. Three circular ports of 0.05 m diameter towards downstream will allow for either utilization of instrumentation devices (for the placement of thermocouple, pressure transducer, gas analyzer, material testing inside the combustor) or for visualization purpose. Three rectangular windows are located on the two sides and top of the combustor that are evenly spaced. The rectangular window slot dimension is 0.32 m by 0.10 m leaving an additional tolerance of 0.5 mm to allow the use of gasket. Different views of the combustor are shown from Fig 2.21 to 2.25.

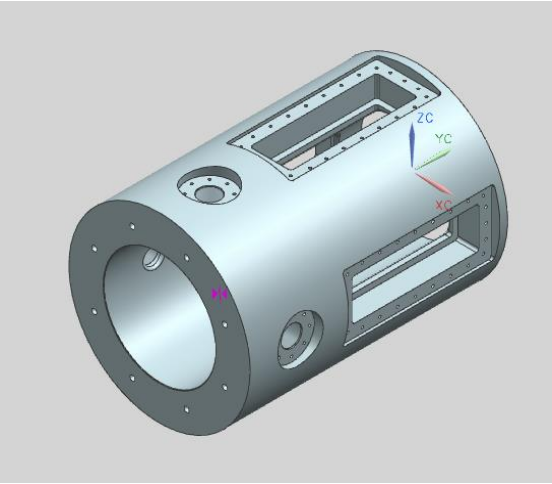

Figure 2.21: Stainless Steel combustor

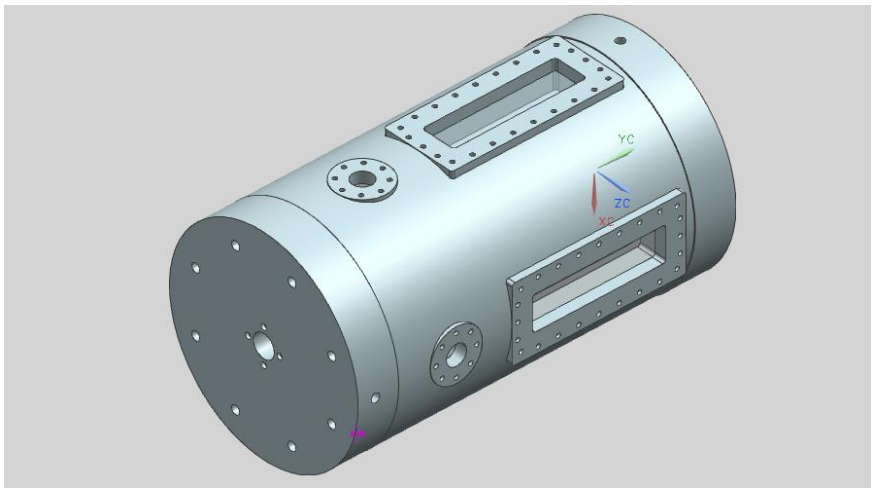

Figure 2.22 : Stainless Steel combustor with all integrated parts

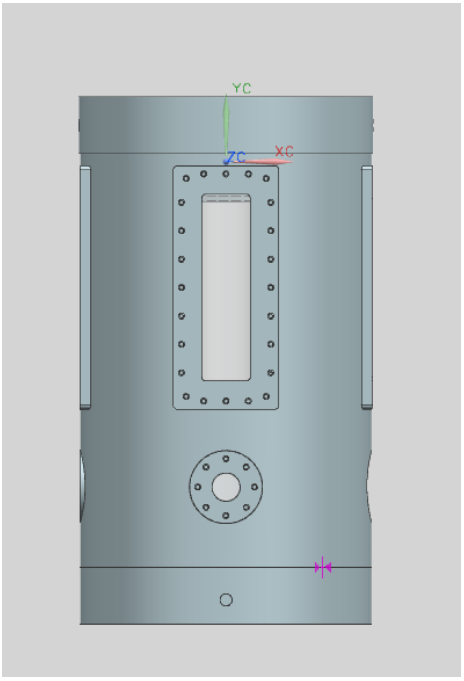

Figure 2.23 : Top view of the combustor

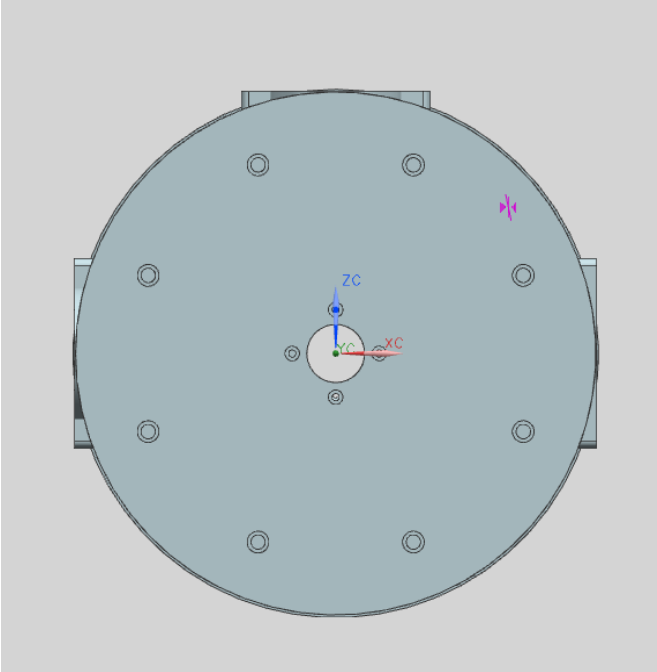

Figure 2.24 : Back view of the combustor

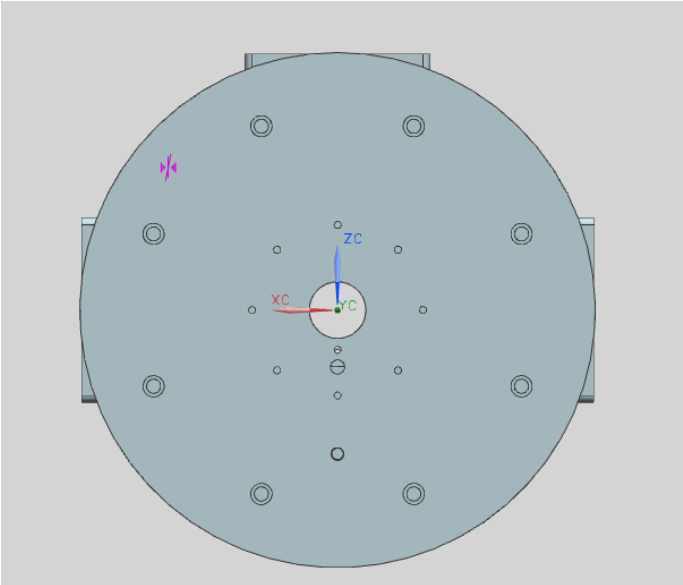

Figure 2.25 : Front view of the combustor

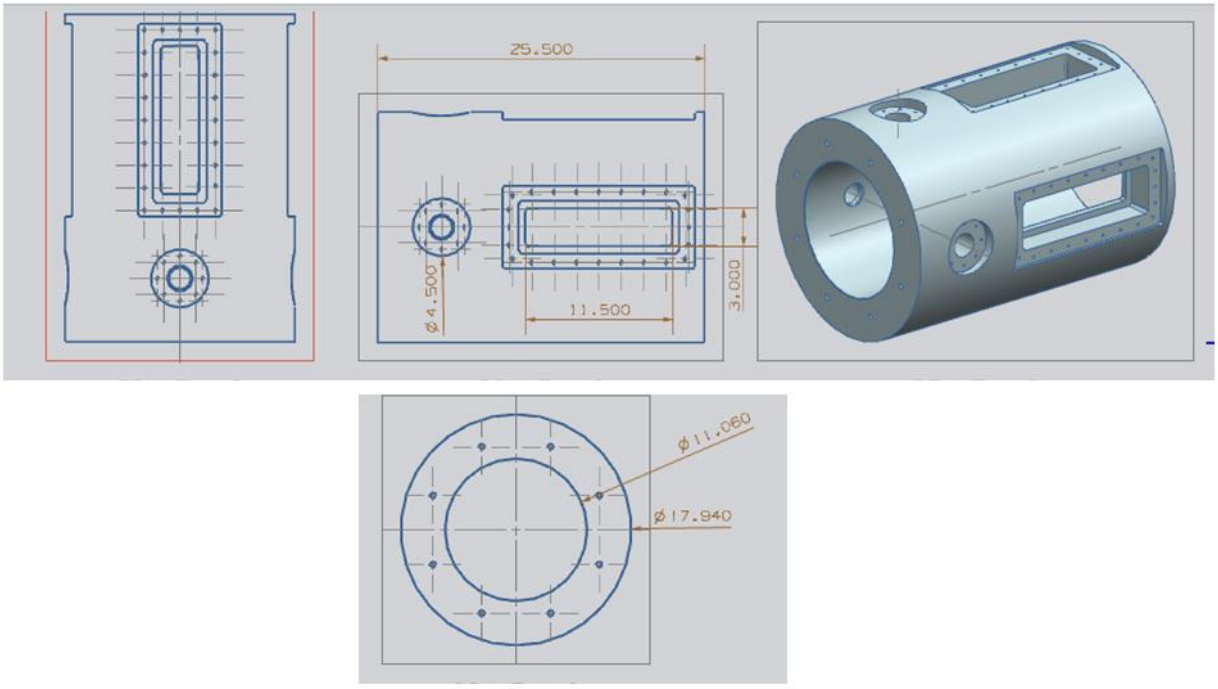

Figure 2.26 : Drafting of the combustor

2.5.5 Window covers and circular ports: The window covers are used to secure the rectangular quartz windows with the slotting that was made on the combustor wall. The windows covers are attached to the combustor by the use of twenty four 6.35 mm diameter bolts. The design is shown in Fig 2.27. Outer dimensions of the covers are made up of 16.51 cm by 38.1 cm length and inner dimensions are of 10.16 cm by 29.21 cm having overall thickness of 2.54 cm. Eight 12.7 mm diameter bolts are used to secure the circular windows. Circular ports are interchangeable. They can be used for visualization purposes or can be used as instrumentation ports.

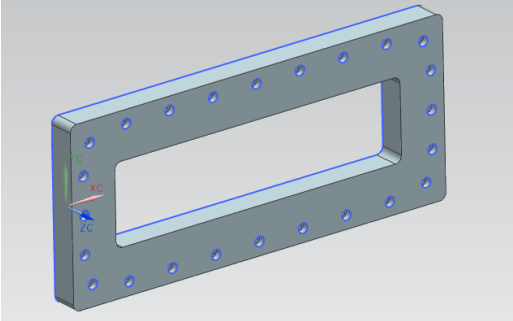

Figure 2.27: Rectangular window cover

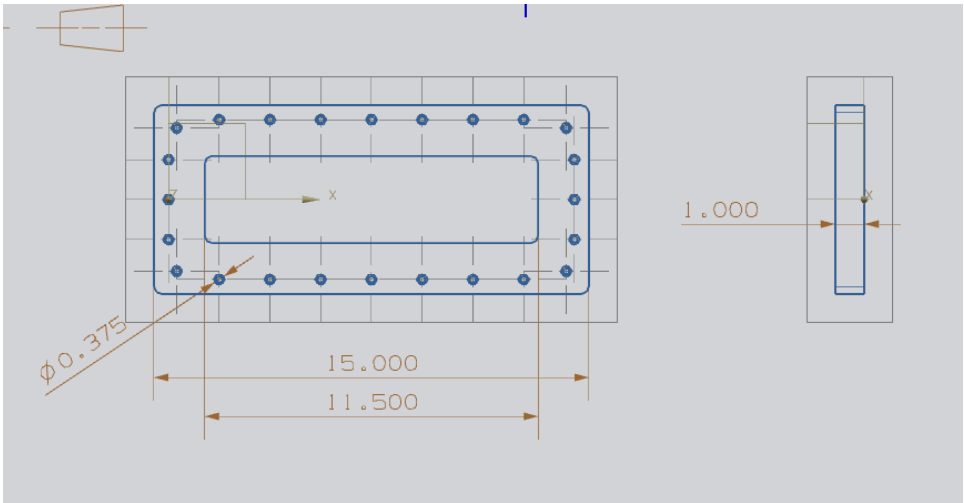

Figure 2.28 : Drafting of window cover

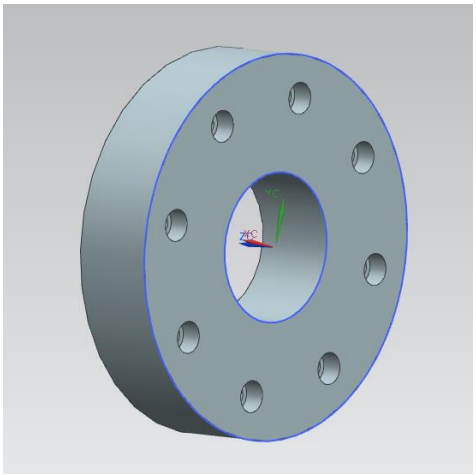

Figure 2.29 : Circular window cover

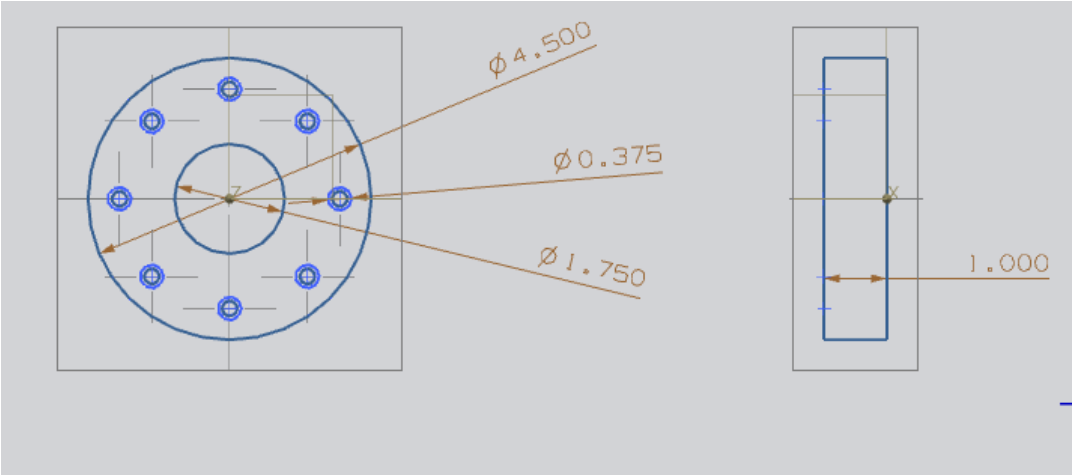

Figure 2.30: Drafting of circular window cover

2.5.6 Inner quartz chamber and quartz window: The designed combustion chamber has two different configurations –as a standalone stainless steel combustion chamber and with an inner quartz glass insert which gives optical access allows testing of chamber configuration. The quartz chamber has an outer diameter of 22.86 cm, inner diameter of 12.7 cm and total length is 63.5 cm. Quartz windows were purchased from Machined Glass Specialist Inc having the transmission spectrum shown in Fig 2.31 that gives a transmission percentage of approximately 90% at 532 nm wavelength (same wavelength that will be used for particle image velocimetry).

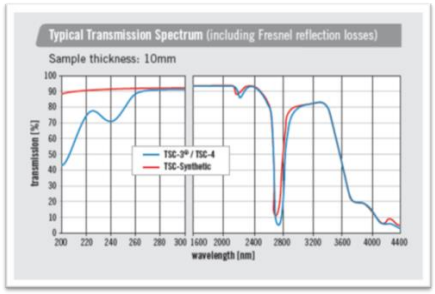

Figure 2.31: Quartz transmission spectrum

Figure 2.32: Squared quartz window

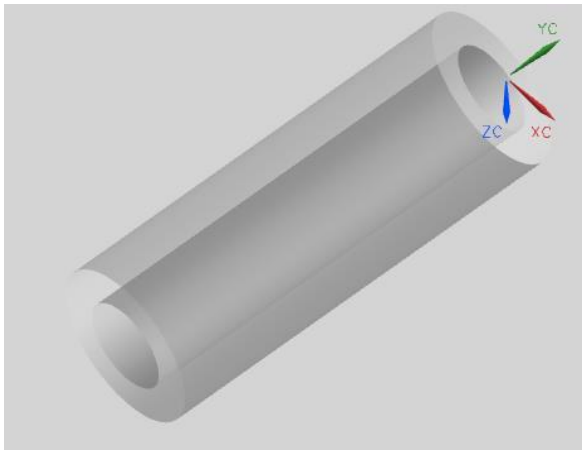

Figure 2.33: Inner quartz chamber

2.5.7 End Cap: The End cap acts as a connector between the combustion chamber and the exhaust and also it serves as a sealant to the main combustion chamber. The outer dimension of the end cap is 0.46 m in diameter containing a hole of 50.8 mm diameter for housing the converging nozzle. Eight 12.7 mm diameter stainless steel bolts were used to secure the end cap with the main combustor. The end cap is designed to have three different removable modular

sections- the converging nozzle, the nitrogen exhaust disk, and the outer main cap that connects the end cap to the main combustion chamber as shown in Fig 2.34. The main purpose of the converging nozzle is to the control the throat area in order to maintain the desired pressure inside the chamber. The main end cap acts as a sealant for the main combustion chamber as well as the link between the combustion chamber and the exhaust. The use of converging nozzle is to control the desired pressure inside the combustion chamber. Equation 1 was used to calculate the throat area in order to maintain 15 bar pressure inside the chamber and the calculated area is 161.29 mm^2. The design is shown in Fig 2.35 and it is attached to main combustion chamber by using 46.35 mm diameter stainless steel bolts.

$$A_T = \frac{\dot{m}\sqrt{RT_T}}{P_T\sqrt{\gamma\, Ma}}\left(1+\left(\frac{\gamma-1}{2}\right)Ma^2\right)^{\frac{\gamma+1}{2-2}\gamma} \tag{2.4}$$

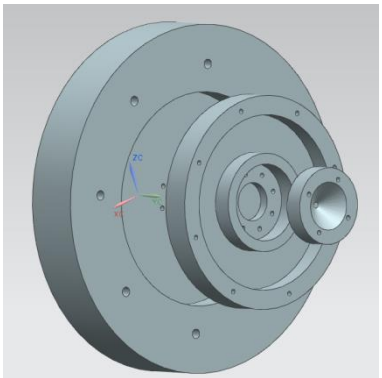

Figure 2.34: End Cap assembly

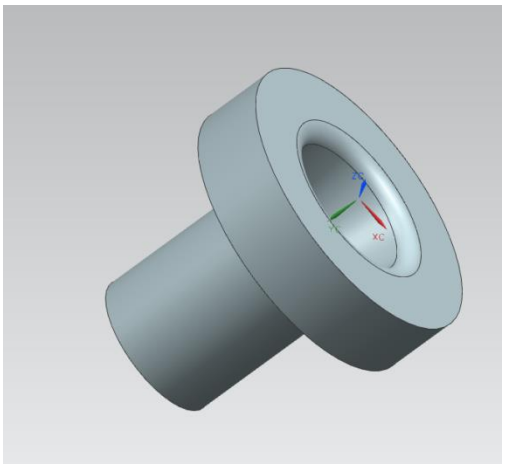

Figure 2.35: Converging nozzle

The nitrogen exhaust disk will be used when the inner quartz chamber will be used. This disc will be attached to the end cap as a middle part that will allow nitrogen to be exhausted through the end cap. A grouping will be made for the placement of the nitrogen exhaust disc and 6.35 mm diameter stainless steel bolts will be used to connect the disc with the main end cap. Since all the three parts for end cap are modular in design, it will be possible to replace the nitrogen exhaust disc when inner quartz chamber will not be used. Both configurations are shown in Fig 2.36 and Fig 2.37.

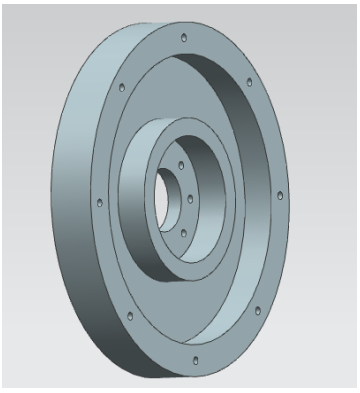

Figure 2.36: End cap having slot for quartz configuration

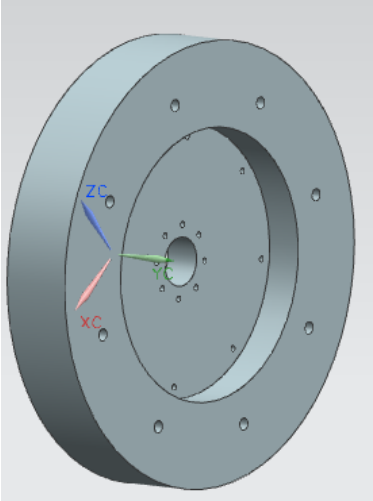

Figure 2.37: End cap without the slot for quartz tube

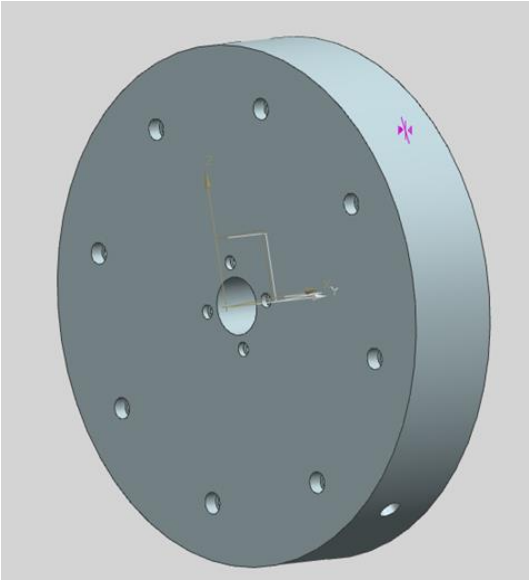

Figure 2.38 : Side view of the end cap

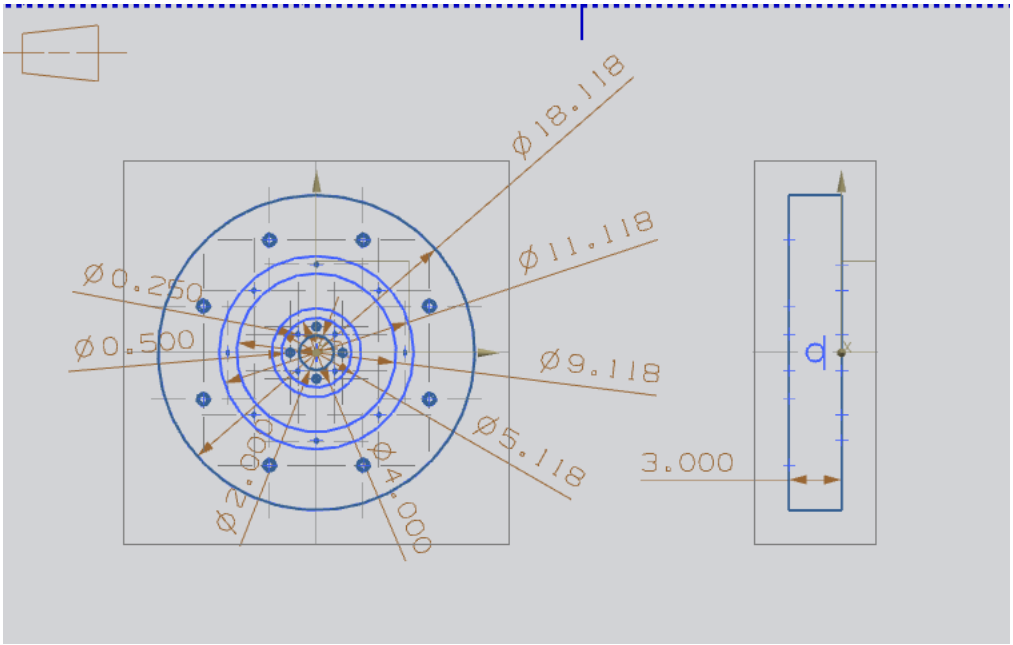

Figure 2.39 : Drafting of end cap

2.5.8 Cooling System: Finite element analysis suggests that a robust cooling system is necessary for both outer stainless steel chamber and inner quartz combustion chamber. Cooling system will allow combustor to sustain at high temperature. Because of the need of a cooling system, two different cooling systems have been designed individually –one is for the outer stainless steel chamber and the other is for the inner quartz combustion chamber.

A nitrogen distributor has been designed for cooling the inner quartz chamber. The distributor has a connecting tube attached that act as an intake of nitrogen flow. This distributor is hollow in the inner section that allows the nitrogen flow. There are a total of sixteen distribution holes in that design. In order to maintain the even distribution of the coolant, eight of them are pointed at 90^{o} angle and the other eight are pointed at 180^{o} angle towards the outer wall of the quartz chamber. The design of the cooling distributor can be seen in Fig 2.40 along with the cross section of the nitrogen flow in Fig 2.44.

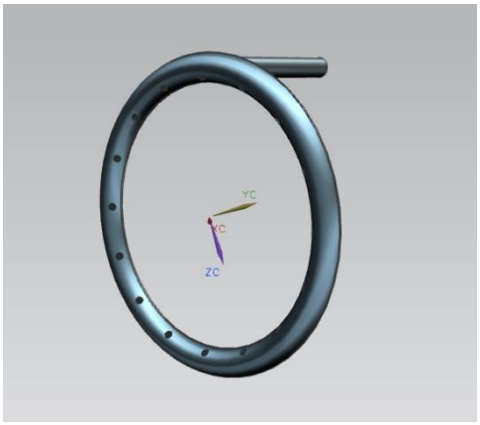

Figure 2.40: Nitrogen distributor

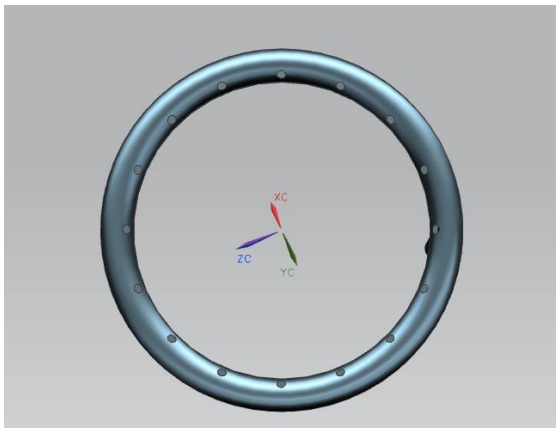

Figure 2.41 : Front view of nitrogen distributor

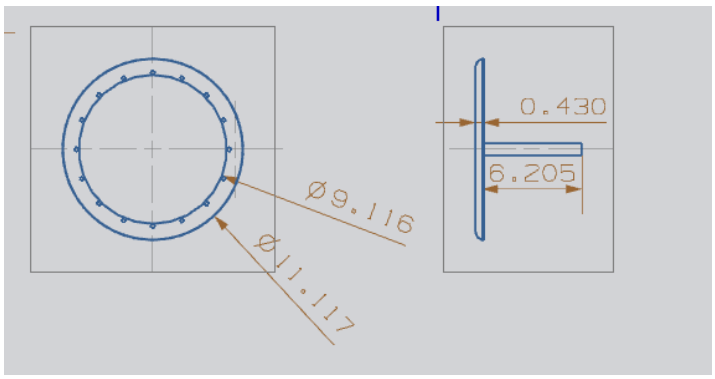

Figure 2.42 : Drafting for nitrogen distributor

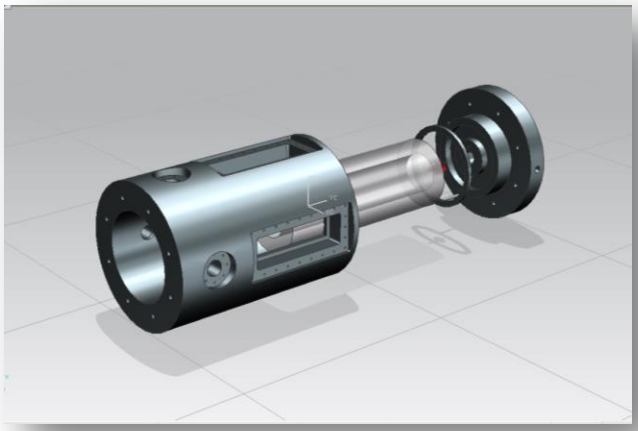

Figure 2.43 : Arrangement of N_2 distributor

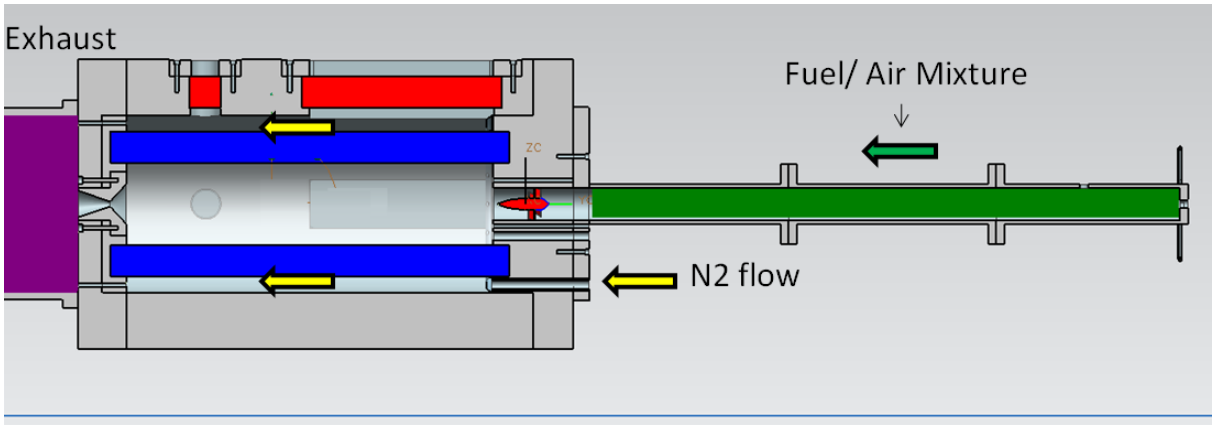

Figure 2.44: Cross section of N_2 flow

To reduce the thermal stress, a cooling system has also been designed for the outer stainless steel chamber. In this design, the outer chamber will be wrapped with copper coil as shown in Fig 2.45 and ethylene glycol will be used as the working fluid.

Figure 2.45: Stainless Steel chamber cooling system

2.6 Bolt specifications: Bolts were used throughout the design. The bolts used are medium carbon grade 8 alloy steel that has a minimum tensile strength of 1241.05 MPa, a proof strength of 965.26 MPa, and minimum yield strength 1054.89 MPa with a minimum Rockwell hardness of C39. All bolts have a black oxide finish that makes them rust resistant. For the front cap and end cap, the maximum stress applied on each bolt under our design operating conditions is rated at 93.9 MPa. The maximum stress applied on each bolt for circular window is 12.2 MPa and for rectangular window is 64.5 MPa.

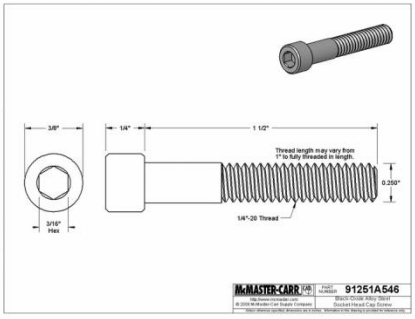

Figure 2.46: Window cover bolt [McMasters]

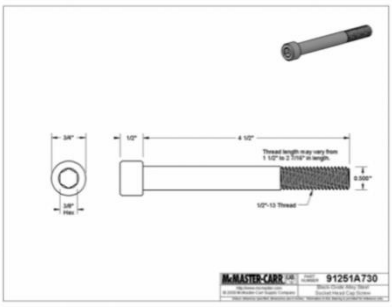

Figure 2.47: End Cap/ Front Cap bolt [McMasters]

2.7 Test Mounting: A test mounting has been designed for the combustor. This stand is designed to mount the combustor and to prevent the combustor from moving during experiment when thrust will be created. Four curvature supports have been made to secure the combustor. Removable wheels are used for the easy movement of the combustor; dampers will be used during the time of experiment. Two eye bolts that are attached to the top of the end cap and front cap will be used to mount the combustor. An engine lift will be used to place the combustor in the stand. Figure 2.48 represents the test stand. The stand is made out of 7.62 cm by 7.62 cm square tubing with thickness of 9.5 mm. The material used for the test stand is A36 Steel because of its low cost, availability and its property that satisfied the finite element analysis. The length and width of the stand is 0.83 m by 0.71 m with the height of 0.71 m.

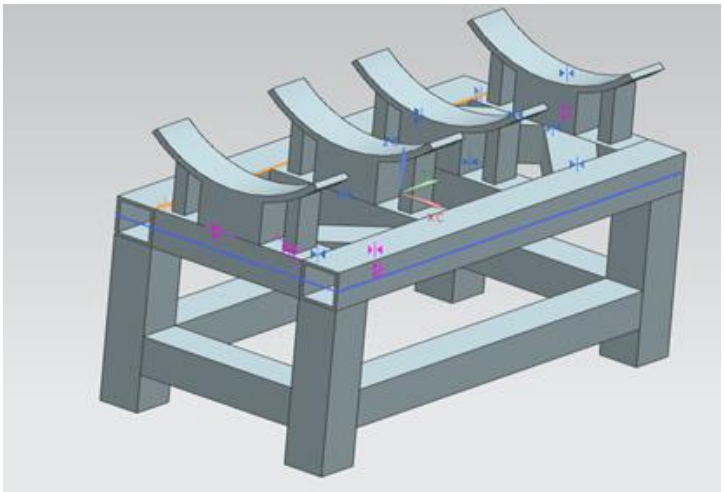

Figure 2.48: Stand for the combustor

2.8 Manufactured parts: All of the designed parts of the combustor have already been manufactured. The Computer Numerical Code (CNC) machine was used to manufacture the parts very precisely. Main chamber has been manufactured and assembled with all of the necessary parts. All manufactured parts are shown in Fig 2.49-2.53. Figure 2.54 shows the complete combustor assembly.

Figure 2.49: Inlet manifold

Figure 2.50: Rectangular window cover

Figure 2.51: Stainless Steel Instrumentation Port

Figure 2.52: Converging nozzle

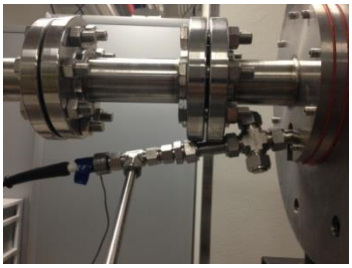

Figure 2.53 : Igniter assembly

Figure 2.54: Combustor in the stand with exhaust

2.9 Control System: The schematic of the delivery system is illustrated in Fig 2.55. The control system is operated remotely using Lab View. Proportional flow control valves are integrated to regulate the flow. Proportional control valves are programmed with DAQ cards that can send either a voltage signal or an ampere signal to the valves. Needle valves are also installed in order to regulate the flow precisely. Flow meter that is integrated in each line provides the visual measurement of the flow for each line. A shut off system is installed by using solenoid valves that will help to shut off the lines as per need and this is also controlled remotely using Lab View. A manual emergency shutdown has been integrated in order to shut off the entire system in case of any emergency. A spark plug ignition system is also being controlled remotely using Lab View.

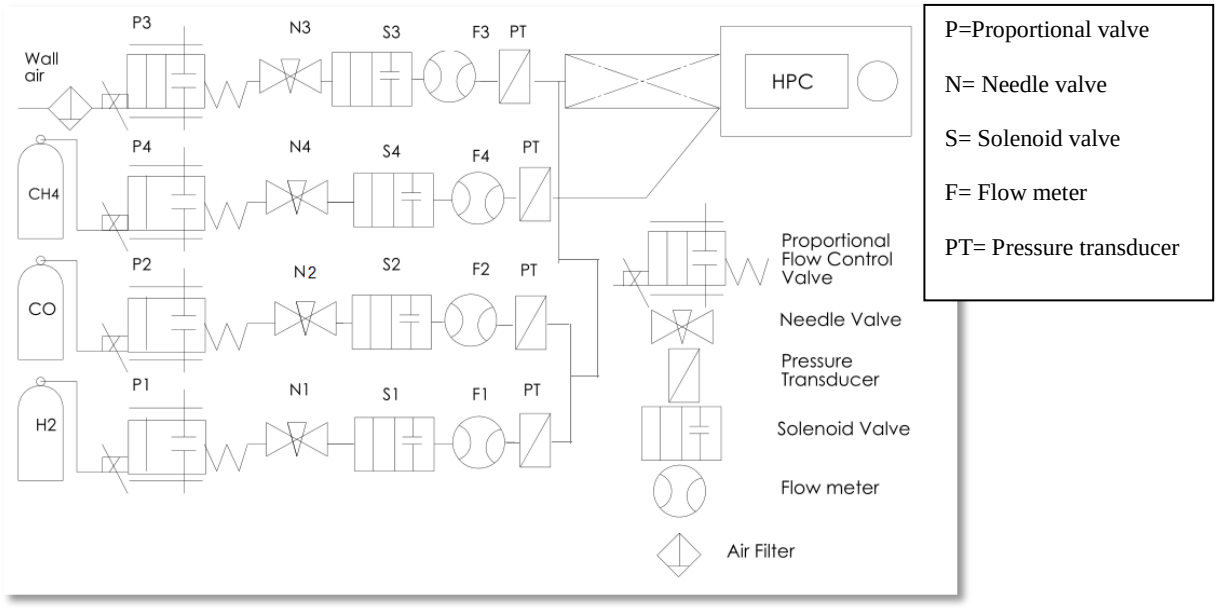

Figure 2.55: Schematic of control system

2.10 Components of Control system

2.10.1 Solenoid valves: Solenoid valves were selected from Jefferson valves (model number 1314IA06T). Solenoid valves as shown in Fig 2.56 are actuated with a 120 VAC signal. They are made of 316 Stainless Steel and normally closed two way valves. This specific model was chosen because of required pressure differential of 1.5 MPa and their 0.02 m connection that is needed for designed piping system. Connection was manufactured to power up the valves. In order to provide the necessary power, cables were rewired and terminal blocks were used to distribute the 120 VAC signal to all valves.

Figure 2.56: Jefferson Valve 1314 Series

2.10.2 Proportional flow control valve: Proportional control valves that have been integrated into the system are EH2 series from KZ Valve and they are actuated with a 12 VDC signal. Figure 2.57 demonstrates the EH2 valve. They are two way valves and operated by a motor to turn a stainless steel ball valve in order to regulate the flow. These valves are rated up to 1000 psi and can be regulated with an output of 0-10 VDC.

Figure 2.57: KZ Valve EH2 series

2.10.3 Flow meters: Flow meters- FMA 1843-1845 from Omega were used to measure the gas flow. These flow meters were selected based on their flow measurement capacity as per required for the experiment. Flow meters are connected to the USB 6008 DAQ 1) and to the power supplies. In order to power the flow meters and communicate with the computer, Pins number 2-5 were used as shown in Fig 2.58. They require an excitation voltage of 12 VDC and current of 0.2 ampere. Numeric displays as shown in Fig 2.59 allow the visual observation of the flow rate that allows comparing the flow rate with the graphical interface.

Figure 2.58: Flow meters 1800 series

PIN	FUNCTION
1	Remote LCD display signal
2	0 to 5 VDC output indication
3	0 to 5 VDC common
4	Power supply, positive
5	Power supply, common
6	Remote LCD display reference
7	(unassigned)
8	4 to 20 mA output indication
9	4 to 20 mA common

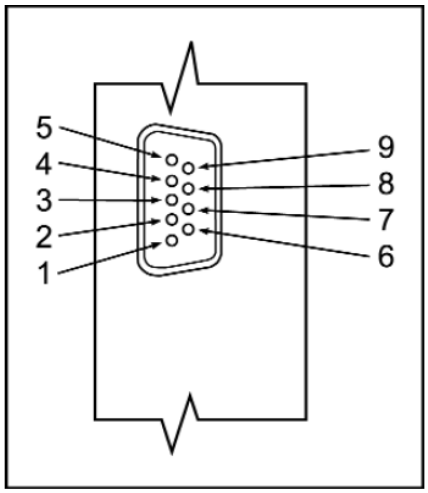

Figure 2.59: Pin out of the flow meter

2.10.4 Pressure Transducers: Pressure transducers were also installed in the system in order to measure the line pressure. Omega pressure transducers PX309-300G5V as shown in Fig 2.60 were integrated into the system. This pressure transducer requires an excitation voltage of 9-30 VDC. The wring connection for the pressure transducer is illustrated in Fig 2.61.

Figure 2.60: Omega PX309-300G5V pressure transducer

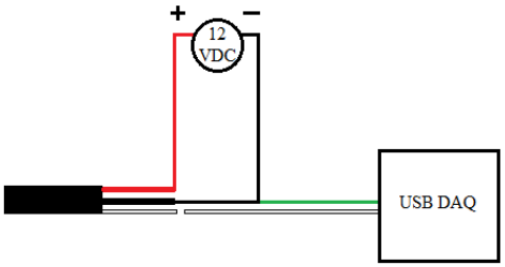

Figure 2.61: Wiring connection for Pressure Transducer

2.10.5 Electrical characteristics of the components: In order to delineate the requirement for the control of the flow, a detailed analysis was executed to analyze the electrical characteristics of the instrumentation that used in the system which makes the hardware function accordingly. Four solenoid valves, four needle valves, four proportional control valves are integrated to operate the system efficiently. Table 2.7 summarizes the characteristics.

Table 2.7: Electrical Characteristics of Components

Purpose	**Hardware components**	**Number**	**Electrical characteristics**
Control	solenoid valves	4	Excitation:120 VAC
	proportional control valves	4	Excitation:12VDC
			Output: 0-10 VDC
Measurement	pressure transducers	3	Excitation: 9-30DC
			Output: 0-5 VDC
	Mass flow meters	4	Excitation: 0-12 VDC
			Output: 0-5 VDC

2.10.6 Power supply: Extech 382270 Power Supply as shown in Fig 2.62 was used to deliver the power for flow meters and pressure transducers. Mastech DC power supply as shown in Fig 2.63 was used to provide power for proportional flow control valves. Extech power supply has four outputs: two 0 to 30 V with a maximum of 5 A, one 3 to 6.5 V with a maximum of 3 A and one 8-15 V with a maximum of 1 A.

Figure 2.62: EXTECH Instruments 382270 Power Supply

Figure 2.63 : MASTECH DC power supply

2.11 Wiring of the instrumentation: Two different types of wiring was done by using two different types of wire: one is from Grainger for solenoid valves which is a gage 12 AWG stranded wire and the other one is the multi-paired wire from Mouser Electronics to connect the

proportional control valves with the DAQ. The first one from Grainger was selected due to the 120 VAC supply needed for the solenoid valves and it is rated up to 600 V and 20 A. The second wire from Mouser Electronics has four gage 18 AWG wire and it is rated up to 300 volts.

2.12 Hardware Components: Hardware components consist of two USB DAQ and a PCI card from National Instrument (NI). The USB-6008 has eight ±10 V analog inputs and two 0-5 VDC analog outputs. Two USB-6008 were used in order to control proportional valves, flow meters and pressure transducers. Solenoid valves are controlled by PCI-6521 with the mechanical relay outputs. This PCI has eight mechanical relay outputs with 150 V AC or DC. Both PCI and DAQ are illustrated from Fig 2.66 to 2.68. PCI 6521 is a relay card that was used to actuate the solenoid valves and also the igniter coil. On the contrary, the USB 6008 has both analog outputs and inputs. First DAQ was used for flow meters and two proportional valves and second DAQ was used for pressure transducers and two proportional control valves. The valve assignment in Lab VIEW was executed by following the pin outs of the respective hardware accessory.

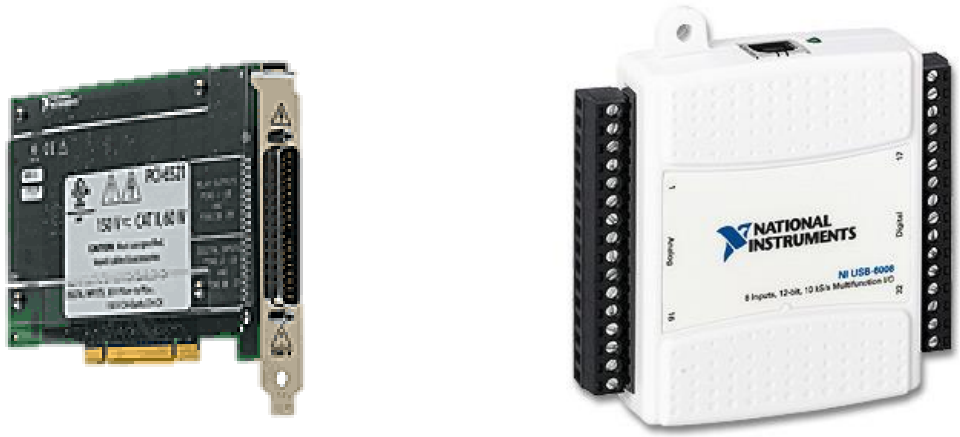

Figure 2.64: USB DAQ-6008

Figure 2.65 : PCI 6521 card

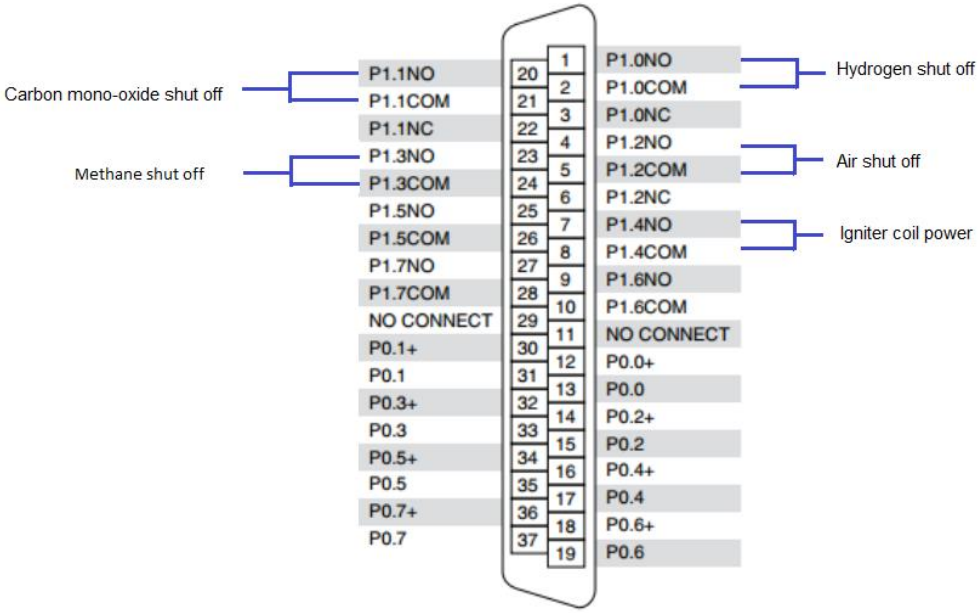

Figure 2.66: NI PCI-6521

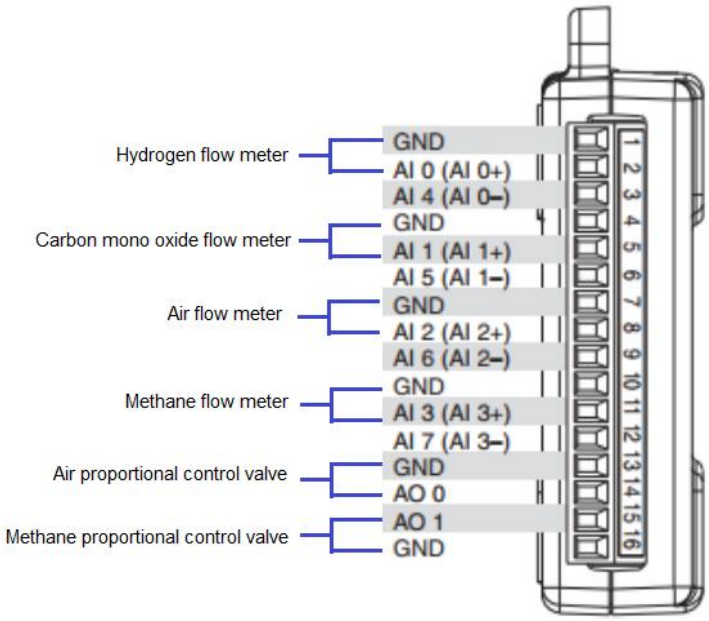

Figure 2.67 : USB DAQ-6008 (DAQ 1)

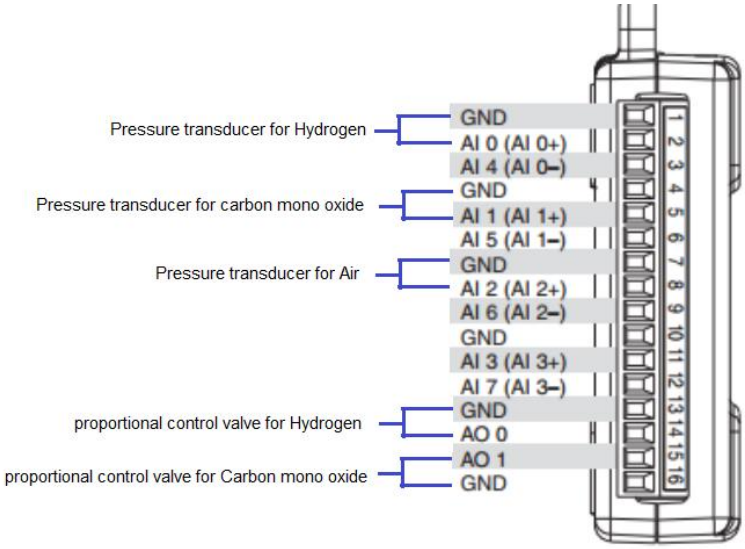

Figure 2.68 : USB DAQ-6008 (DAQ 2)

2.13 Hardware components of the ignition system: MSD 8247 multi-spark coil was used to create the necessary discharge that is needed for the spark plug. Figure 2.69 illustrates the MSD 8285 and its connection pin out. This coil requires a frequency of 100 Hz and a 5 V input. The frequency and voltage were provided by using a signal generator and a 12 V battery respectively. In order to provide all the required components, three pin connectors were used as shown in Fig 2.69. Mouser Electronics 18 AWG cables were used for all the necessary connections. Wiring was done as follows: Red – 12 V Battery positive to 12 V in coil, White – Coil input to PCI 6521 to signal generator, Green – Coil ground to 12 V battery negative, Black – 12 V Battery negative to spark plug ground.

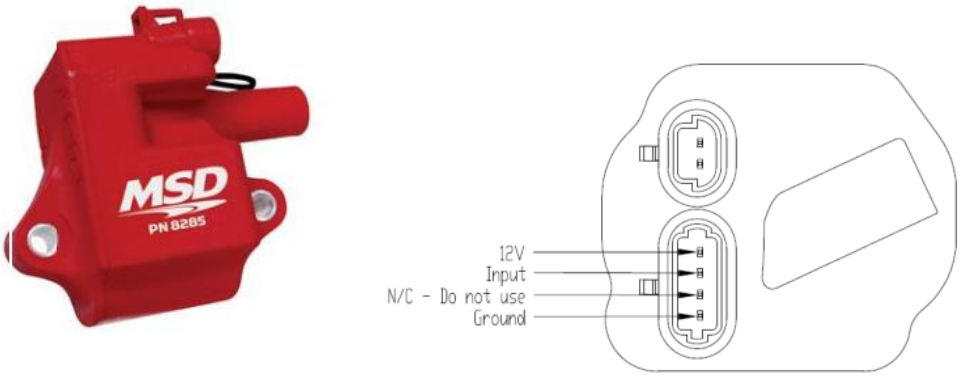

Figure 2.69: MSD 8285 and its connection pin out

In order to abstain from any undesired current, a negative battery connector was grounded to the power supplies. Green cables were used for grounding. Figure 2.70 illustrates the battery connector showing all its necessary components.

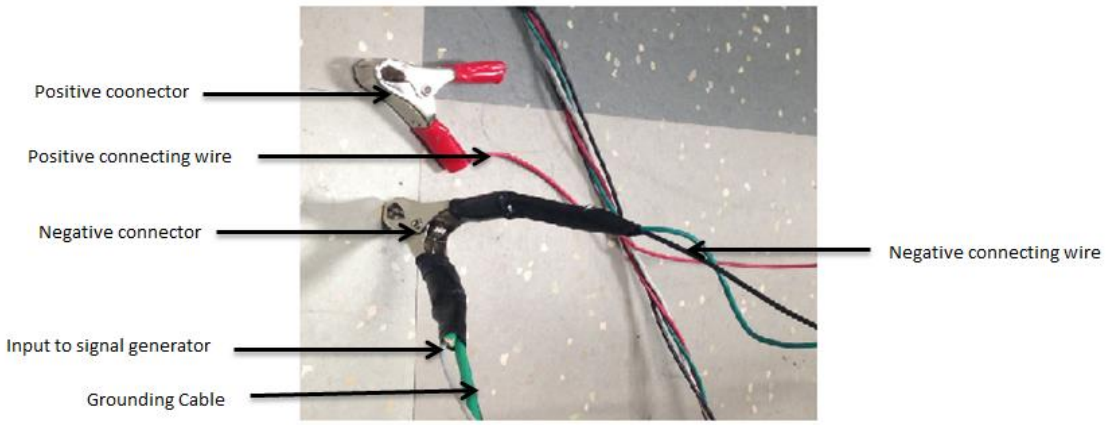

Figure 2.70: Negative battery connector

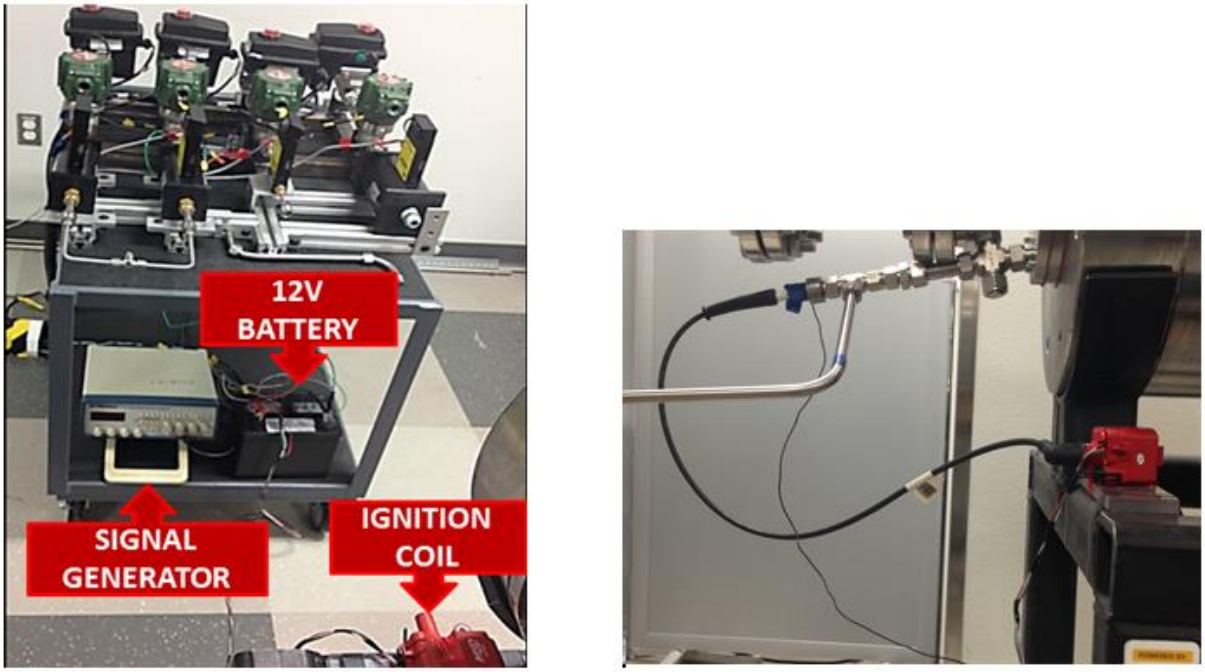

Figure 2.71 : Ignition system set up

2.13.1 Signal generator: In order to generate the 100 Hz frequency that is required for the coil, a BK Precision 4012A signal generator was used as shown in Fig 2.7**2**. A Transistor-transistor logic (TTL) channel was used. The reason of using TTL channel is that the output channel gives 14 V which can burn the coil and also coil will not turn on unless the TTL 5V signal is sent via Lab VIEW which ensures the user's control over the TTL signal and coil ignition. A 12 V battery was used to provide the required charge for the spark plug. The Bayonet Neill-Concelman (BNC) cable was used in order to connect the positive and negative wires.

Figure 2.72: BK Precision 4012A Signal Generator

2.14 Integration of the hardware components: After all the hardware set up was completed, configuration of Software was executed in Lab VIEW that provides the user with a graphical interface and allows remote operation as well as monitoring. Fig 2.77 demonstrates the configuration for the PCI 6521 card that is used for control of the solenoid valves and igniter. Figures 2.73 to 2.76 demonstrates the configuration for DAQ 1 and DAQ 2

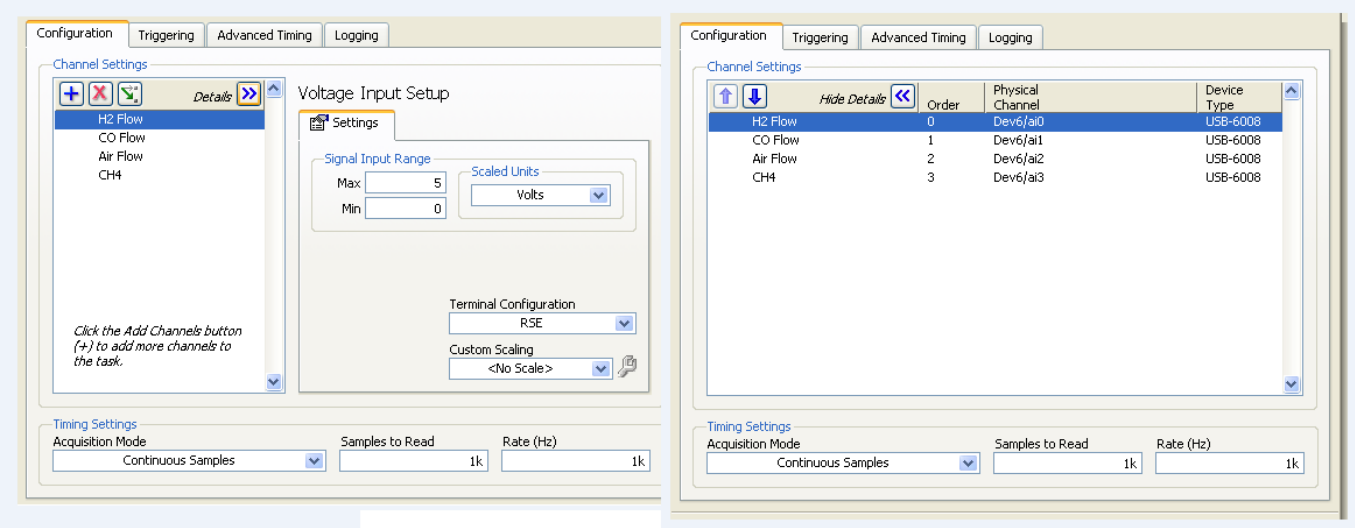

Figure 2.73: USB DAQ-6008 (DAQ 1) Configuration for flow meter

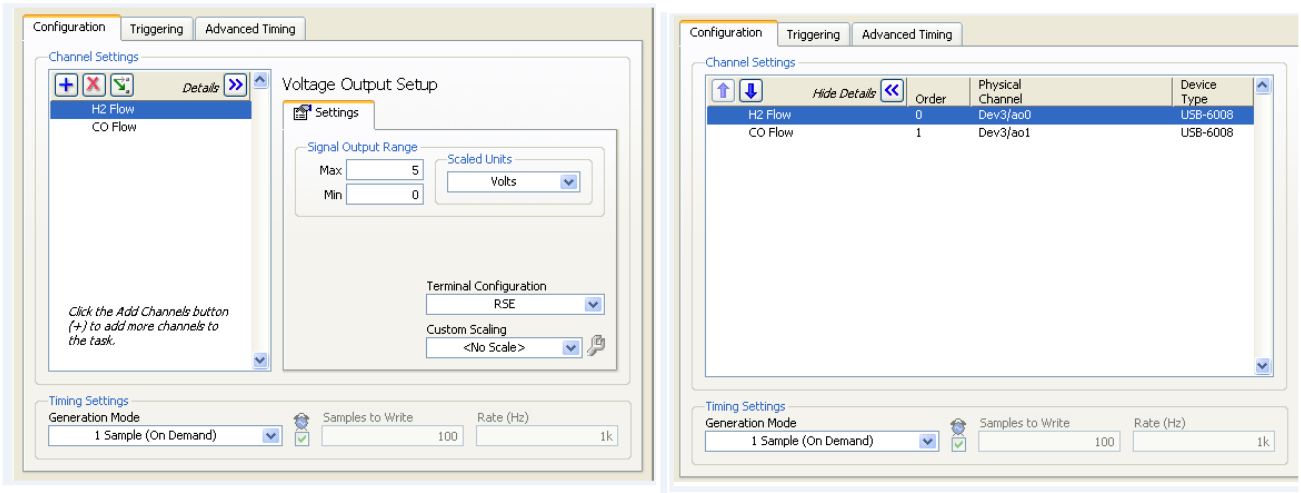

Figure 2.74 : USB DAQ-6008 (DAQ 1) Configuration for proportional valve

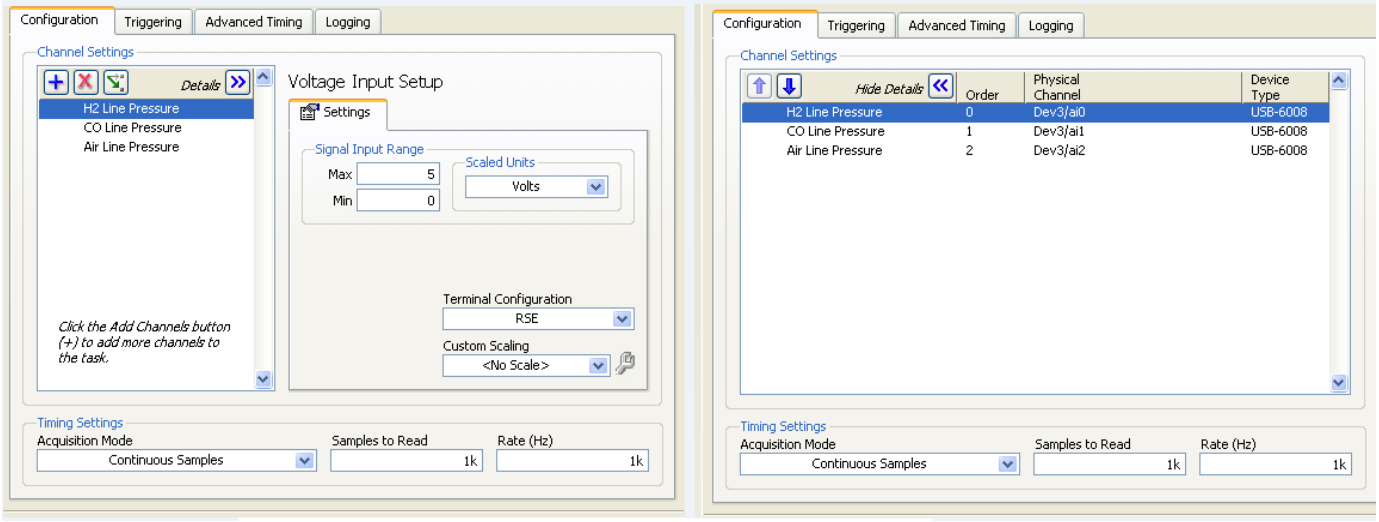

Figure 2.75 : USB DAQ-6008 (DAQ 2) Configuration for pressure transducers

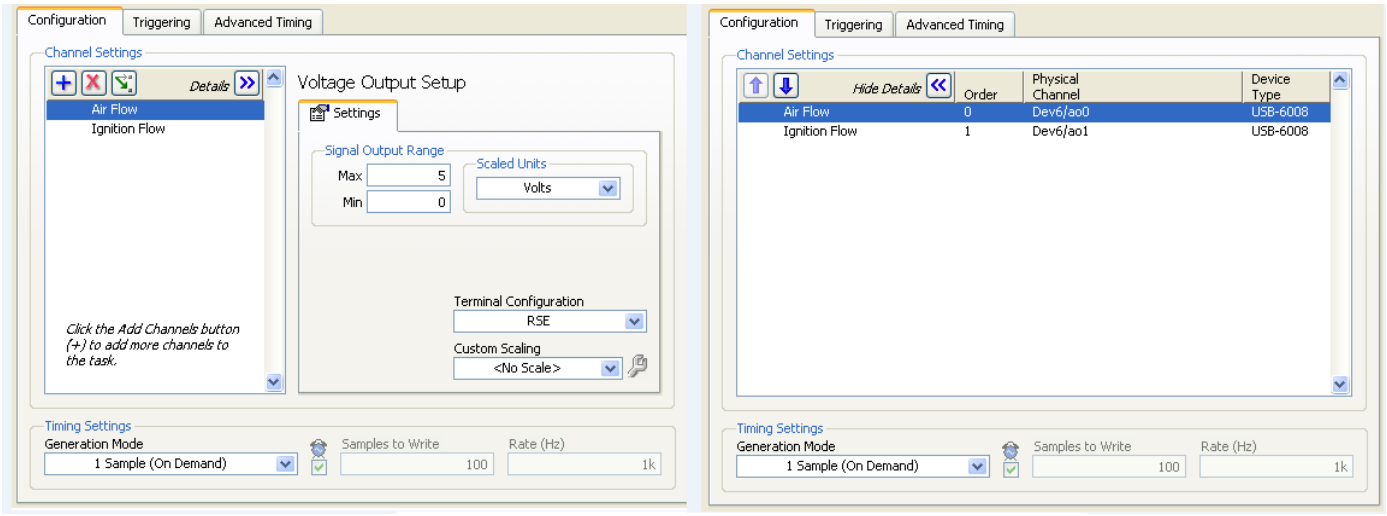

Figure 2.76 : USB DAQ-6008 (DAQ 2) Configuration for proportional valves

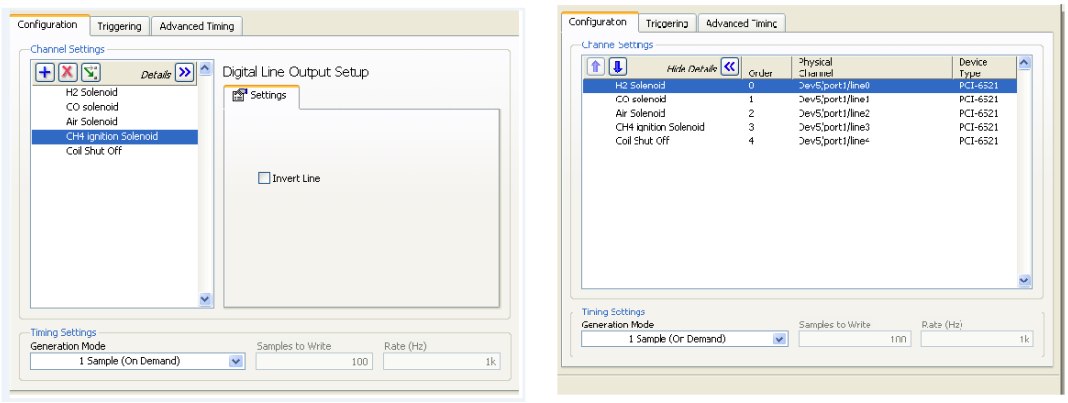

Figure 2.77: PCI 6521 Configuration

2.15 Graphical user interphase configuration: In order to make easy observation and control of the experiment, all controls and sensors are integrated in the same window. By changing the voltage from 0-5 volts, expected flow control can be maintained by proportional control valves. Actuation of solenoid valve is mandatory to make the line opened. A green light in the panel is the indication of the opened valve which ensures that flow can go through. Figure 2.78 illustrates the graphic interface panel for the control system that is designed for this high pressure combustor.

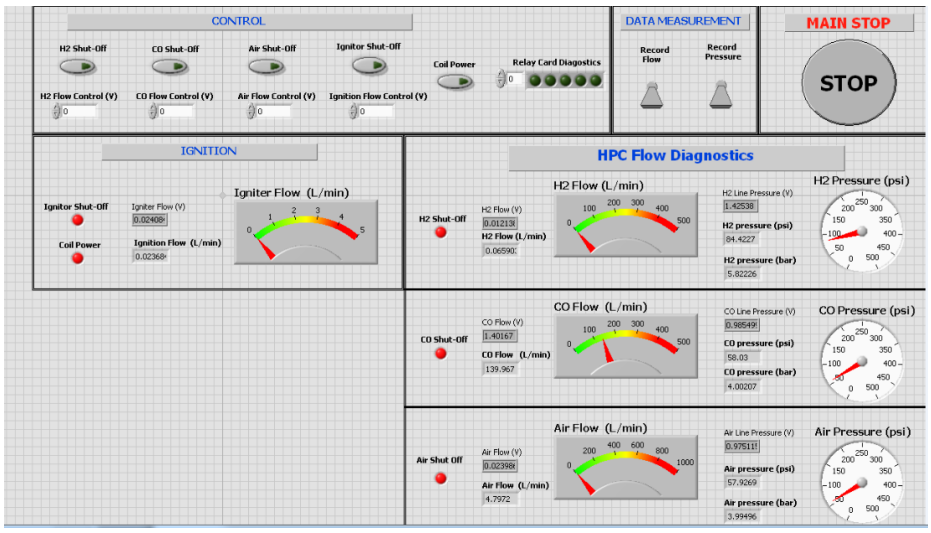

Figure 2.78 : Graphic Interface Panel for the HPTC

2.16 Data Acquisition: Data are recorded by using the "Write to Measurement File" tool in Lab View that facilitates to save data in a series of files indicating the date and time of testing which allows further investigation of data. Data is acquired and recorded using DAQ. The output signal acquired by the DAQ from the instrumentation is represented in the graphical interface panel that allows visual observation. The user can know the status of the flow both graphically and numerically by a series of indicators. Figure 2.79 illustrates the VI for data acquisition and recording of proportional control valves, flow meters and pressure transducers

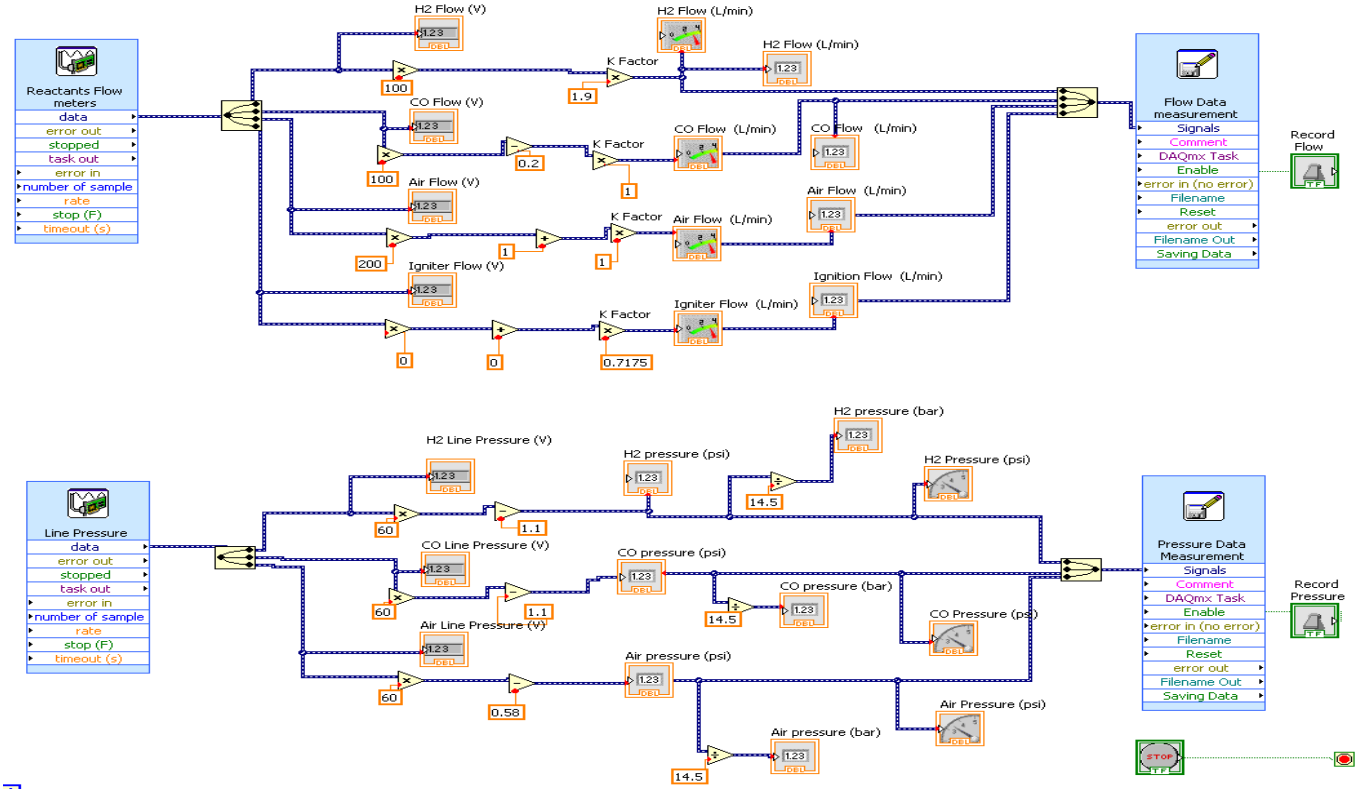

Figure 2.79: Data Acquisition and Recording Logic

2.17 Logic for solenoid and proportional control valve: Relay card diagnostics allows the user know about the status of the line whether it is closed or opened and also informs about the status of igniter coil. A numeric controller controls the proportional valves and then it is converted into dynamic data. Switches are used to control the solenoid valves. A green light indicates that the relay is on and functioning. All logic is placed in a loop and it repeats the sequence until the stop button is pressed. The logic circuit programmed is split into four parts: proportional valves, solenoid valves, pressure transducers and data, the signal from all the buttons is sent into an array. Figure 2.80 illustrates the logic for the proportional valves and Figure 2.81 illustrates the logic for the solenoid valve control.

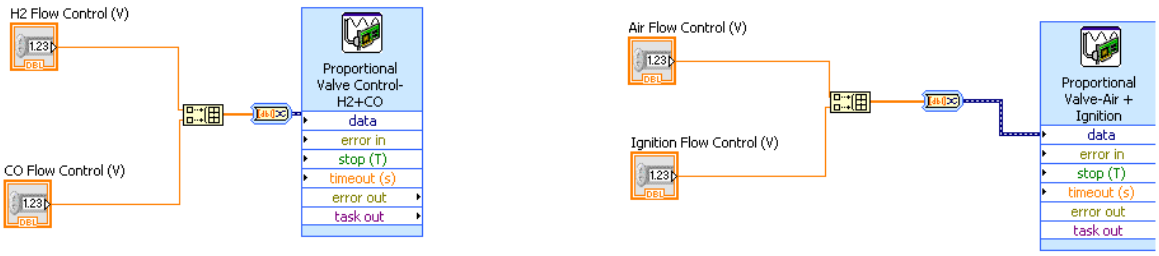

Figure 2.80 : Logic for proportional control valves

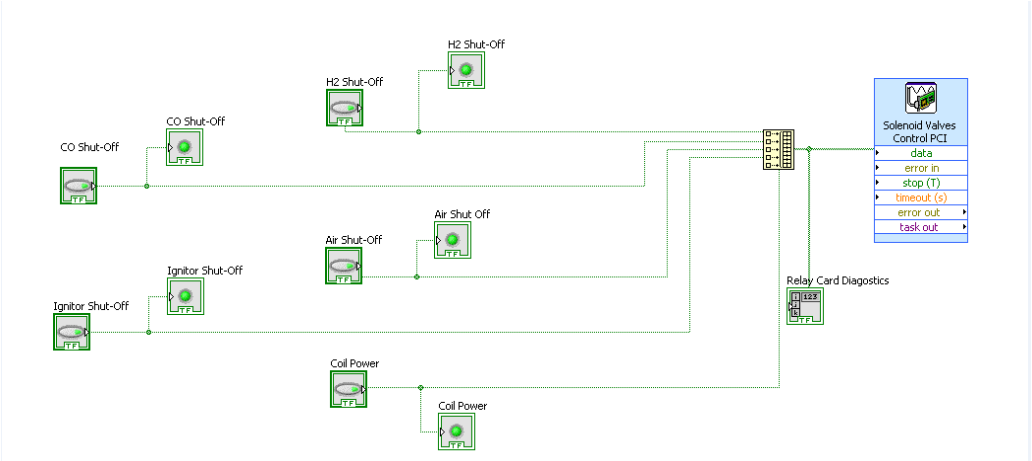

Figure 2.81: Logic for solenoid valve control

2.18 Adaption of PCI and USB DAQ: Fig 2.82 illustrates the adaptation of PCI and USB DAQ to the control system and also the power supplies. Red cables deliver the 120 V to the positive lines, and black cables deliver the 120 V to the negative lines. From the left, first 16 terminal blocks are used for flow meters, next 16 terminal blocks are used for proportional control valves and last 12 terminal blocks are used for pressure transducer. A movable cart was used to accommodate solenoid valves, proportional control valves, flow meters and ignition components.

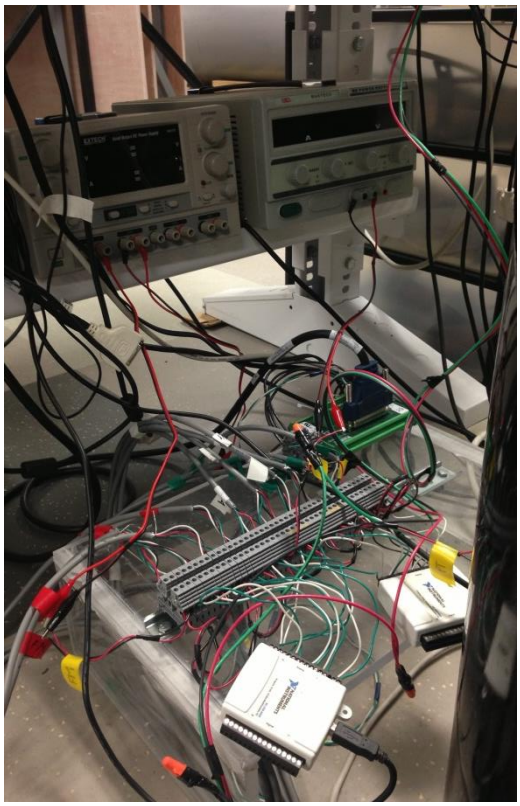

Figure 2.82: Adaptation of PCI and USB DAQ with power supplies

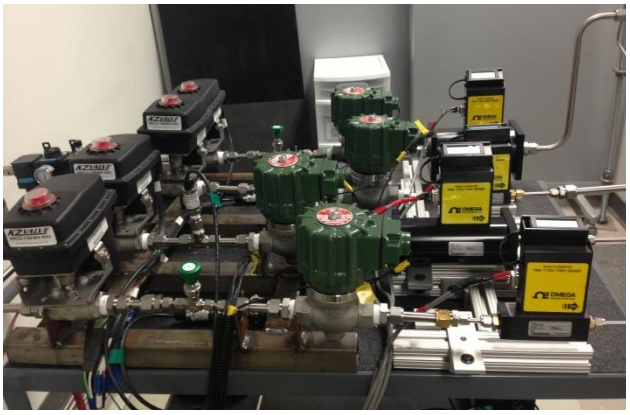

Figure 2.83: Valves arrangement

2.19 Testing: Functional testing, Leak testing, pressure testing, and ignition testing were carried out in order to evaluate the performance of the system. RTV glue and alumina polycrystalline fibers were used to make the combustor leak proof

2.19.1 Functional testing: Functional testing of all instrumentation was carried out in order to make sure that the entire control system would be operational. In order to prevent any excess current discharge, the system is grounded to the 120 V socket. After turning on the power supply, all mass flow meters were checked and the initial reading of 0 L /min of flow meter that ensures its functionality. Ignition coil was checked when it was actuated in order to make sure a spark is present. Simultaneously pressure transducer reading was checked to have the reading of 0 KPa. Solenoid valves were shut off and shut on in order to make sure their functionality. Voltage was changed ranging from 0-5 volt to operate the proportional valves.

2.19.2 Pressure testing: Leak and pressure tests were done simultaneously. Air pressure was tested at the pressure of 758 kPa which is the maximum pressure of the current compressor while methane line was tested at the pressure of 207 kPa. Pressures were verified from the reading of

the pressure transducer. Leak testing was carried out in the combustor and the lines by using snoop.

2.19.3 Ignition testing: The main purpose of this test is to evaluate the installed control and ignition system. The first step was to get the stable pilot flame to ignite the main fuel stream. Methane line was connected at a flow rate of 1 L/min and at the same time the spark plug was actuated to obtain aflame. A stable diffusion flame was obtained by regulating the flow from 1to 5 L/min. Figure 2.84 illustrates the diffusion flame in the chamber.

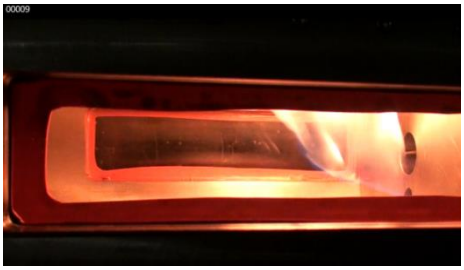

Figure 2.84: Diffusion flame

After getting the diffusion flame, air was introduced using different flow rates varying from 1- 5 L/mi and a stable flame was found as shown in Fig 2.85 by maintaining the air flow rate of 5 L/min. Then methane was introduced at the flow rate of 9 L/min and the pilot was shut off to see the stability of the flame as shown in Fig 2.86.

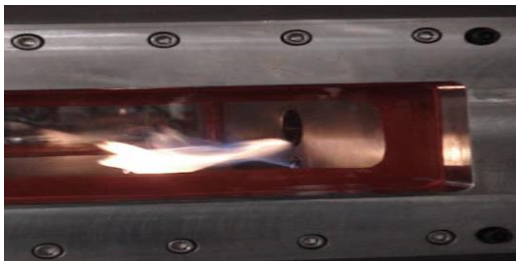

Figure 2.85: Stable pilot flame after introducing the air

Figure 2.86: Stable flame

Chapter 3 : Experimental Procedure

For this study a high pressure gas turbine combustor was used in order to study the effect of multi-tube injector geometry on flame stability and NO_x emission. The combustor rig has four configurable modules: (1) inlet manifold with static mixture, (2) Front cap and (3) optically accessible combustion chamber (4) End cap.

The combustion chamber integrates an ignition system where a diffusion pilot flame is used to ignite the main fuel-air stream. The fuel and air enter the inlet manifold through five alternate injection holes. The fuel-air mixture is then passes through the static mixture section of the inlet manifold in order to eliminate any injection induced flow irregularities as well as to ensure proper mixing of air and fuel. Combustor can accommodate both swirler and multi-tube injector. For the present study, initially swirler was used to do the functional testing of the equipment and also for ignition testing. Finally flame stability and NO_x emission measurements were carried out using multi-tube injector.

3.1 High pressure combustor: The combustion chamber is constructed in a cylindrical-type cross-section having quartz window to provide optical access to the measuring instrumentation. The chamber is also fitted with variable area flow restrictor in order to maintain desired pressure inside the combustor. This can be operated up to 15 MPa pressure and has a maximum power rating of 25 kW. Figure 3.1 illustrated the schematic diagram of the combustor.

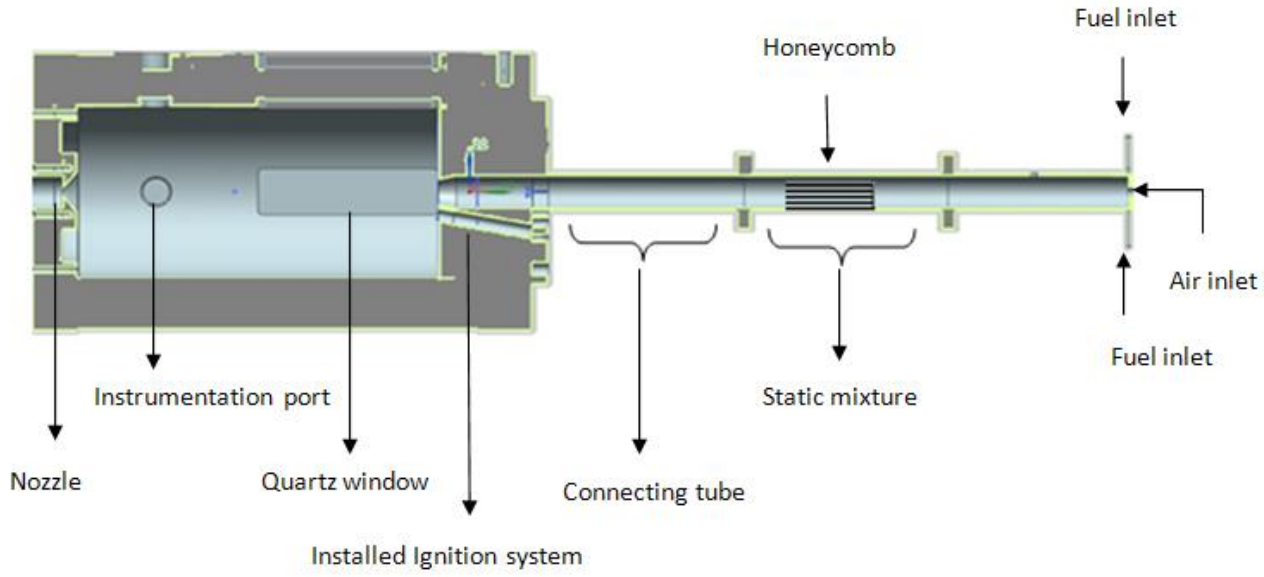

Figure 3.1 : Schematic diagram of combustor

3.1.2 Swirler: For this study a center body swirler with 12 vanes and a swirl number of 0.97 was used as shown in Fig 3.2 and 3.3 in order to do the initial functional testing of the equipment and to measure the NO_x emission for swirl stabilized flame. Swirl number is defined as the axial flux of swirl momentum divided by the axial flux of axial momentum, times the equivalent nozzle radius. The swirl number is related to the angle of a swirl vane and the geometry of the hub and can be calculated by the following equation

$$\boldsymbol{S} = \frac{\mathbf{2}}{\mathbf{3}}\left[\frac{\mathbf{1}-\left(\frac{d_h}{d}\right)^{\mathbf{3}}}{\mathbf{1}-\left(\frac{d_h}{d}\right)^{\mathbf{2}}}\right] \tag{3.1}$$

Where d and d_h are nozzle and vane pack hub diameters, respectively. The centerbody of the swirler is made out of stainless steel and the body is made of aluminum which was anodized for higher temperature resistance.

Figure 3.2 : Sketch of the swirler

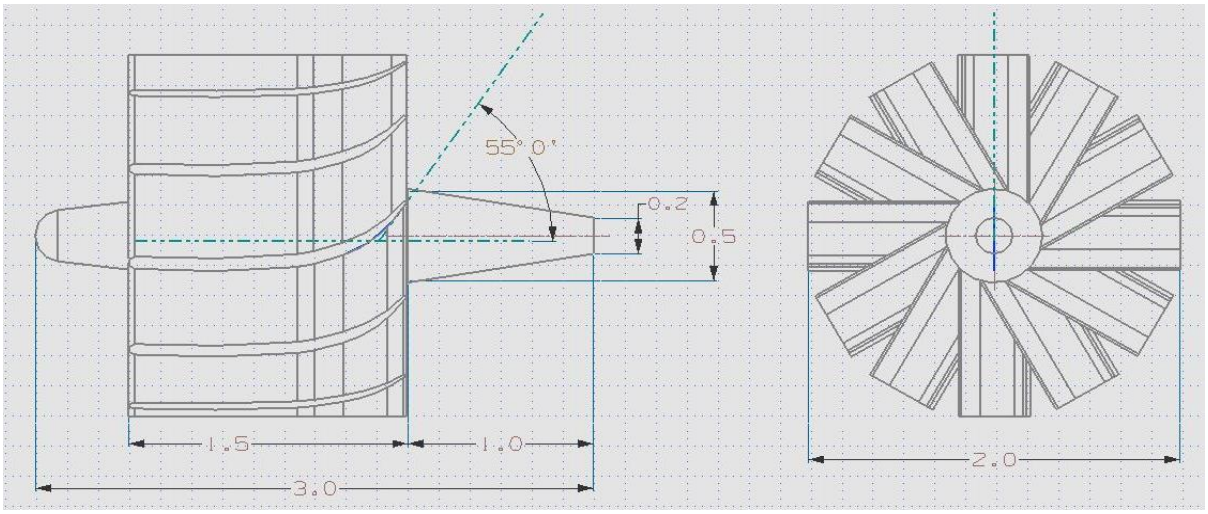

Figure 3.3 : Cross section of the swirler

3.1.2 Injector: Injector has three different parts-(1) Injector head. (2) Connecting tube. (3) Base. All the components are made of Stainless Steel 410. Injector head as shown in Fig 3.4 is made out of a converging disc. This disc is converged from diameter 0.05 to 0.03 m. It consists of 13 orifices having diameter of 0.004 m and depth of 0.02 m. Closest orifices are apart by 7 mm while the distant orifices are apart by 10 mm.

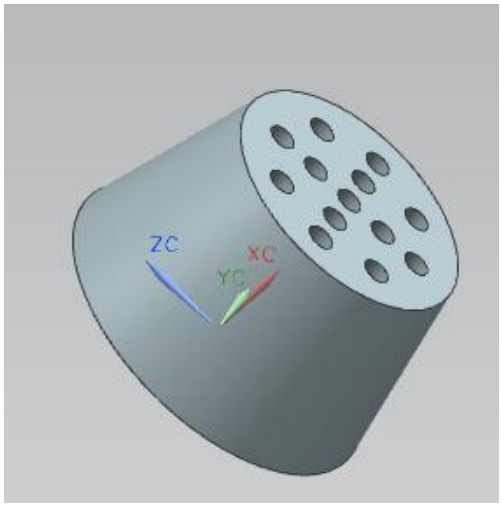

Figure 3.4 : Injector head

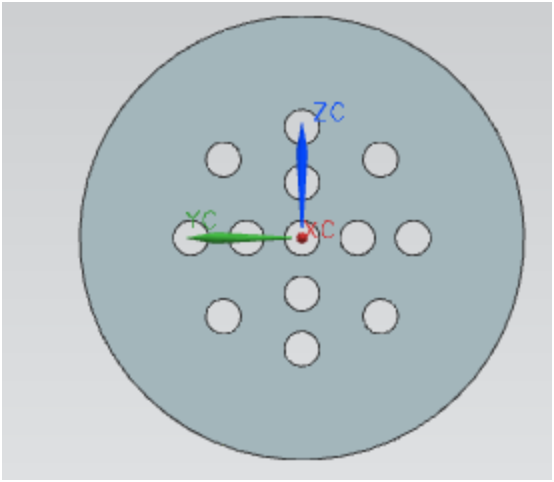

Figure 3.5 : Top view of the injector

Connecting tube connects the injector head with the injector base. Connecting tube has diameter of 0.03 m and height of 0.1 m. a grouping was made as shown in Fig 3.7 at the bottom side of the injector to wield it with the connector. Injector base connects the injector to the front cap of the combustor. The base has the diameter of 0.02 m

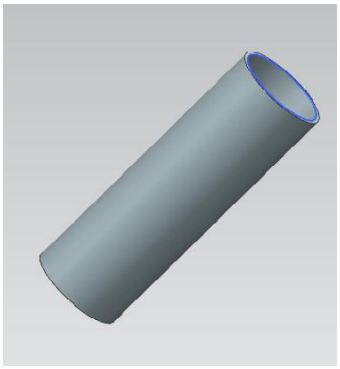

Figure 3.6 : Connecting tube

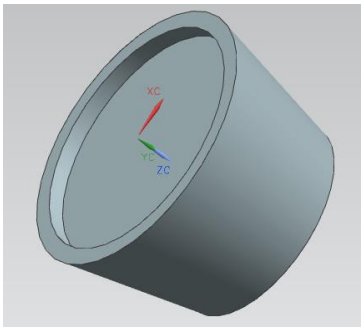

Figure 3.7 : Grouping in the injector head

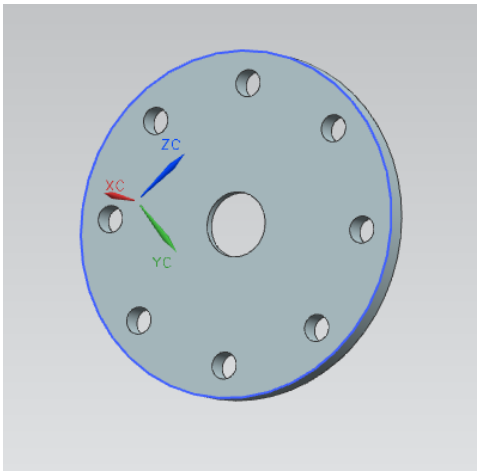

Figure 3.8 : Injector base

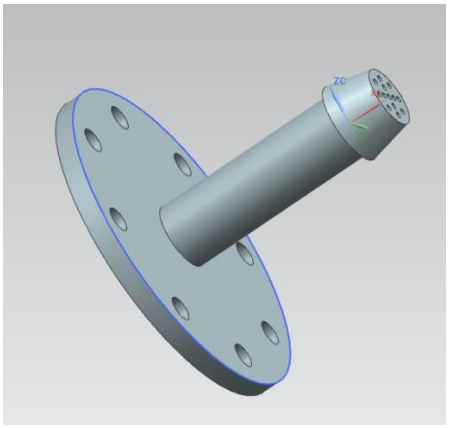

Figure 3.9 : Injector assembly

3.2 Flow measurement devices: Air was supplied to the rig through a high pressure rotary screw type compressor. All the gases (CH_4, H_2, CO, N_2, and Air) are stored separately in gas cylinders under 1600 psi pressure. The purity of these gases is 99%. Different flow meters are used in this experiment to control the volumetric flow rate which ranges from 0 to 1000 LPM. Proportional control valves and needle valves were used to control the flow rate.

3.2.1 Mass flow meter: A mass flow meter consists of a sensor tube and a monitoring component. The sensor tube contains a metal coil that can be heated in order to increase the temperature of gas passing through it. It also consists of a sensor on the end which can detect the volume of the gas. In order to measure the flow of a gas, it is passed through the sensor tube of the mass flow meter. The heating coil increases the temperature of the gas that causes its volume to increase too. The temperature is raised to a point set by the flow meter's user and this is the temperature at which the volume and mass of the gas under regular conditions is known. In order to determine its volume or molecular mass, the sensor at the end of the tube begins reading the volume of the gas when it passes through. The concentration of the gas particles within the volume indicates how much actual gas is flowing through the system.

Digital mass flow meters Omega FMA 1700/1800 series (see figure 3.4) were used to measure the mass flow rate of fuel and air. The mass flow meters have the capability to work with temperatures ranging from 0^0C to 50^0C, pressures of up to 500 psig, a relative humidity of 70%, These flow meters have an accuracy of ±1.5% of the full scale. The mass flow meters used in the present study are 0-5L/min, 0-30 L/min and 0-500L/min. Prior to each experiment the flow meters were set to the desired flow rate by using air.

3.2.2 Proportional control valves: The function of proportional valves is to provide a smooth and variation in flow in response to an electrical input and it is very important to link the electronics to the valve very carefully. Generally proportional control valves work in open loops situations where pressure and flow are required to change continuously. The way a proportional valve works is a balance established between the forces in action on the plunger that includes a mechanical force provided by a spring. The magnetic force is created by the current level passing

through the coil. The spring force is opposed by the magnetic force proportionally. The spring will compress until the force of the spring is equal to the armature force which is a stable position. The armature force increases as the current increases resulting in an imbalance force on the spring, which compresses the spring until a balance is re-established. Proportional valves react proportionally to the voltage supplied. Jefferson valve 1314 series was used for the current study. Since for this present study, a very low flow rate was used, manual precision metering valves SS-SS4VH were used to control the desired flow of fuel and air flow rates.

3.2.3 Solenoid valve: Solenoid valve consists of nine essential elements as shown in Fig 3.4. Gases controlled by the solenoid valve enter the valve through the inlet port (Part 2 in the Fig). Gases flow through the orifice (9) before continuing into the outlet port (3). The orifice is closed and opened by the use of plunger (7). Solenoid valve used in this present study is a normally-closed solenoid valves that uses a spring (8) which presses the plunger tip against the opening of the orifice. The sealing material at the tip of the plunger keeps the gas from entering the orifice, until the plunger is lifted up by an electromagnetic field created by the coil.

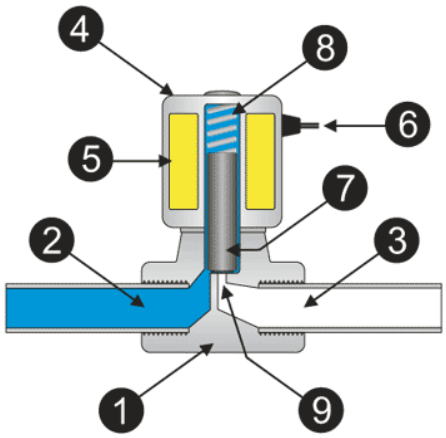

1. Valve 2. Inlet Port Body 3. Outlet Port 4. Coil / Solenoid 5. Coil Windings. 6. Lead Wires 7. Plunger 8. Spring 9. Orifice

Figure 3.10 : Different parts of solenoid valve

3.3 Instrumentation

3.3.1 Imaging technique: Particle Image Velocimetry (PIV) is an optical method of flow visualization. PIV can be applied to both non-reacting and reacting flows. In this present study PIV has been used only for cold flow characterization. In PIV, the fluid is seeded with particles and the fluid is then illuminated by the use of a laser sheet that causes the particles to scatter light to the camera. PIV analysis requires two frames to be captured in order to compare them and produce a flow field. CCD camera capture two frames at very high speeds with only a few ns between frames and post processing software calculates the displacement of the particles and the corresponding flow properties.

All the equipment used for PIV was synchronized with Dantec Dynamic's software. The system used for this study consists of a Phantom v310 camera, with a resolution of 1280 x 800 at 3250 fps and a maximum repetition rate of 500,000 fps (Figure 3.11) and a high speed Nd:YLF LDY300 series laser with a maximum firing rate of 20 kHz (Figure 3.12). A PS-10 Seeder system from SCITEK Consultants Ltd. was used to introduce the particles in the flow, see Figure 3.13. The seeder can operate with temperatures in the range of 0 to 60°C. Figure 3.14 shows a picture of the entire setup. High resolution direct imaging was used using HDR-SR 11. A remote system of flame observation was made for the safety of the operators as shown in Fig 3.15.

Figure 3.11 : Phantom v310 camera

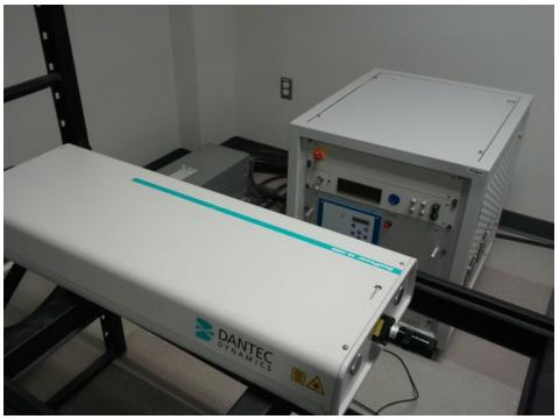

Figure 3.12 : LDY300 series high speed laser

Figure 3.13 : PS-10 Seeder system from SCITEK

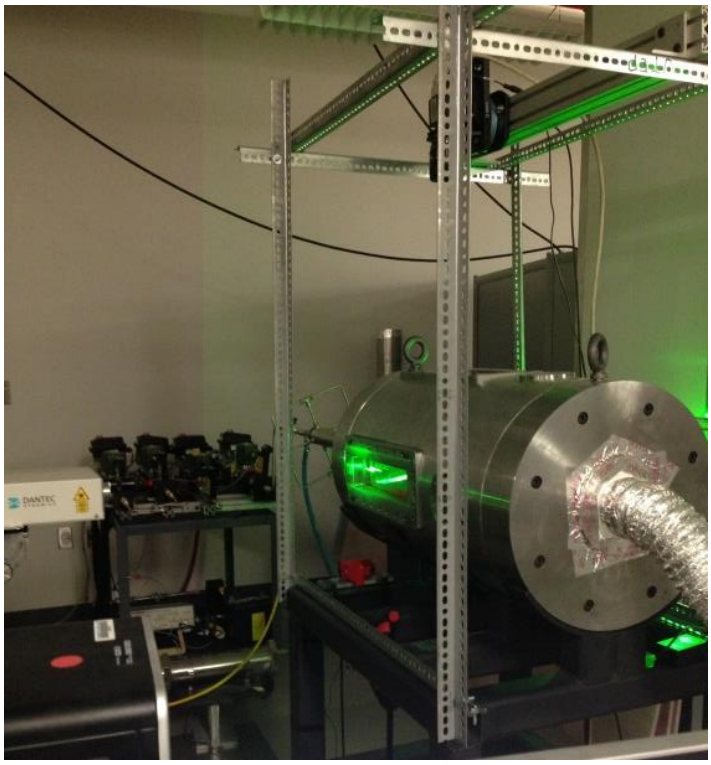

Figure 3.14 : Experimental set up for PIV

Figure 3.15 : Experimental set up for remote observation

3.4 Background Analysis: For the present study, research is focused on flame stability, specifically blowout since the designed injector mitigates problems with flame flashback. Lewis and von Elbe, (1943) defined a term critical velocity gradient at the boundary for blow-off in their study. It is described that at some point gas and burning velocities are equal, and the flame is thus attached to the orifice. Then as the flow is increased the combustion zone moves away from the rim and gains burning velocity until a new point of equality (burning velocity equals flame speed) is established farther out from the injector exit. The reason for this is that independent of the quenching action of the rim, the burning velocity diminishes toward the boundary of the stream and gradually the gas velocity exceeds the burning velocity everywhere in the stream causing the flame to blow off the tube. These authors express the critical velocity gradient at the boundary for blow-off can in Eq. (1):

$$g_B = \frac{4V}{\pi R^3} \tag{3.2}$$

Where g_B is critical velocity gradient at blow out, V is the volumetric flow rate at blowout condition and R is the radius of the tube. Wohl, 1953 also described a relationship between critical velocity gradient and blow-off distance as,

$$g_{B=\frac{S_u}{X_{bl}}} \tag{3.3}$$

Where S_u is laminar burning velocity and X_{bl} is blow-off distance and it can be rearranged as:

$$g_{B=} CS_u \tag{3.4}$$

Where C is a correlation constant (scaling constant) for different composition of syngas fuel which equals to $1/X_{bl}$. Starkey et al. (2007) used Peclet Number for modeling blowout. Putnum and Johnson, 1949 have found Pe_U to correlate with $Pe_{S_L}^2$ as,

$$Pe_U = C\, Pe_{S_L}^2 \tag{3.5}$$

Where,

$$Pe_U = \frac{U_{ref}D}{\alpha} \quad \text{and} \quad Pe_{S_L}^2 = \frac{S_L D}{\alpha} \tag{3.6}$$

Zhang et al. (2007) described that Damköhler number correlation is equivalent to Peclet number correlations as,

$$Pe_U = (1/Da)\, Pe_{S_L}^2 \tag{3.7}$$

3.5: Description of the test matrix: This study focuses on the blowout characteristics of syngas mixtures ranging from 10% to 30% hydrogen concentration in carbon monoxide (CO) emitted from a novel multi-tube injector that is incorporated in the high pressure gas turbine combustor. A systematic experimentation was performed using multi-tube injector. Three different conditions were carried out for the experimentation-1) where jet velocity is greater than

the flame speed, 2) jet velocity is equal to the flame speed and 3) jet velocity is less than the flame speed. Laminar flame speed of different compositions of syngas fuel at different equivalence ratio was calculated by CHEMKIN kinetic code, using the GRI 3.0 mechanism. All the experiments were carried out at equivalence ratios ranging from 0.8 to 1.5. It was not possible to conduct the experiment at very lean conditions because of very low flow that is not possible to acquire from flow meters that are currently installed in the system.

Chapter 4 : Computational Modeling and Results

This chapter consists of 1) a cold flow numerical simulation of the designed multi–tube injector and 2) a numerical investigation of NO_x emission of syngas fuel mixture of the same multi-tube injector. The main objective of conducting the cold flow simulation is to characterize the fluid flow behavior of the injector. The main objective of the task is to evaluate the NO_x emission characteristics of the designed injector. Models used for flow of syngas fuel and combustion are the k-ε model for turbulent flows, mixture fractions/PDF model for partially premixed gas combustion, and P-1 radiation model respectively. A NO_x modeling section was also done

4.1 Problem Description: A multi-tube injector has been integrated into the high pressure combustor. This multi-tube injector consists of 13 ports where each orifice has a diameter and length of 4 and 24 mm; respectively. This injector is attached to the combustor through the front cap. A detailed design is discussed in Chapter 3. A full three-dimensional model of flow of fully premixed air and syngas fuel was simulated and has been modeled at equivalence ratios of 0.5, 0.75 and 1. A schematic of the fluid domain is depicted in Fig 4.1 and Table 4.1 shows the solution method used in the simulation.

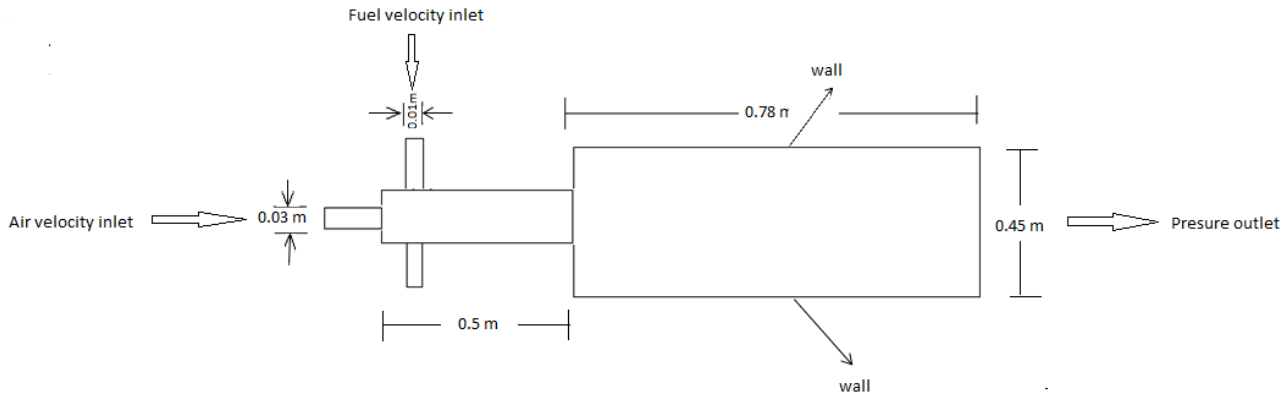

Figure 4.1 : Schematic of fluid domain

Table 4.1: Solution Method

Spatial Discretization	**Method**
Momentum	Second order upwind
Turbulent kinetic energy	First order upwind
Turbulent dissipation rate	First order upwind
Pollutant no	Second order upwind
Temperature variance	Second order upwind
Progress variable	Second order upwind
Mean mixture fraction	Second order upwind
Mixture fraction variance	Second order upwind

Table 4.2 : Models used in the simulation

Model	Description	
Combustion model	Partially premix combustion	
Turbulence model	k-epsilon	
	Specification method	Intensity and hydraulic diameter
	Turbulent intensity(%)	10
	Hydraulic diameter(m)	0.01 (fuel) 0.02 (air)
Progress variable (mean mixture fraction)	1 (fuel) 0 (Air)	

4.2 Grid: The grid used for cold and hot flow is a high quality, structured tetrahedral grid system that was generated using Ansys Workbench. Initially the grid was created using the automatic method and contained a total of 265,268 cells as shown in Fig 4.2. The mesh created

by this automatic method was relatively coarse and the mesh sizing was implemented in order make the mesh finer as shown in Fig 4.3. A grid independence test was carried out and it has been investigated by comparing results from different meshes. If grid independence has been reached, the solutions from different meshes should be identical that makes the researcher confident that a finer mesh would not improve the solution. Figure 4.2 represents the grid independence test.

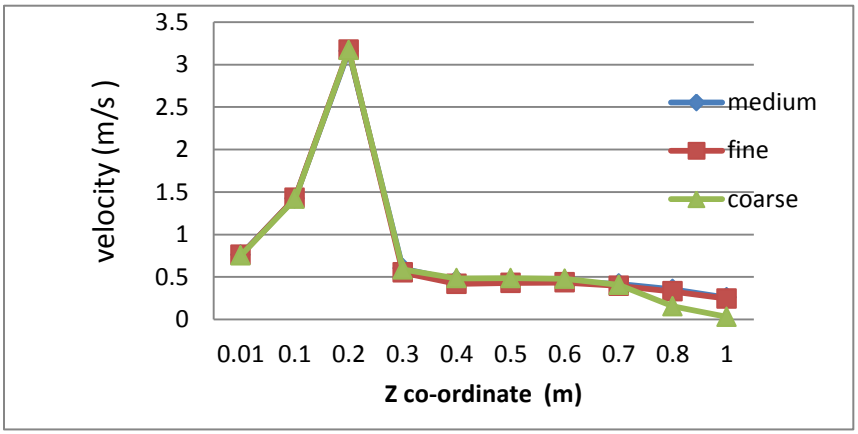

Figure 4.2 : Grid independence test

Medium and fine mesh shows the identical result. Finally medium grid was used in order to save computational time that contained 315,543 tetrahedral cells. In a fluid domain near the wall the velocity decreases non-linearly up to a point where the fluid will have zero velocity at the wall. This no-slip condition was imposed here. In a typical velocity profile in the near-wall region, there is a large change in velocity normal to the wall and it is very important for to capture this gradient correctly. An inflation layer meshing is required to accurately capture the boundary layer region for any wall-bounded turbulent flows. In order to obtain a more accurate result, an inflation layer was introduced into the fluid domain as shown in Fig 4.4.

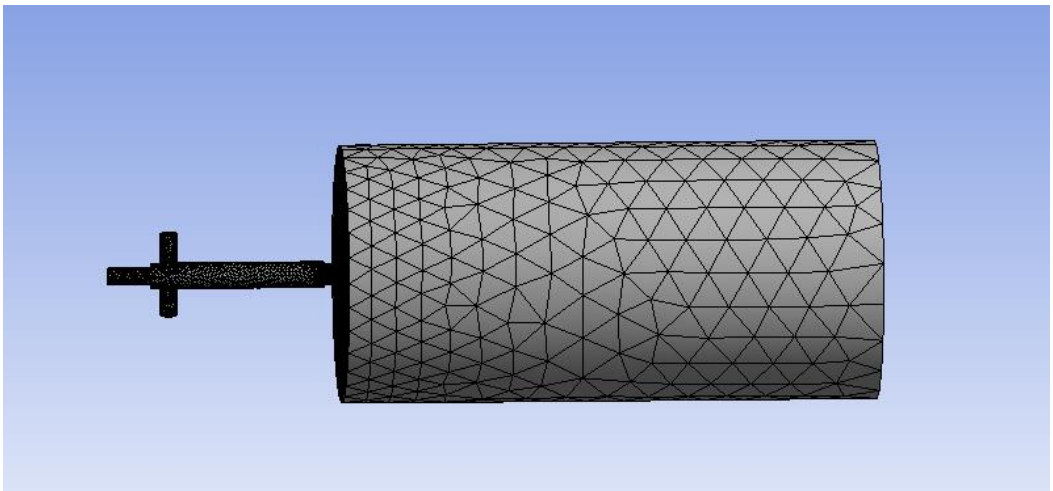

Figure 4.3 : Coarse mesh generated by automatic method

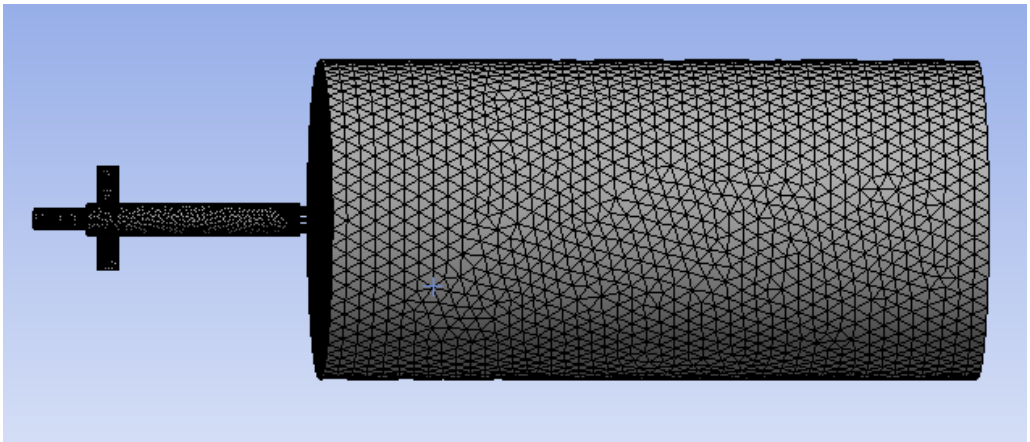

Figure 4.4: Medium mesh generated by mesh sizing using tetrahedron method

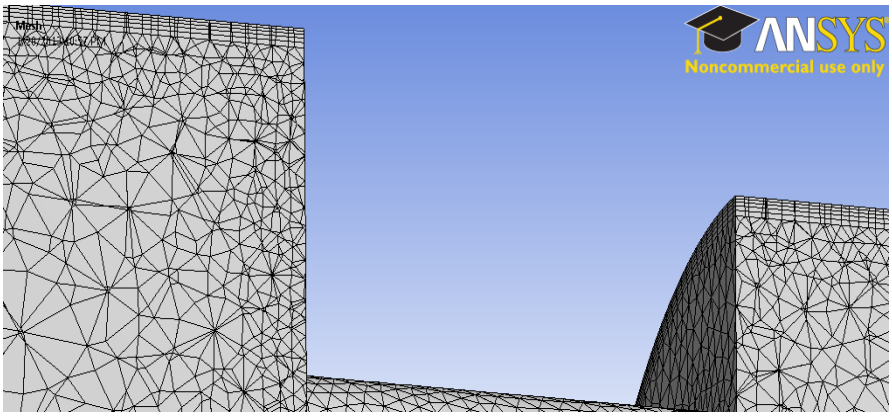

Figure 4.5 : Close up view of the inflation layer

4.3 Governing equations

4.3.1 Flow equations

Equations that govern the flow of the chemically reacting gas mixture consists of the mass, momentum, and energy conservation laws and equations that describe the conservation of chemical species, thermodynamic properties; and reaction rates [Norbert, 2000; Swaminathan et al., 2011].

Continuity

$$\frac{\partial \rho}{\partial t} + \frac{\partial (\rho u_k)}{\partial x_k} = 0 \tag{4.1}$$

Momentum

$$\frac{\partial \rho u_l}{\partial t} + \frac{\partial \rho u_k u_l}{\partial x_k} = -\frac{\partial p}{\partial x_l} + \frac{\partial \tau_{lk}}{\partial x_k} + \rho \sum_{i=1}^{N} Y_i f_{il} \tag{4.2}$$

Here τ_{lk} is the viscous stress tensor

$$\tau_{lk} = \mu \left(\frac{\partial u_l}{\partial x_k} + \frac{\partial u_k}{\partial x_l} - \frac{2}{3} \frac{\partial u_m}{\partial x_m} \delta_{lk} \right) \tag{4.3}$$

Species conservation

$$\rho \frac{\partial Y_i}{\partial t} + \rho u_k \frac{\partial Y_i}{\partial x_k} = -\frac{\partial J_{ik}}{\partial x_k} + \dot{w}_i \quad (4.4)$$

The symbols x_k, u_k, ρ, p, Y_i,, J_{ik}, f_{il} and $\dot{w}_i$ represent the coordinate direction k, velocity component in k, density, pressure, mass fraction of species i, the molecular diffusion flux of species i in direction k, body forces acting on species i in the direction l and the rate of production or destruction of species i due to reactions. The molecular diffusion flux J_{ik} can be expressed by,

$$\boldsymbol{J_{ik} = -\rho D_i \frac{\partial Y_i}{\partial x_k}} \quad (4.5)$$

Where D_i is diffusion coefficient.

Energy equation

From the equation of state we get

$$\boldsymbol{p = \rho R T \sum_{i=1}^{N} \frac{Y_i}{W_i}} \quad (4.6)$$

Here R is universal gas constant and W_i is the molecular weight of species i.

Enthalpy can be calculated by

$$\boldsymbol{h = \sum_{i=1}^{N} Y_i h_i} \quad (4.7)$$

Where

$$\boldsymbol{h_i = h_i^0 + \int_{T^0}^{T} c_{p,i} dT} \quad (4.8)$$

Here h_i^0 is the standard specific heat of formation of species i at temperature T^0.

The energy equation in terms of entropy

$$\rho \frac{\partial h}{\partial t} + \rho u_k \frac{\partial h}{\partial x_k} = \frac{\partial p}{\partial t} + u_k \frac{\partial p}{\partial x_k} + \tau_{lk} \frac{\partial u_l}{\partial u_k} - \frac{\partial q_k}{\partial x_k} - \rho \sum_{i=1}^{N} h_i f_{ik} \frac{\partial Y_i}{\partial x_k} + q_{rad} \quad (4.9)$$

Here q_k is the heat flux that can be expressed by:

$$q_k = -\lambda \frac{\partial T}{\partial x_k} - \rho \sum_{i=1}^{N} h_i D_i \frac{\partial Y_i}{\partial x_k} \quad (4.10)$$

Where λ is the thermal conductivity.

4.3.2 Chemical reaction rate

The rate of production of species *i* ($\dot{w}_i$) that has been used in eq (5.4) can be expressed by

$$\dot{w}_i = W_i \sum_{i=1}^{N} (v''_{ik} - v'_{ik}) \bar{w}_k \quad (4.11)$$

Here v'_{ir} and v''_{ir} are the stoichiometric coefficients of species *i* in reaction *r* in the forward and backwards direction accordingly that can be derived from a reaction mechanism in the form

$$\sum_{i=1}^{N} v'_{ki} M_i \quad \frac{k_{fk}}{k_{bk}} \quad \sum_{i=1}^{N} v''_{ki} M_i \quad (4.12)$$

The term $\bar{w}_k$ in equation (4.11) represents the rate of reaction r and it can be calculated from:

$$\bar{w}_k = k_{fk} \prod_{j=1}^{N} \left(\frac{\rho Y_j}{W_j}\right)^{v'_{jr}} - k_{bk} \prod_{j=1}^{N} \left(\frac{\rho Y_j}{W_j}\right)^{v''_{jr}} \quad (4.13)$$

Here k_{fk} and k_{bk} are the forward and backward reaction rate coefficients of reaction *k*, and can be expressed by

$$k_{fk} = A_{fk} T^{\alpha_{fk}} e^{\left(\frac{-E^a_{fk}}{RT}\right)} \quad (4.14)$$

$$k_{bk} = A_{bk} T^{\alpha_{bk}} e^{\left(\frac{-E_{bk}^{a}}{RT}\right)} \tag{4.15}$$

Where A_{fk}, A_{bk}, α_{fk}, α_{bk}, E_{fk}^{a}, and E_{bk}^{a} are constants of the empirical nature contained in the reaction mechanism rates [Norbert, 2000; Swaminathan et al., 2011].

4.2 Modeling Techniques

A turbulence model for the Reynolds Stresses and a combustion model for the reaction rate are needed in order to convert the governing equations into a closed set.

4.2.1 Modeling Turbulent Flow

Though in theory, governing equations of fluid flow (Navier-Stokes equations) are perfectly deterministic can be solved numerically but in reality velocity behaves in such a chaotic manner that the computing power that is available today is not enough to solve for typical domain sizes and flow speeds [Davidson et al.,2004 ; Pope, 2000]. Because of the term that is used to describe this behavior is the non-linearity term in the momentum equation (convection of momentum), most turbulence theories focus on the determination of the statistical properties of the flow and not on the velocity [Durbin et al., 2011].

Reynolds Averaged Navier Stokes Equations (RANS)

This approach involves the decomposition of the velocity term into its mean and the fluctuating term [Pope, 2000]

$$u(x,t) = \bar{u}(x) + u'(x,t) \tag{4.16}$$

By substituting this decomposition into the governing equations, and taking the time average we have

$$\frac{\partial(\bar{u}_k)}{\partial x_k} = 0 \tag{4.17}$$

$$\frac{\partial \rho \bar{u}_k \bar{u}_l}{\partial x_k} = -\frac{\partial \bar{p}}{\partial x_l} + \frac{\partial}{\partial x_k}\left[\bar{\tau}_{lk} - \rho\overline{u_k' u_l'}\right] \quad (4.18)$$

The k-epsilon turbulence model has been used for reacting flow simulation; Large Eddy Simulation has been used for cold flow simulation.

k- epsilon turbulence model

At high Reynolds numbers the rate of dissipation of kinetic energy ϵ is equal to the viscosity multiplied by the fluctuating vortices. The k - epsilon model consists of the turbulent kinetic energy equation and the dissipation rate equation.

$$\frac{\partial k}{\partial t} + div\,(\rho\mu k) = div([\,\mu_{lam} + \frac{\rho\vartheta_t}{\sigma_k}\,]\,\text{grad}\,k\,) + \rho\vartheta_t G - \rho\epsilon \quad (4.19)$$

$$\frac{\partial \epsilon}{\partial t} + div\,(\rho\mu k) = div([\,\mu_{lam} + \frac{\rho\vartheta_t}{\sigma_k}\,]\,\text{grad}\,\epsilon\,) + C_1\rho\,\vartheta_t G\,\frac{\epsilon}{k} - C_{2\epsilon}\rho\,\frac{\epsilon^2}{k} \quad (4.20)$$

Where *G* represents the turbulent generation rate which is equal to

$$G = 2([\,\frac{\partial u}{\partial x}]^2 + [\,\frac{\partial v}{\partial y}]^2 + \left[\,\frac{\partial w}{\partial z}]^2\right) + (\,\frac{\partial u}{\partial y} + \frac{\partial v}{\partial x})^2 + (\,\frac{\partial u}{\partial z} + \frac{\partial w}{\partial x})^2 + (\,\frac{\partial w}{\partial y} + \frac{\partial v}{\partial z})^2 \quad (4.21)$$

Large Eddy Simulation (LES)

In LES, the large scales of the energy spectrum are resolved and the smaller scales are averaged. The Subgrid Scale (SGS) model [Tabor et al., 2004] is used to model their effect. Compared to the Reynolds Averaged Navier-Stokes (RANS) models, LES provides more detailed information of flow fields and reaction zones that is not possible to get with traditional RANS. A filtering operator as shown in Eq. (4.22) is used to get governing equations for LES. The resulting incompressible governing equations for LES are shown in Eqns (4.22-4.26) [Pope et al.,2000].

$$\bar{\emptyset}(\boldsymbol{x}) = \int_{\boldsymbol{D}} \emptyset(\boldsymbol{x}')\boldsymbol{G}(\boldsymbol{x},\boldsymbol{x}')\boldsymbol{dx}' \quad (4.22)$$

$$\frac{\partial \rho}{\partial t} + \frac{\partial}{\partial x_i}(\rho \bar{u}_i) = 0 \tag{4.23}$$

$$\frac{\partial}{\partial t}(\rho \bar{u}_i) + \frac{\partial}{\partial x_j}(\rho \bar{u}_i \bar{u}_j) = \frac{\partial}{\partial x_j}(\sigma_{ij}) - \frac{\partial \bar{p}}{\partial x_i} - \frac{\partial \tau_{ij}}{\partial x_j} \tag{4.24}$$

Where

$$\sigma_{ij} \equiv \left[\mu\left(\frac{\partial \bar{u}_i}{\partial x_j} + \frac{\partial \bar{u}_j}{\partial x_i}\right)\right] - \frac{2}{3}\mu \frac{\partial \bar{u}_k}{\partial x_k}\delta_{ij} \tag{4.25}$$

And

$$\tau_{ij} \equiv \rho\overline{u_i u_j} - \rho \bar{u}_i \bar{u}_j \tag{4.26}$$

Where (¯) in the LES equations stands for a filtered quantity

4.2.2 Modeling reacting flow

Partially premixed modeling: Since premixed combustion model is not compatible with pollutant (i.e., soot, NO_X) calculations in Fluent. Instead this study will assume a perfectly premixed system which can be modeled with the partially premixed model. Partially premixed fames include premixed jets that discharge into a quiescent atmosphere, lean premixed combustors with diffusion pilot flames and/or cooling air jets. The partially premixed model in Fluent consists of the non-premixed model and the premixed model.

Non-premixed combustion model: In the non-premixed combustion model, fuel and oxidizer enter the reaction zone in two different streams. The PDF/mixture fraction model is used in this model. Instead of using individual species transport equations, equation for the conserved scalar (f*)* is solved. The predicted mixture fraction distribution is used to derive individual component concentrations and the mixture fraction equation is given by

$$f = \frac{Z_K - Z_{K,O}}{Z_{K,F} - Z_{K,O}} \quad (4.27)$$

Where Z_k is the element mass fraction of some element *k*. Subscripts *F* and *O* defines fuel and oxidizer inlet stream values, respectively. The equilibrium chemistry PDF model is used for the mixture fraction approach, the equilibrium system consists of 13 species (C, CH_4, CO, CO_2, H, H_2, H_2O, N_2, NO, O, O_2, OH, HO_2) where the chemistry is assumed to be fast enough to achieve equilibrium [Ghaouki, 2010].

Premixed combustion model:

According to Zimont et al. (2000) turbulent premixed combustion model involves the solution of a transport equation for the reaction progress variable and the closure of this equation is based on the definition of the turbulent flame speed. When flame front moves, combustion of unburnt reactants occurs that converts unburnt premixed reactants to burnt products. In the premixed combustion model, the reacting flow field is divided into regions of burnt and unburnt species that is separated by the flame sheet. The progression of the reaction is the same as the progression of the flame front where flame front propagation is modeled by solving a transport equation for the scalar quantity *c*, called Favre averaged reaction progress variable.

$$\frac{\partial}{\partial t}(\rho c) + \nabla.(\rho \vec{\vartheta}\, c) = \nabla.\left(\frac{\mu_t}{Sc_t}\nabla c\right) + \rho S_C \quad (4.28)$$

Where

c = mean reaction progress variable

S_{ct} = turbulent Schmidt number

S_c = reaction progress source term (s^{-1})

The progress variable is defined as a normalized sum of the product species,

$$c = \frac{\sum_{i=1}^{n} Y_i}{\sum_{i=1}^{n} Y_{i,eq}} \quad (4.29)$$

Where

n = number of products

Y_i = mass fraction of product species i

$Y_{i,eq}$ = equilibrium mass fraction of product species i

4.2.3 Equation for the P-1 Radiation Model—Radiation Flux Equation: In order to simulate the radiation from the flame, the P-1 radiation model is used in this study and this radiation model is based on the expansion of the radiation intensity into an orthogonal series of spherical harmonics. The P-1 radiation model is the simplest case of the P-N model. If only four terms in the series are used, the following equation is obtained for the radiation flux:

$$q_r = \frac{1}{3\,(a+\sigma_S)-C\sigma_S}\,\nabla G \quad (4.30)$$

Where a is the absorption coefficient, σ_S is the scattering coefficient, G is the incident radiation, and C is the linear-anisotropic phase function coefficient [Ghauki, 2010].

4.2.4 NOx modeling

The Fluent code allows modeling of thermal, prompt, and fueling NO_x formation as well as NO_x consumption due to reburning in combustion systems. Fluent solves a transport equation for nitric oxide (NO) concentration in order to predict NO_x emission. With fuel NO_x sources Fluent solves an additional transport equation for an intermediate species (HCN or NH_3). The NO_x transport equations are solved based on a given flow field and combustion solution that is basically a post processing from a combustion simulation. This is why an accurate combustion solution is a prerequisite of NO_x prediction.

The formation of NO_x in flames

The formation of NO_x is attributed to four distinct chemical kinetic processes: 1) thermal NO_x formation, 2) prompt NO_x formation, 3) fuel NO_x formation, and 4) reburning. Thermal NO_x is generated by the oxidation of atmospheric nitrogen present in the combustion air. Prompt NO_x is formed by high-speed reactions at the flame front, and fuel NO_x is produced by oxidation of nitrogen that is contained in the fuel. The reburning mechanism reduces the total NO_x formation that accounts the reaction of NO with hydrocarbons. Fluent NO_x model is able to simulate all these processes.

Governing equations for NO_x transport

Fluent solves the mass transport equation for the NO species that accounts for convection, diffusion, production and consumption of NO and related species. The effect of residence time in NO_x mechanisms is a Lagrangian reference frame concept that is included through theconvection terms in the governing equation, written in the Eulerian reference frame. Only the NO species transport equation is needed for thermal and prompt NO_x mechanisms:

$$\frac{\partial}{\partial t}\left(\rho Y_{NO}\right) + \nabla.\left(\rho\vec{\vartheta}\, Y_{NO}\right) = \nabla.\left(\rho D \nabla Y_{NO}\right) + S_{NO} \qquad (4.31)$$

$$\frac{\partial}{\partial t}\left(\rho Y_{HCN}\right) + \nabla.\left(\rho\vec{\vartheta}\, Y_{HCN}\right) = \nabla.\left(\rho D \nabla Y_{HCN}\right) + S_{HCN} \qquad (4.32)$$

Fluent solves a transport equation for the HCN or NH_3 species in addition to the NO species:

$$\frac{\partial}{\partial t}\left(\rho Y_{NH_3}\right) + \nabla.\left(\rho\vec{\vartheta}\, Y_{NH_3}\right) = \nabla.\left(\rho D \nabla Y_{NH_3}\right) + S_{NH_3} \qquad (4.33)$$

Where Y_{HCN}, Y_{NH3}, and Y_{NO} are mass fractions of HCN, NH_3, and NO in the gas phase. The source terms S_{HCN}, S_{NH3}, and S_{NO} are to be determined next for different NO_x mechanisms [Fluent Inc, 2001]

Since flame temperature is influential for thermal NO_x and Prompt NO can be formed in a significant quantity in some combustion environments, such as in low-temperature, fuel-rich conditions and where residence times are short [Brane,1988]. That's why thermal NO_x and prompt NO_x were encountered for NO_x modeling.

Thermal NOx formation

A set of highly temperature dependent chemical reactions known as the extended Zeldovich mechanism determine the formation of thermal NO_x. The principal reactions that govern the formation of thermal NO_x from molecular nitrogen are as follows:

$$O + N_2 \overset{K_{+1}}{\longleftrightarrow} N + NO \tag{4.34}$$

$$N + O_2 \overset{K_{+1}}{\longleftrightarrow} O + NO \tag{4.35}$$

At near stoichiometric conditions and in fuel-rich mixtures, a third reaction has been shown to contribute.

$$N + OH \overset{K_{+3}}{\longleftrightarrow} H + NO \tag{4.36}$$

Thermal NOx reaction rates

The rate constants for these reactions have been measured in numerous experimental studies [Blauven et al., 1977; Flower et al., 1975; Monat et al., 1979] and the data obtained from these

studies have been critically evaluated by Baulch et al. (1973) and Hanso et al. (1984).The expressions for the rate coefficients for reactions 4.37 to 4.42 that used in the NO_x model are given below. These were selected based on the evaluation of Hanson et al. (1984)

Where,

$$k_1 = 1.8 \times 10^8 \qquad \text{m}^3\text{/ gmol-s} \qquad (4.37)$$

$$k_{-1} = 3.8 \times 10^7 \, e^{-425/T} \qquad \text{m}^3\text{/ gmol-s} \qquad (4.38)$$

$$k_2 = 1.8 \times 10^{48} \, e^{-4680/T} \qquad \text{m}^3\text{/ gmol-s} \qquad (4.39)$$

$$k_{-2} = 3.8 \times 10^3 \, e^{-20820/T} \qquad \text{m}^3\text{/ gmol-s} \qquad (4.40)$$

$$k_3 = 7.1 \times 10^7 \, e^{-450/T} \qquad \text{m}^3\text{/ gmol-s} \qquad (4.41)$$

$$k_{-3} = 1.7 \times 10^8 \, e^{-24560/T} \qquad \text{m}^3\text{/ gmol-s} \qquad (4.42)$$

Where k_1, k_2, and k_3 are the rate constants for the forward reactions respectively, and k_{-1}, k_{-2}, and k_{-3} are the corresponding reverse rates. The net rate of formation of NO via reactions from 4.37 to 4.42 is given by

$$\frac{d[NO]}{dt} = k_1[O][N_2] + k_2[N][O_2] + k_3[N][OH] - k_{-1}[NO][N] - k_{-2}[NO][O] - k_{-3}[ONO][H] \qquad (4.43)$$

Where all concentrations have units of gmol/m^3.

Prompt NO_x formation

The presence of a second mechanism leading to NO_x formation was first identified by Fenimore and was termed prompt NO_x. At present the prompt NO_x contribution to total NO_x from stationary combustors is small. However, as NO_x emissions are reduced to very low levels by employing new strategies (burner design or furnace geometry modification), the relative

importance of the prompt NOx can be expected to increase. The actual formation involves a complex series of reactions and many possible intermediate species.

$$CH + N_2 \leftrightarrow HCN + N \quad (4.44)$$

$$N + O_2 \leftrightarrow NO + O \quad (4.45)$$

$$HCN + OH \leftrightarrow CN + H_2O \quad (4.46)$$

4.3: Results:

4.3.1 Cold flow simulation: A cold flow simulation was done to evaluate the flow behavior of the injector. At first a cold flow simulation was first done for a swirl stabilized flow. Velocity contours as shown in Fig 4.6 represent the typical swirl stabilized flow. The vector field of Fig 4.7 shows two strong recirculation zones at the downstream of the swiler. Figure 4.9 represents the velocity distribution along the x- coordinate with the bulk velocity of 3.3 m/s used for the simulation that replicates the previous work done by Corona, 2010 experimentally.

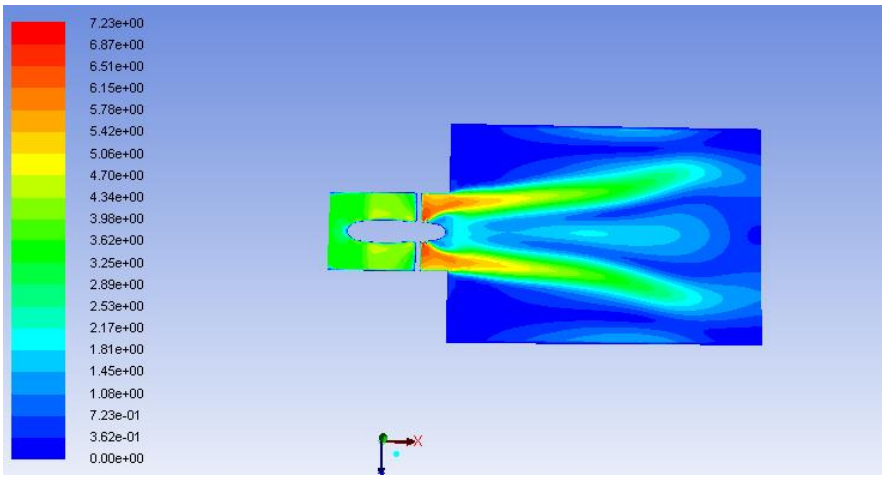

Figure 4.6 : Velocity contour at an inlet velocity of 3.3 m/s (non-reacting flow)

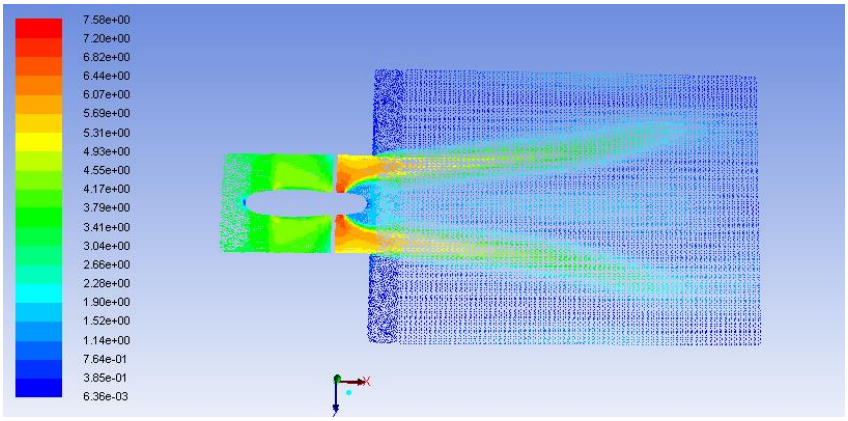

Figure 4.7 : Velocity vectors at an inlet velocity of 3.3 m/s (non-reacting flow)

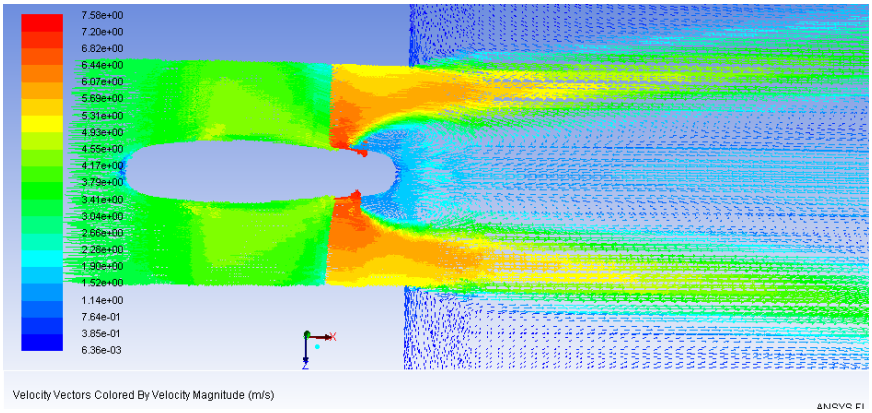

Figure 4.8: velocity vectors at the downstream of the swirler at an inlet velocity of 3.3 m/s (non-reacting flow)

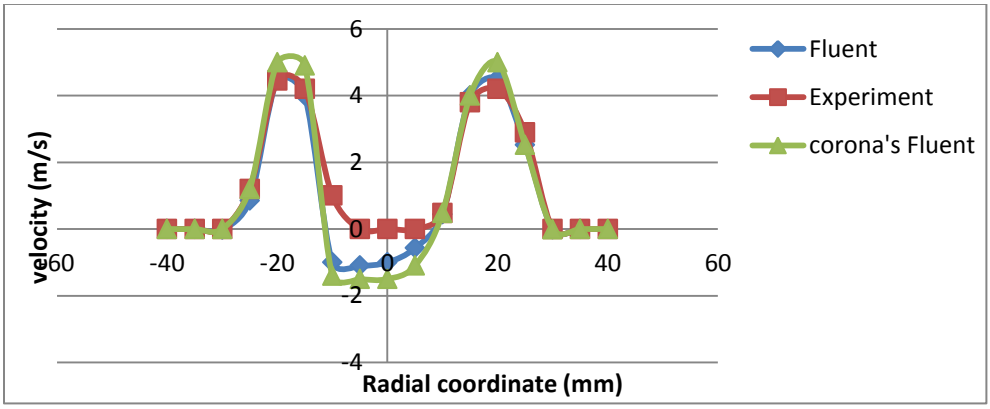

Figure 4.9 : Velocity distribution along Radial coordinate

Then a cold flow simulation was carried out for the multi-tube injector using a LES solver. Figure 4.10 shows the velocity contours. Figure 4.11 represents the typical jet out of the multi-tube injector. Since the area right after the injector is the point of interest, a close observation was made at that location.

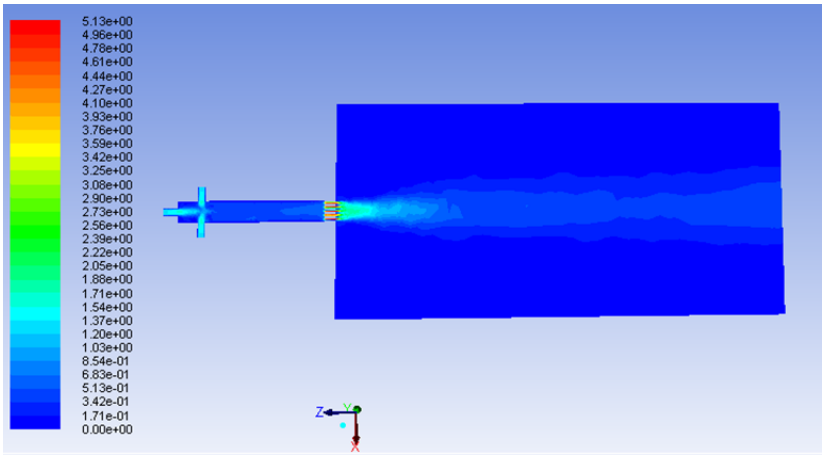

Figure 4.10 : Velocity contours for the multi-tube injector

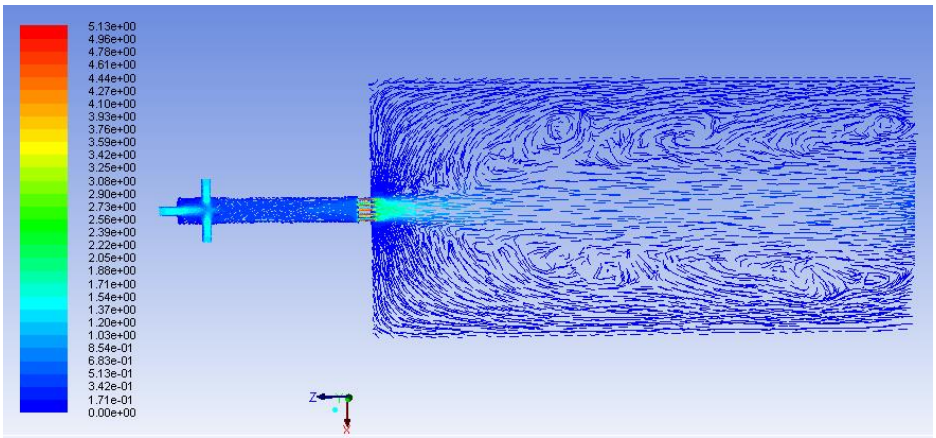

Figure 4.11 : Velocity vectors for the multi-tube injector

Figures 4.12 and Fig 4.13 show the velocity contours at a distance of 50 mm from the injector face representing the fluid mixing. Results show strong interactions between the orifices that are distant by 7 mm and show a weak interaction between the orifices that are distant by 10 mm. From Fig 4.12 - 4.15, the diffusive fashion of the flow ejecting from injector can be seen.

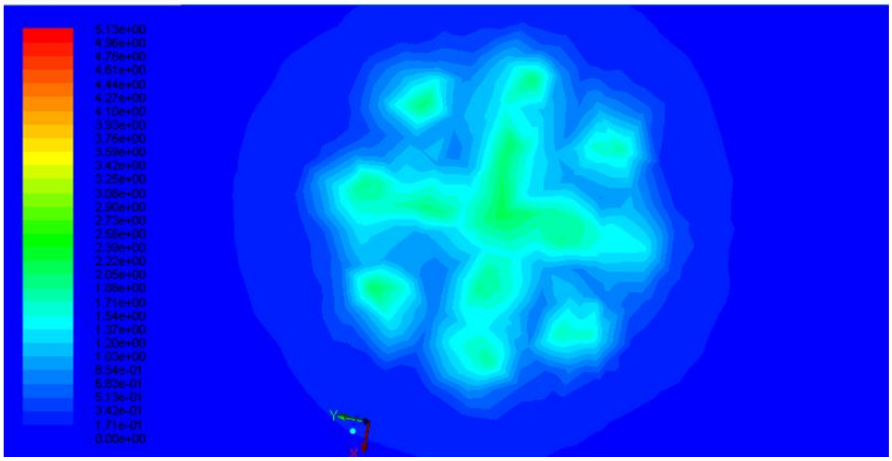

Figure 4.12 : Velocity contour at an axial distance of Z= 50 mm

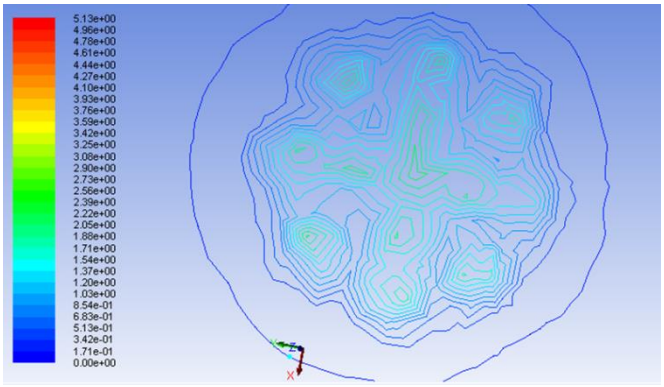

Figure 4.13: Unfilled Velocity contour at an axial distance of Z= 50 mm

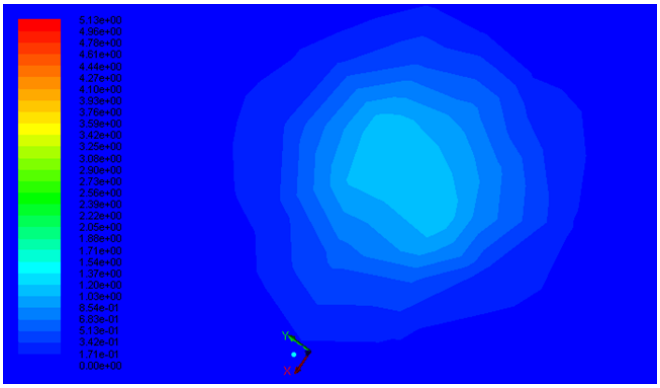

Figure 4.14 : Velocity contour at an axial distance of Z= 200 mm

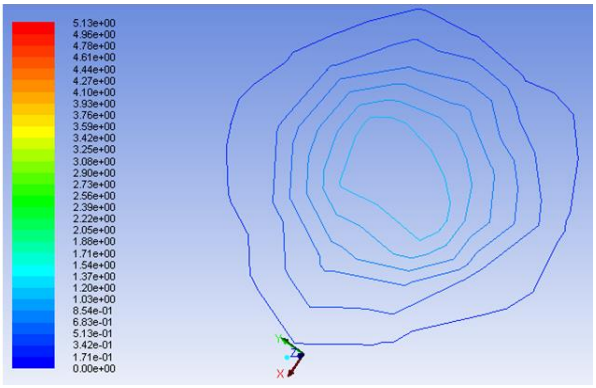

Figure 4.15: Unfilled Velocity contour at an axial distance Z= 200 mm

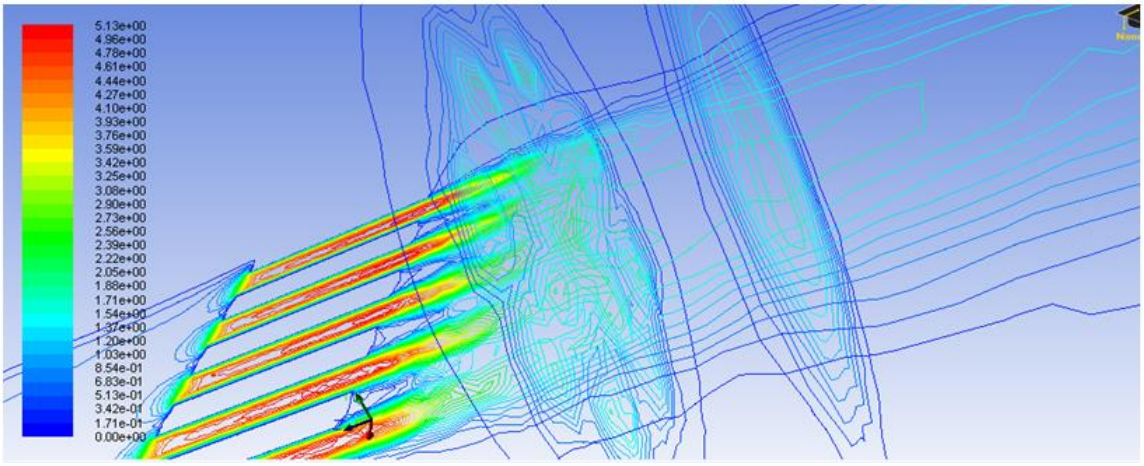

Figure 4.16 : Velocity contours plotted in the center plane at Z= 50 and Z= 200mm

Figures 4.16 and 4.17 show that the flow is coming out as a jet from each port and after an axial distance of 50 mm from injector face, jets are interacting with each other. This result indicates higher velocities near the injector face.

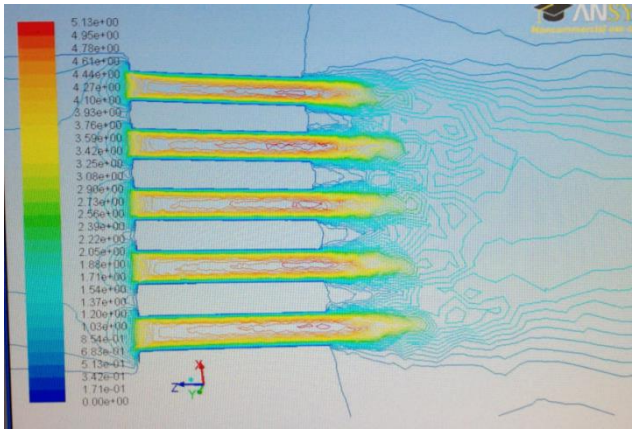

Figure 4.17 : Velocity contours exiting the injector

4.3.2 Reacting flow: Simulation of reacting flow was carried out at equivalence ratio of 0.5, 0.75 and 1. At first a simulation was carried out using a syngas –air combustion for swirl stabilized flow. Figure 4.18 shows the temperature contours of syngas-air combustion for an equivalence ratio 0.8 which shows that the model predicts temperature in the chamber within the acceptable limits.

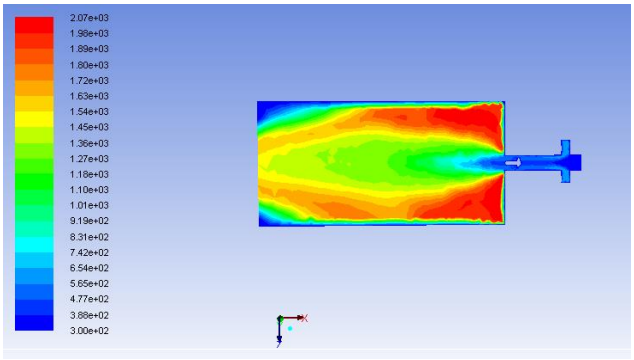

Figure 4.18 : Temperature contours of syngas combustion for a swirl stabilized flame

Then syngas-air combustion was simulated for the multi-tube injector. The temperature profile as shown in Fig 4.19 represents that the flame is way lifted from the injector face where inlet velocity of 40m/s was used. In order to evaluate the bulk velocity effect, another analysis was carried out using lower bulk velocity of 10 m/s; with an equivalence ratio of 0.65 maintained for both cases. Figure 4.18 shows that the flame is anchored at a distance of 35 mm off from the injector face which indicates the lifted flame. Results show bulk velocity to be very influential on the flame anchoring of the multi-tube injector.

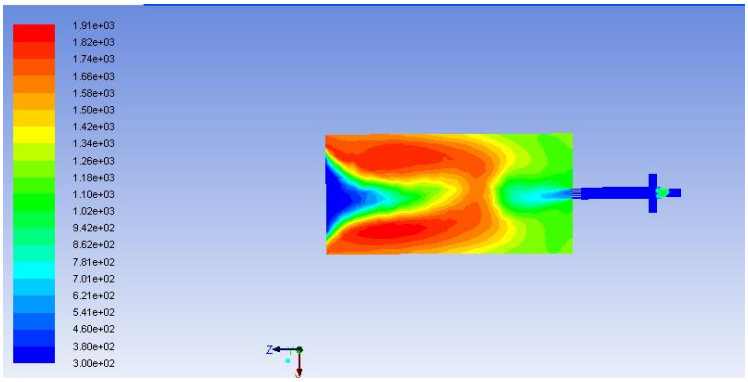

Figure 4.19 : Temperature contours of a syngas flame at inlet velocity of 40m/s

The same syngas-air flame temperatures were calculated at equivalence ratios of 0.5, 0.75 and 1 at a fixed velocity of 10 m/s. The contours of the burned gas temperature for the combustion of syngas in the gas turbine combustor are shown in Fig 4.20, 4.21 and 4.22 for equivalence ratio of 0.5, 0.75 and 1, respectively. The maximum gas temperature for syngas combustion of ratio of 0.5, 0.75 and 1 is 1800K, 2250K and 2333 K accordingly which shows that the model predicts the temperature within acceptable limits.

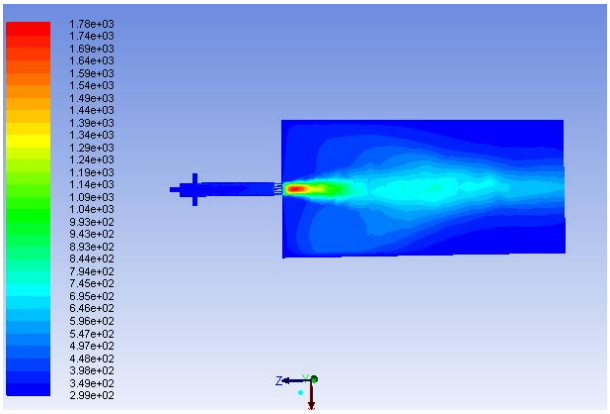

Figure 4.20: Temperature contours of syngas combustion at an equivalence ratio of 0.5

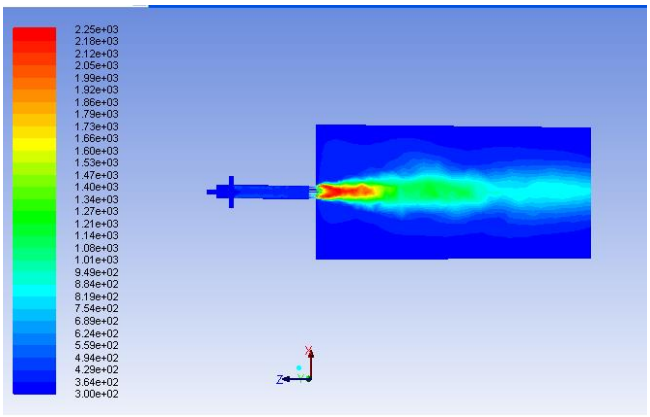

Figure 4.21 : Temperature contours of syngas combustion at an equivalence ratio of 0.75

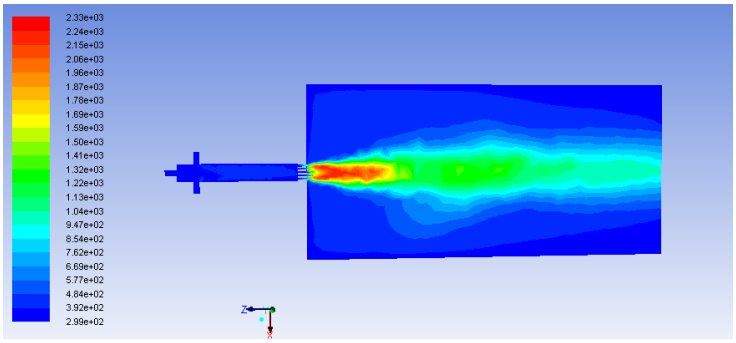

Figure 4.22 : Temperature contour of syngas combustion at an equivalence ratio of 1

Figures 4.23 to 4.25 represent the OH radical distribution for equivalence ratios of 0.5, 0.75 and 1 respectively. Location of OH radical is used here to indicate primary reaction zone. Result of

flame temperature and position of OH radical concentration reveal the expected scenario (primary reaction zone is followed by the location of OH radical).

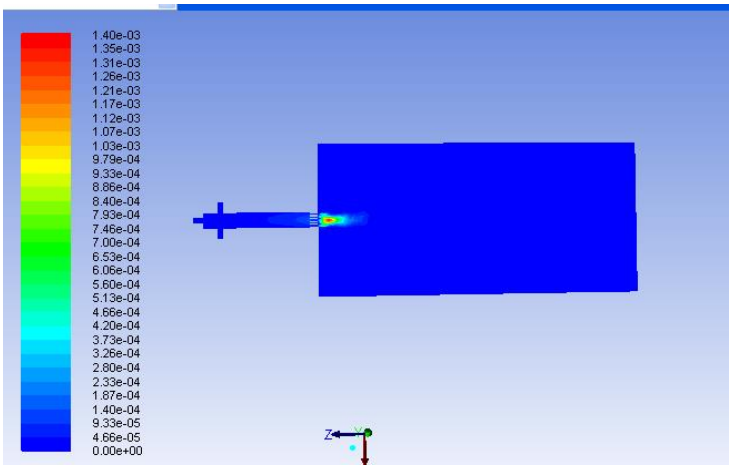

Figure 4.23: mass fraction of OH at an equivalence ratio of 0.5

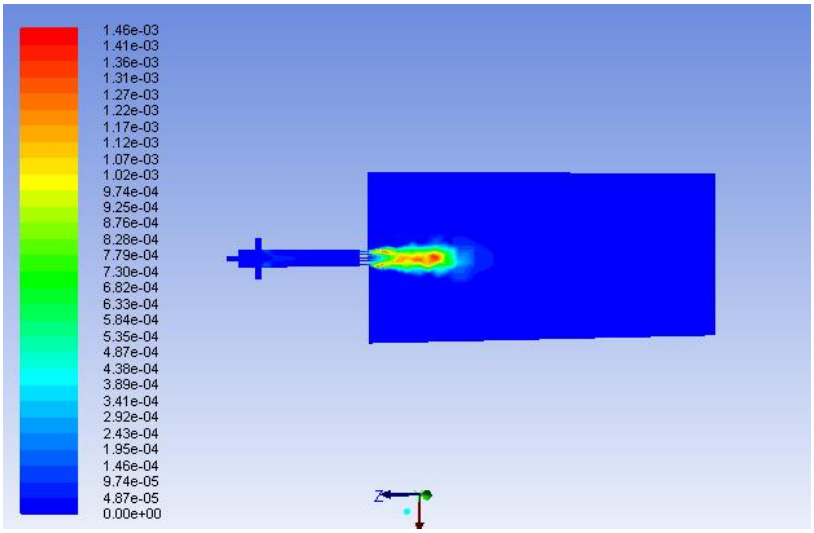

Figure 4.24: Mass fraction of OH at an equivalence ratio of 0.75

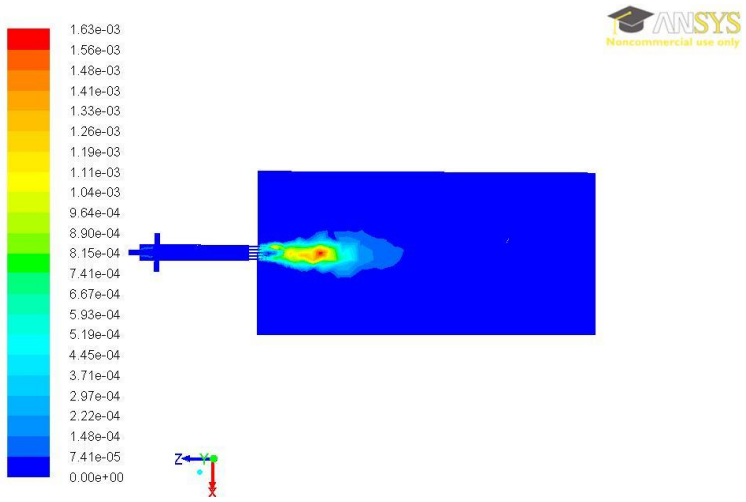

Figure 4.25 : Mass fraction of OH at an equivalence ratio of 1

In order to see the flame evolution, different planes were visualized after the injector face. Unfilled temperature contours were used to get a distinct visualization of flame progression. Figures 4.26 to 4.28 represent the flame evolution for equivalence ratios of 0.5, 0.75 and 1, respectively.

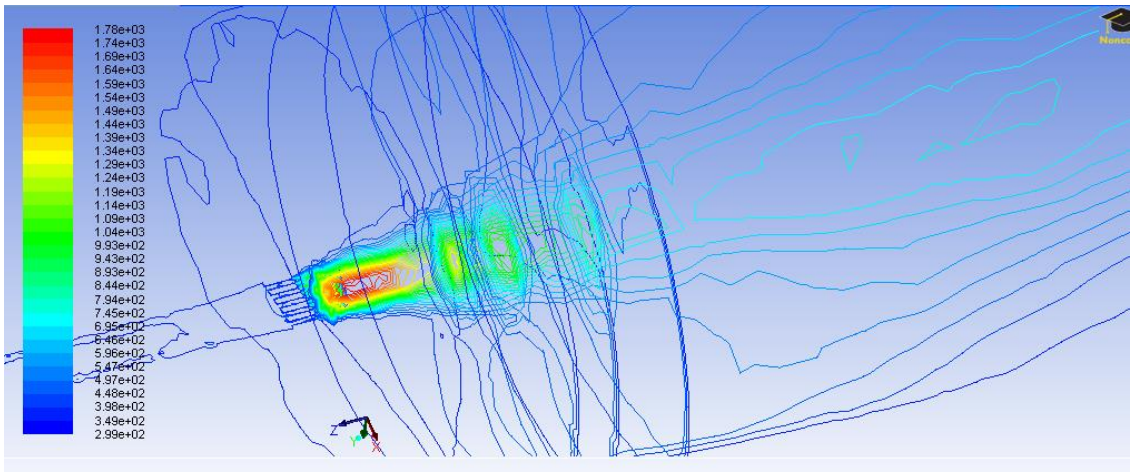

Figure 4.26 : Unfilled temperature contours at an equivalence ratio of 0.5 (Z= 50,120,150,200 mm)

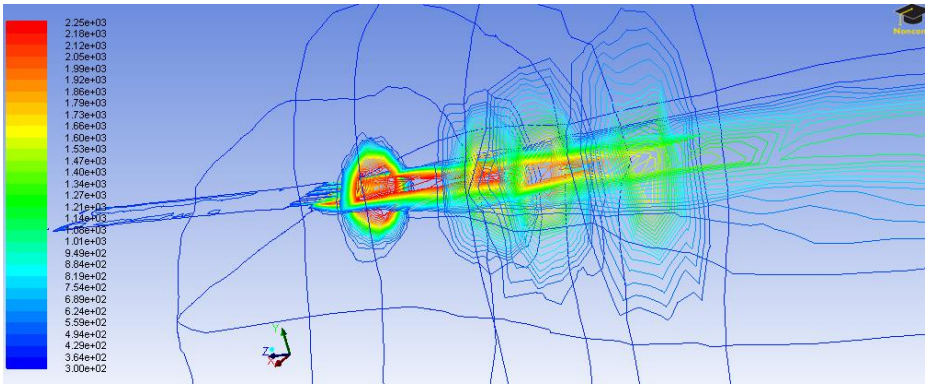

Figure 4.27 : Unfilled temperature contours at an equivalence ratio of 0.75 (Z= 50,120,150,200 mm)

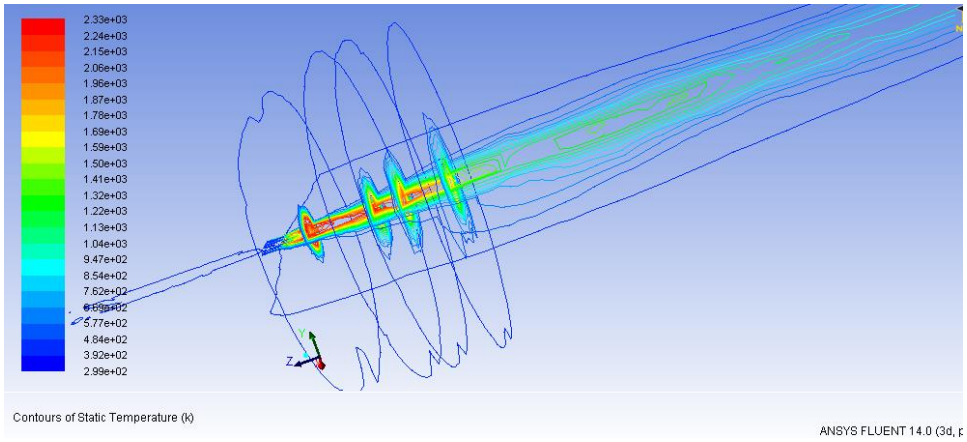

Figure 4.28: Unfilled temperature contours at an equivalence ratios of 1 (Z= 50,120,150,200 mm)

Figures 4.29 to 4.31 show the temperature contours for syngas combustion at equivalence ratios of 0.5, 0.75 and 1 respectively in the combustor at different axial positions (Z = 50 mm, 120 mm, 150 mm and 200mm).The size of the flame increases downstream and reached a maximum at Z= 120 mm. The flame attained the maximum temperature at Z = 50 mm. After that the radius and temperature of the flame decreased with the increase of the axial distance. A uniform gas temperature distribution is obtained at the exit of the combustor.

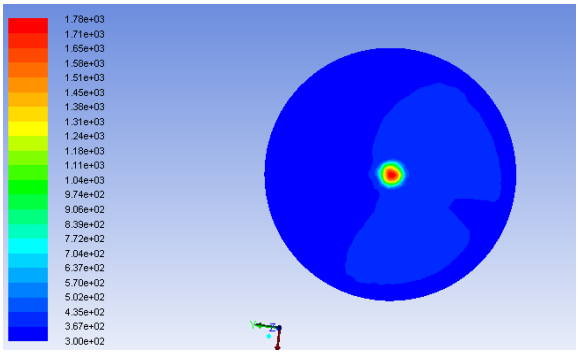

Z= 50 mm

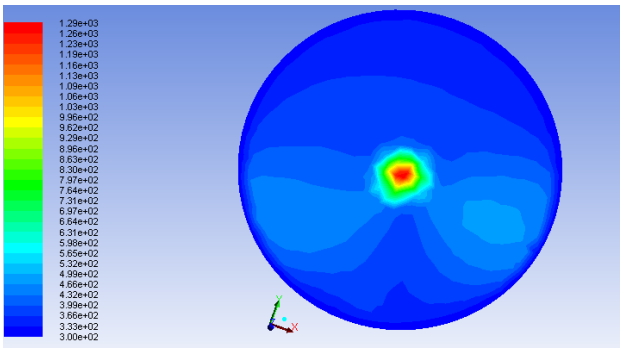

Z= 120 mm

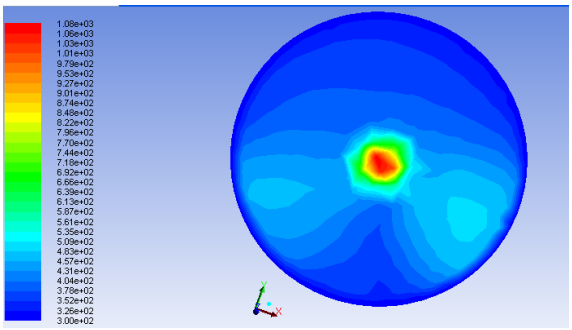

Z= 150 mm

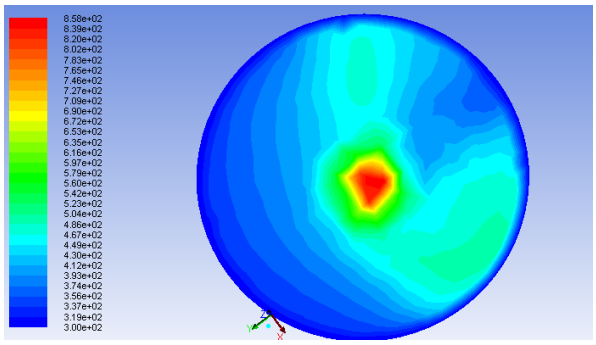

Z= 200 mm

Figure 4.29 : Flame temperature at different axial direction (($\emptyset = 0.5$)

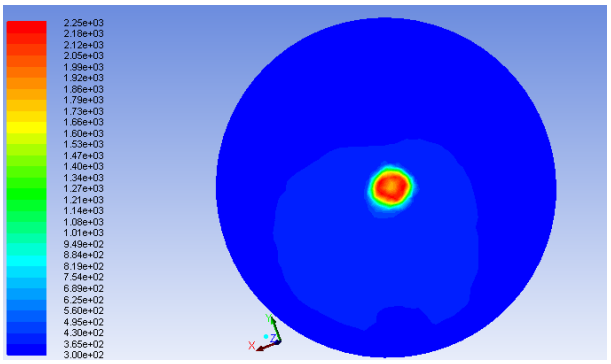

Z= 50 mm

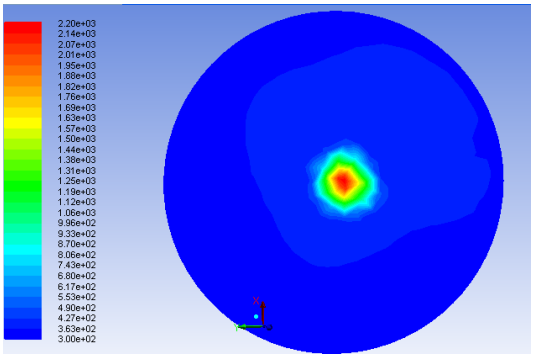

Z= 120 mm

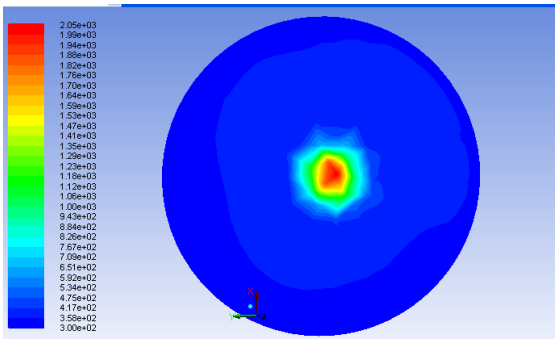

Z= 150 mm

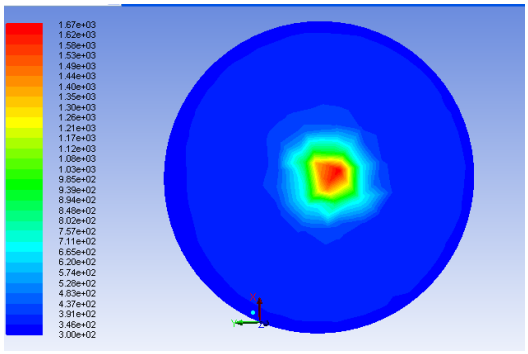

Z= 200 mm

Figure 4.30 **:** Flame temperature at different axial direction ($\emptyset = 0.75$)

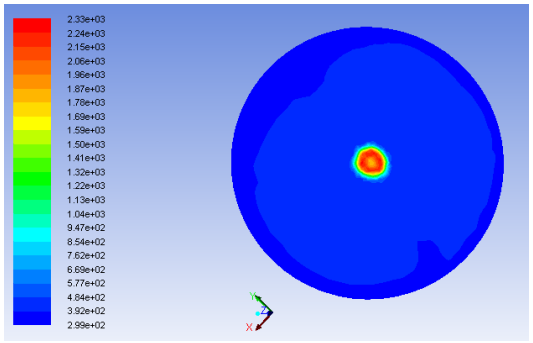

Z= 50

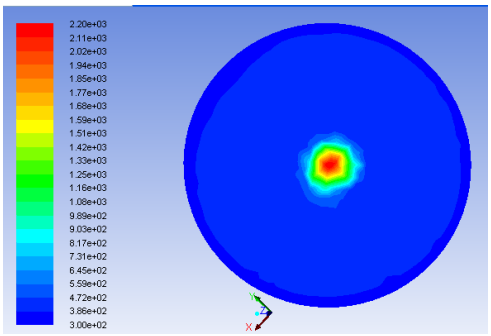

Z= 120

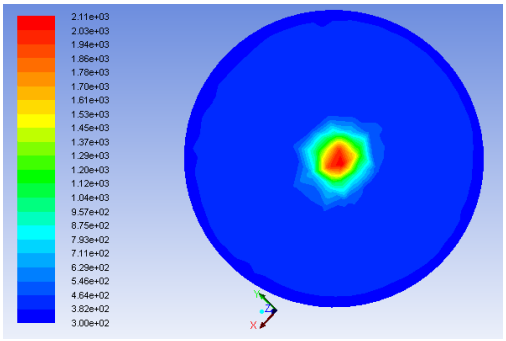

Z= 150

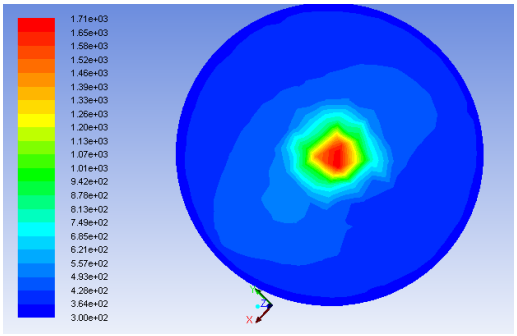

Z= 200

Figure 4.31**:** Flame temperature at different axial direction ((Ø = 1)

Figures 4.32 to 4.34 represent the mass fraction of NO_x (thermal + prompt) for an equivalence ratio of 0.5, 0.75 and 1, respectively and the quantity of NO_x is consistent with the flame temperature that means flame temperature increases with the increase of equivalence ratio. NO_x is increased in a similar fashion and finally was measured in terms of ppm; shown in Fig 4.35, 4.36and 4.37.

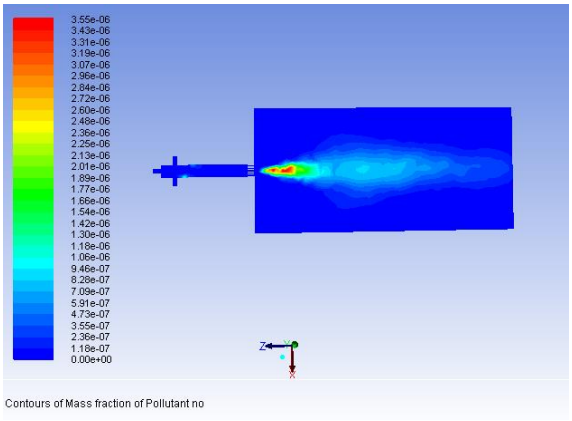

Figure 4.32 : Mass fraction of NO_x at an equivalence ratio of 0.5

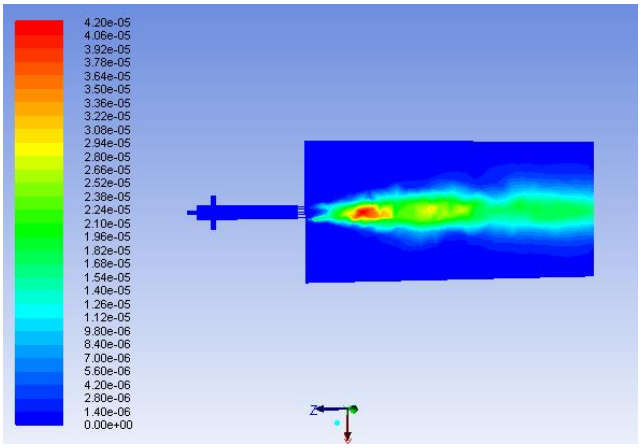

Figure 4.33: Mass fraction of NO_x at an equivalence ratio of 0.75

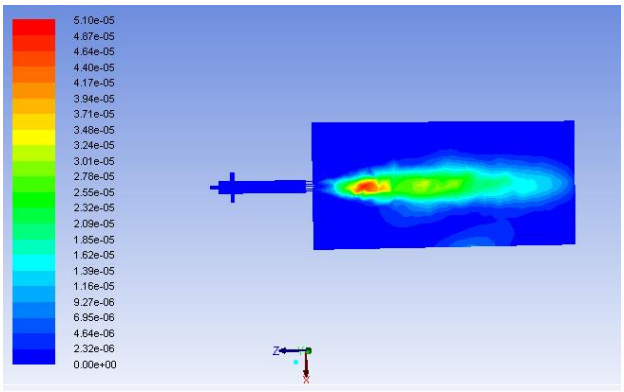

Figure 4.34 : Mass fraction of NO_x at an equivalence ratio of 1

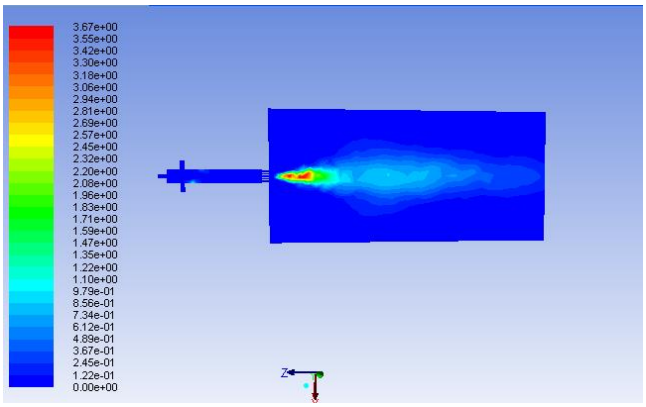

Figure 4.35 : Contour of NO_x in ppm at an equivalence ratio of 0.5

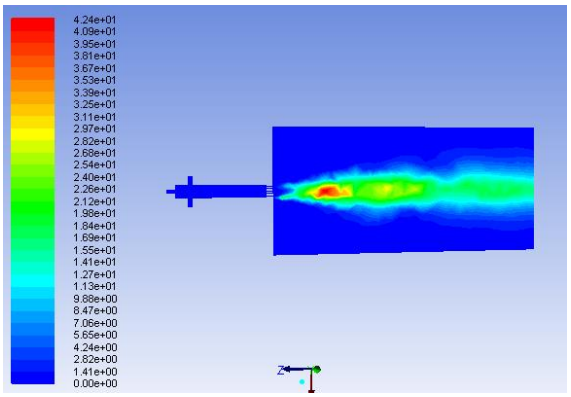

Figure 4.36 : Contours of NO_x in ppm at an equivalence ratio of 0.75

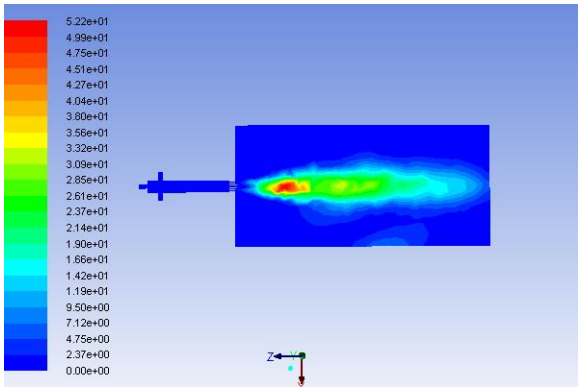

Figure 4.37 : Contours of NO_x in ppm at an equivalence ratio of 1

Chapter 5 : Experimental Results

Particle Image Velocimety (PIV) of cold flow analysis was done in order to evaluate flow behavior of the designed injector. Figure 5.1 shows the flow injected into the combustor with vectors showing the direction of flow from each orifice and velocity vector indicated no interactions with the adjacent jets. It was not possible to get the detailed flow behavior because of the recirculation of seeding particle that was caused by small throat area of the combustor.

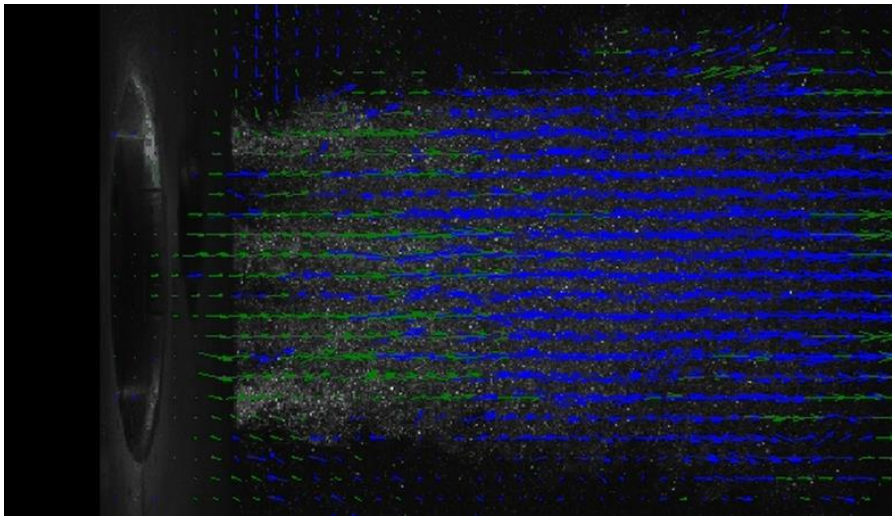

Figure 5.1 : Velocity vector captured by Particle Image Velocimetry (PIV)

Flame images at a blowout condition for 10%, 15%, 20% and 30% H_2 in the syngas mixture are presented in Fig 5.2. From the images it can be seen that the flame is first attached to the injector face. Heat is then transferred to the injector face causing the flame to quench, ultimately resulting in blowout.

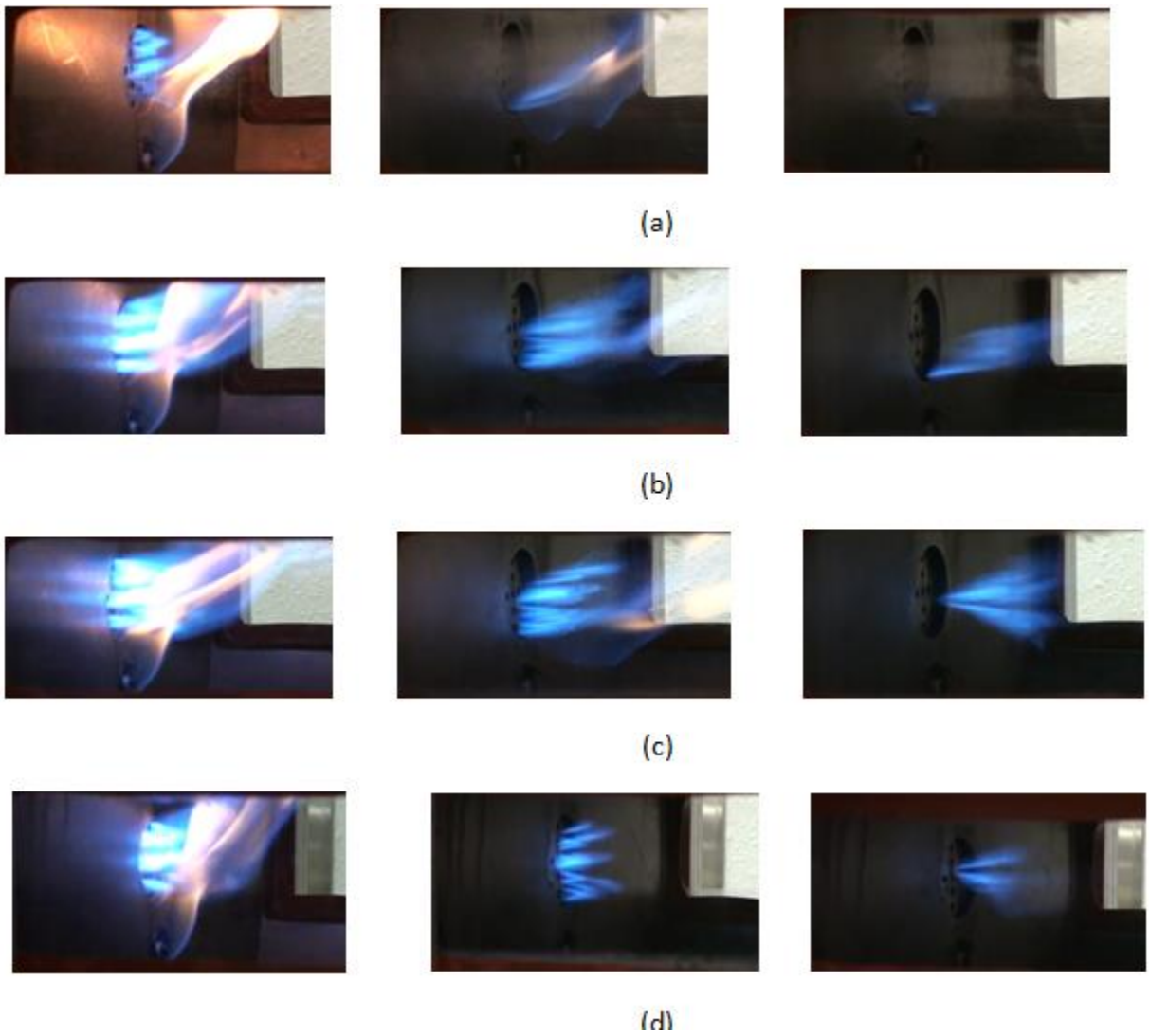

Figure 5.2 : Flame images for various synthetic gas compositions (a) 10%H_2 -90%CO (b) 15%H_2-85%CO, (c) 20%H_2 - 80% CO, and (d) 30%H_2 - 70% CO.

Figures 5.3, 5.4 and 5.5 show the critical velocity gradient at blowout conditions for syngas fuel compositions of 10%, 15%, 20% and 30%H_2 at three different conditions. The critical velocity gradient is plotted against different equivalence ratios for a jet velocity greater than flame speed, equal to flame speed and less than flame speed respectively. It is observed for each case that a critical velocity gradient increases with increasing concentration of hydrogen which indicates that the higher hydrogen concentration lowers the blowout tendency. The reason is that the

higher hydrogen concentration in the fuel expedites the chain reactions for the flame propagation by releasing the active radicals OH and O. The flame propagation is generally dependent on the diffusion rate of these radicals into unburned gas. Additionally, higher thermal diffusivity of syngas of higher hydrogen concentration helps to propagate flame and the designed multi-tube injector was completely able to mitigate flashback up to H_2 concentration of 30%. Surprisingly it was also not possible to get flame for 10% hydrogen below equivalence ratio of 1.1 at the condition of jet velocity greater than flame speed as shown in Fig 8 that did not allow capturing the blowout below the equivalence ratio of 1.1. At the condition of jet velocity equal to flame speed allowed the capture of blowout up to an equivalence ratio of 0.8.

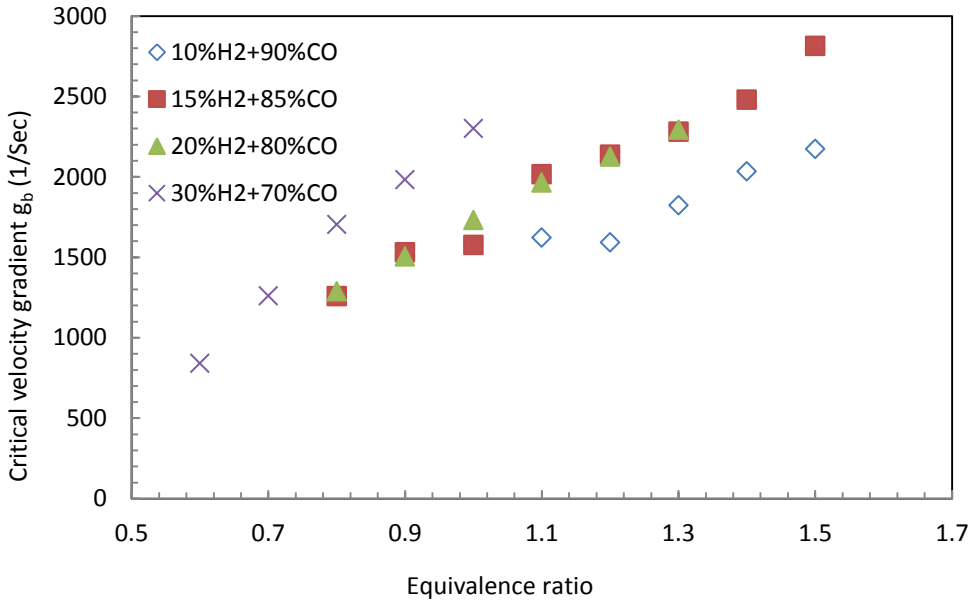

Figure 5.3: Critical velocity gradient at different mixture compositions at the condition of jet velocity greater than flame speed

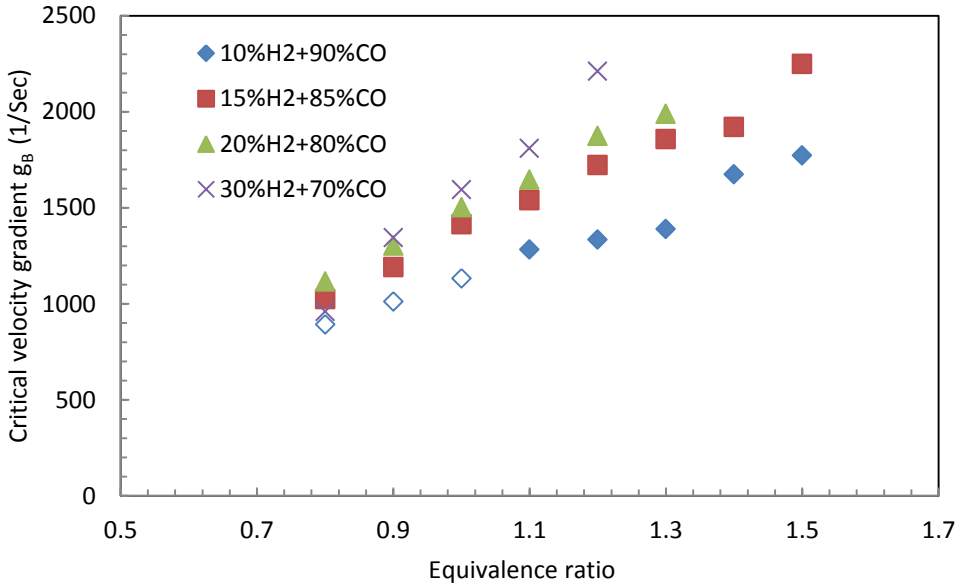

Figure 5.4 : Critical velocity gradient at different mixture compositions at the condition of jet velocity equal to the flame speed

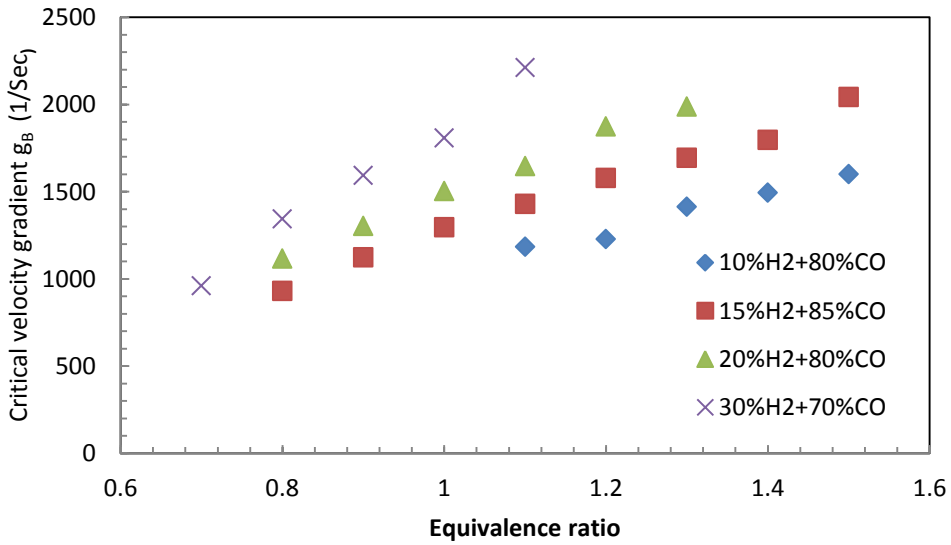

Figure 5.5 : Critical velocity gradient at different mixture compositions at the condition of jet velocity less than the flame speed.

Figures 5.6, 5.7 and 5.8 depict the correlation of critical velocity gradient with laminar burning velocity. A correlation between g_B, S_L and X_{bl}, can be used to develop a predictive model for flame blowout for this injector. Figure 5.6 shows the results for the condition of jet velocity greater than flame speed (Condition 1); Fig. 5.7 presents the results for a condition where the unburned gas velocity is equal to the flame speed (Condition 2) and Fig. 5.8 represents the results for a condition where the unburned gas velocity is less than the flame speed (Condition 3) The correlation constant, C is related to blow-off distance. Laminar flame speed of different compositions of syngas fuel at different equivalence ratio was calculated by CHEMKIN kinetic code, using the GRI 3.0 mechanism. A parametric model was used to get a correlation of blowout of syngas composition varying from 10% H2 to 30 % H2. Here critical velocity gradient is plotted against laminar flame speed. Results show that for condition 1- scaling constant somewhat agreed with the average value; for condition 2- scaling constant yielded the average value for 10% to 30% H_2; for condition 3- scaling constant yields approximately same value (10%, 15% and 20%) while for higher hydrogen concentration (30%) it shows relatively lower value than the lower hydrogen concentration. Conditions 2 and 3 show a very good agreement of two different conditions for different syngas composition up to 30% hydrogen while condition 1 showed different behavior that indicates that since jet velocity was maintained at the condition of greater than flame speed, it played a major role because all other parameters (flame speed, H_2 concentration, and thermal diffusivity) are same as other conditions. Tables 5.1, 5.2 and 5.3 summarize the correlation coefficient values for different compositions of syngas for condition 1, 2 and 3.

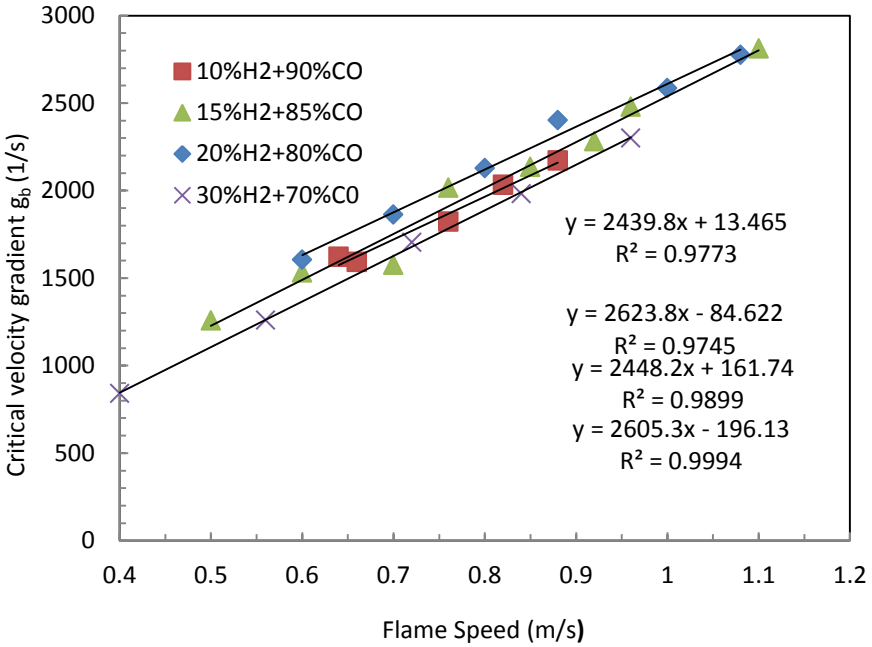

Figure 5.6 : Critical velocity gradient vs. laminar flame speed at different mixture compositions at the condition of jet velocity greater than the flame speed.

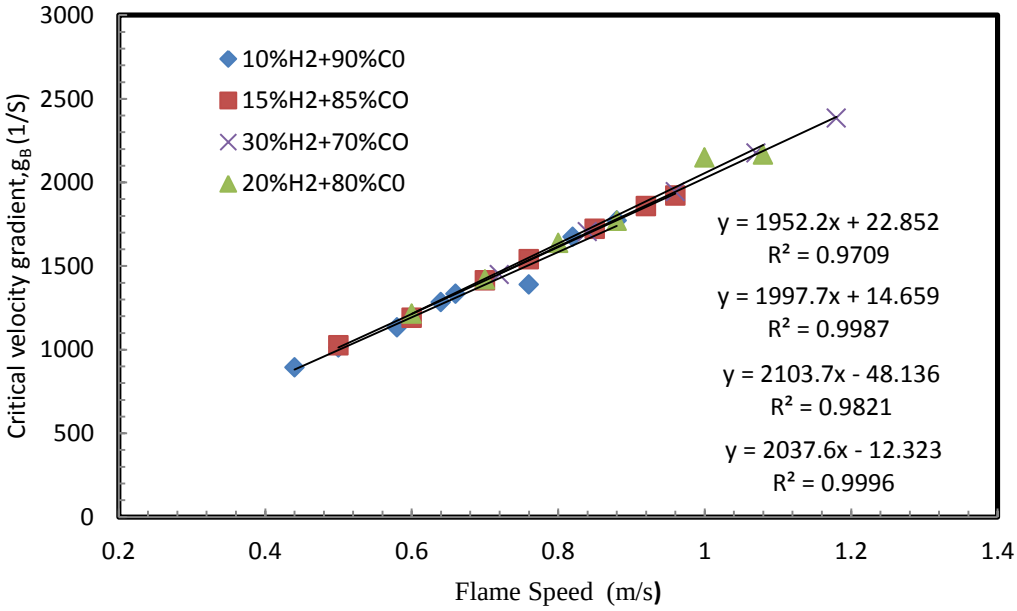

Figure 5.7: Critical velocity gradient vs. laminar flame speed at different mixture compositions at the condition of jet velocity equal to the flame speed.

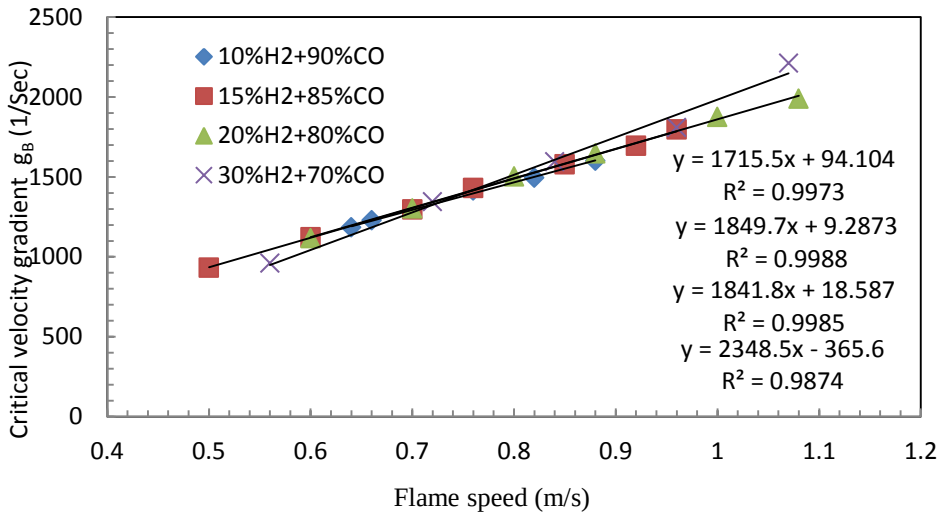

Figure 5.8: Critical velocity gradient vs. laminar flame speed at different mixture compositions at the condition of jet velocity less than the flame speed.

Table 5.1: Correlation coefficient for the blowout model for different syngas mixtures for a condition where jet velocity is greater than the calculated flame speed

Fuel composition	Correlation co-efficient (C)	R^2 value
10%H_2+90%CO	2439	0.97
15%H_2+85%CO	2623	0.97
20%H_2+80%CO	2448	0.98
30%H2+70%CO	2605	0.99

Table 5.2: Correlation coefficients for different syngas mixtures at exit jet velocities equal to the calculated flame speed

Fuel composition	Correlation co-efficient (C)	R^2 value
10%H_2+90%CO	1952	0.97
15%H_2+85%CO	1997	0.99
20%H_2+80%CO	2103	0.98
30%H2+70%CO	2037	0.99

Table 5.3: Correlation coefficients for different syngas mixtures at exit jet velocities less than the calculated flame speed

Fuel composition	Correlation co-efficient (C)	R^2 value
10%H_2+90%CO	1715	0.99
15%H_2+85%CO	1849	0.99
20%H_2+80%CO	1841	0.99
30%H2+70%CO	2348	0.98

Figures 5.9, 5.10 and 5.11 present a correlation between the flow Peclet Number (Pe_U) and the flame Peclet Number (Pe_{flame}) for 10%H_2+90%CO, 15%H_2+85%CO, 20%H_2+80%CO fuel and 30%H_2+70%CO mixtures for three different operating conditions. These terms include the laminar flame speed, unburned gas velocity and other transport properties such as thermal diffusivity which is also very influential in flame blowout. The dimensionless Peclet number analysis conjugates the flame speed with thermal diffusivity and helps to make a robust correlation for modeling blowout. The results show that for condition 1- correlation coefficient, C which is also related to Damköhler number (C=1/Da) for blowout apparently agrees for different syngas compositions up to 30% H_2 yielding Da of 2 except 15% H_2 syngas that yielded Da of 1.92; for condition 2- Damköhler number increases from 1.78 (10% H_2 syngas) to 2.0 (30% H_2 syngas); for condition 3 - Damköhler number decreases from 2.5 (10% H_2 syngas) to 1.78 (30% H_2 syngas).Condition 1 and 2 yields the average C value of 0.52 and 0.51 while condition 3 yield an average C value of 0.48 that indicates the effect of unburned gas velocity together with flame speed on blowout. The values of co-relation coefficients are also summarized in Tables 5.4, 5.5 and 5.6.

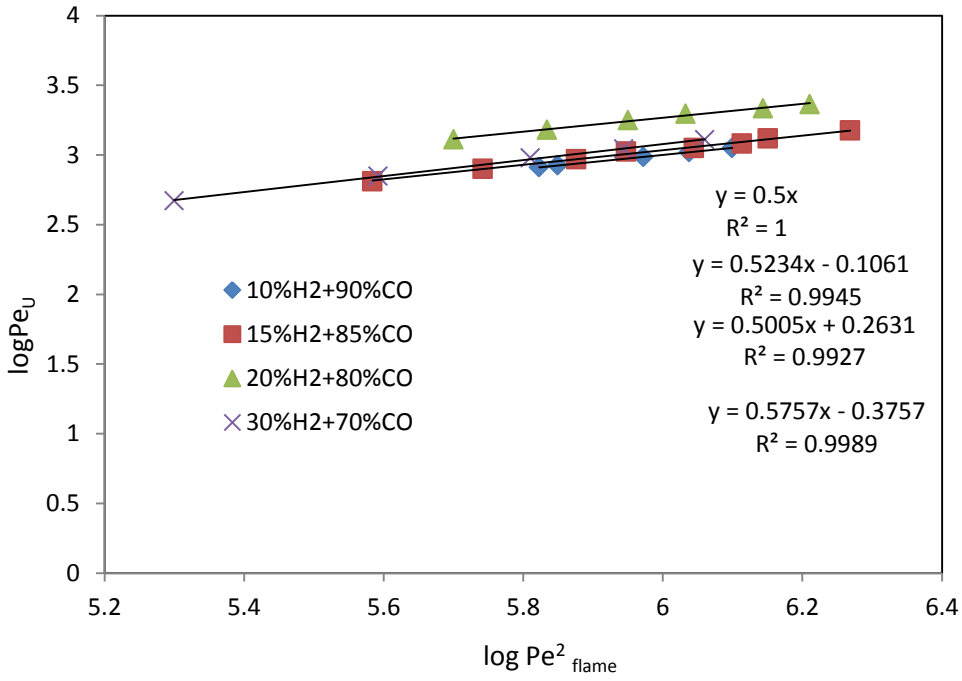

Figure 5.9: Peclet number model for different mixture compositions for a jet velocity greater than the calculated flame speed

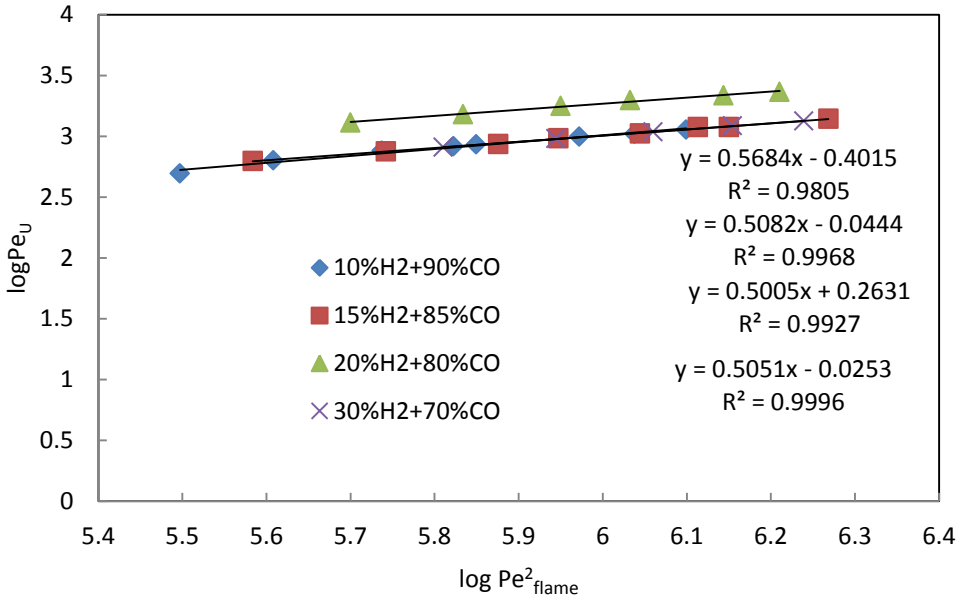

Figure 5.10: Peclet number model for different mixture compositions for a jet velocity equal to the calculated flame speed.

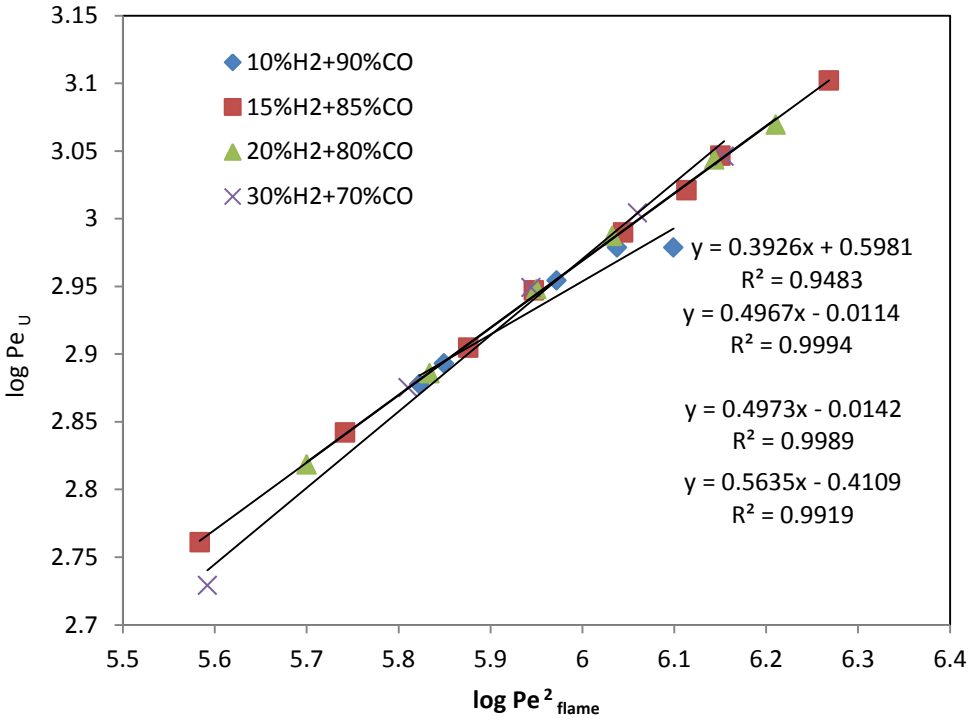

Figure 5.11 : Peclet number model for different mixture compositions for a jet velocity less than the calculated flame speed.

Table 5.4 : Correlation coefficient for the blowout model for different syngas mixtures for a condition where jet velocity is greater than the calculated flame speed

Fuel composition	**Correlation co-efficient (C)**	Da	**R^2 value**
10%H_2+90%CO	0.50	2.0	1
15%H_2+85%CO	0.52	1.92	0.99
20%H_2+80%CO	0.50	2.0	0.99
30%H_2+70%CO	0.57	1.75	0.99

Table 5.5: Correlation coefficient for the blowout model for different syngas mixtures for a condition where jet velocity is equal to the calculated flame speed

Fuel composition	**Correlation co-efficient (C)**	Da	**R^2 value**

10%H_2+90%CO	0.56	1.78	0.98
15%H_2+85%CO	0.50	2.0	0.99
20%H_2+80%CO	0.50	2.0	0.99
30%H_2+70%CO	0.50	2.0	0.99

Table 5.6 : Correlation coefficient for the blowout model for different syngas mixtures for a condition where jet velocity is less than the calculated flame speed

Fuel composition	**Correlation co-efficient (C)**	Da	**R^2 value**
10%H_2+90%CO	0.40	2.5	0.94
15%H_2+85%CO	0.49	2.0	0.99
20%H_2+80%CO	0.49	2.0	0.99
30%H_2+70%CO	0.56	1.78	0.99

Chapter 6 : Summary and Conclusions

This present work consists of five individual parts: (1) Design of the high pressure turbine combustor, (2) Development and construction of the combustor, (3) Integration of control and ignition system, (4) Characterizing the flame stability of synthetic gas mixtures using the novel multi-tube injector and establishing a relationship to predict the stability of a particular fuel-air mixture for this type of injector, and (5) Computationally modeling the pollutant emissions expected from the use of the new fuel injector.

The designed high pressure combustor is rated up to 1.5 MPa pressure and 500 kW thermal powers. This design is made to withstand temperatures based on the adiabatic flame temperature of a 30% H_2-70% CO mixture which is 2400K. Finite element was used as a technical approach to obtain the wall thickness of the combustion chamber. The combustor has four different sections- inlet manifold, front cap, combustion chamber, and end capping. In order to ensure proper mixing the static mixture section of inlet manifold will eliminate injection induced flow irregularities of fuel -air mixture. After mixing, the fuel and air pass to the combustion chamber which can accommodate non-swirl stabilized, swirl flow, and center-body stabilized swirl flow flame. The inlet manifold is connected with the combustor through front cap which also accommodates the ignition system. Because of this modular connection we have the flexibility for the installation of different fuel injection systems. The variable throat area allows maintaining the desired pressure inside the chamber and the calculated throat area to maintain 1.5 MPa pressure inside the chamber is 6.35 mm^2. Based on finite element analysis, the wall thickness of stainless steel chamber is 88.9 mm and 50.8 mm for the quartz windows. Copper coiling will be used on the stainless steel chamber to reduce the thermal stress where water will be used as

driving fluid and inner quartz chamber will be convectively cooled using nitrogen. The entire design is now completely designed and built.

A LabVIEW control system has also been integrated into this developed high pressure combustor. Proportion control valves are used for regulating gas flow, solenoid valves are used for emergency shutdown. Pressure transducers are also incorporated to get the line pressure. A diffusion flame was used in order to ignite the main fuel-air stream where a modified spark plug was installed as an ignition source. Initially functional test of the equipment, leak test and pressure test were carried out prior to conducting the ignition experiments. Currently, the system has been tested to withstand the maximum pressure allowed by the air compressor which is 758 kPa. Ignition test was carried out at lean condition and the installed ignition system successfully ignited the fuel-air stream which ensures that this high pressure combustor is ready to be operational to conduct the experiments.

A cold flow simulation was carried out for the multi-tube injector using a LES solver. The result showed that flow is coming out as a jet from each port and after an axial distance of 50 mm from injector face; jets are interacting with flow from the various ports. Since the area right after the injector is a point of interest, a close observation at that point revealed that strong interactions between the orifices that are distant by 7 mm and show a weak interaction between the orifices that are distant by 10 mm. NOx emission characteristics of the designed injector were evaluated using numerical simulation. Models used for flow of syngas fuel and combustion are the k-ε model for turbulent flows, mixture fractions/PDF model for partially premixed gas combustion, and P-1 radiation model respectively. The temperature profiles at different equivalence ratios revealed that the flame was lifted at the simulated condition, which was also experienced during

experimental testing. The partially premixed combustion model was used and location of OH radical concentrations was found to be followed by higher temperature zone. The magnitude of 4, 42 and 52 ppm NO_x concentration was measured for equivalence ratio of 0.5, 0.75 and 1 accordingly in the region of the reaction zone.

Blowout characteristics of syngas mixtures emitted from a novel multi-tube injector have been studied for syngas from 10% to 30% hydrogen concentration in carbon monoxide (CO).

Three different conditions were tested for these compositions:

- where jet velocity was greater than the laminar flame speed (condition 1)
- where the jet velocity was equal to the flame speed (condition 2)
- Where jet velocity was less than the flame speed (condition 3)

Parametric modeling

- Critical velocity gradient g_B which was defined as the ratio of laminar burning velocity to blow-off distance was used to make a correlation between blowout behavior of different syngas compositions at three different conditions .
- A dimensionless parameter, Peclet number, was also used to capture the blowout characteristics of the injector at three operating condition.

Results showed that

- The degree of blowout tendencies decreased with increasing hydrogen concentration for this multi-tube injector for all three conditions.
- Modeling of the critical velocity gradient with respect to flame speed reveal that

1. Correlation coefficient (scaling constant) agreed at the average value for all syngas compositions that also indicates that hydrogen concentration has negligible effect on scaling constant for condition 1 when jet velocity is higher than the flame speed.
2. For condition 2, where the jet velocity is equal to flame speed, the scaling constant yielded the average value for 15% to 30% H_2 concentration and differ for lowest hydrogen concentration (10% hydrogen).
3. For condition 3 where jet velocity is lower than flame speed, scaling constant yielded the average value for 10% to 20% H_2 but it yielded relatively greater value for 30% H_2 that indicates the effect of higher hydrogen concentration on scaling constant.

Though Peclet modeling yielded apparently same correlation coefficient but in terms of Damköhler number it was observed that,

1. For condition 1- correlation coefficient, C which is also related to Damköhler number (C=1/Da) for blowout apparently agrees for different syngas compositions up to 30% H_2 yielding Da of 2.
2. For condition 2- Damköhler number increases from 1.78 (10% H_2 syngas) to 2.0 (30% H_2 syngas).
3. For condition 3 - Damköhler number decreases from 2.5 (10% H_2 syngas) to 1.78 (30% H_2 syngas).

Appendix:

Nomenclature

α	=	Thermal diffusivity	[m^2/s]
λ	=	Thermal conductivity	[W/m.K]
ρ	=	Density	[kg/m^3]
σ_s	=	Scattering coefficient	[1/m]
γ	=	Specific heat ratio	
A	=	Chamber area	[m^2]
A_T	=	Throat area	[$m^{2]}$
a	=	Absorption coefficient	[1/m]
C_p	=	Specific heat constant	[J/kg.K]
C	=	Correlation constant	
G	=	Incident radiation	[W/m^2]
g_b	=	Critical blowout velocity gradient	[1/s]
h	=	Heat transfer co- efficient	[W/ (m^2-K)]
J	=	Molecular diffusion flux	[mol / (m^2-s)]
M	=	Mach number	
P_c	=	Chamber pressure	[MPa]
P_t	=	Pressure at throat	[MPa]
T_c	=	Chamber temperature	[K]
T_{Ad}	=	Adiabatic Flame temperature	[K]
T_∞	=	Ambient temperature	[K]
t	=	Experiment time	[min]
P	=	Pressure	[Mpa]
R	=	Radius of the tube	[m]
S_L	=	Laminar flame speed	[m/s]
V	=	Volumetric flow rate	[m^3/L]
W	=	Molecular weight	[kg]
$\dot{w}$	=	Rate of production of speies	[mol/ (L-s)

Experimental Procedure:

Hardware and software elements

Ensure that the system meets the following criteria:

1. Computer set-up:

Processor	Pentium III/Celeron 866 MHz or equivalent
RAM	256 MB
Screen Resolution	1024 x 768 pixels
Operating System	Windows 8/7/Vista (32-bit and 64-bit) Windows XP SP3 (32-bit) Windows Server 2003 R2 (32-bit) Windows Server 2008 R2 (64-bit)
Disk Space	382 MB

2. Lab View Software- *Installed In PC*

Equipment Requirements

Ensure that the following equipment is installed in the system. Refer to the equipment manual.

Equipment/Instruments	Quantity	X
Power supply- EXTECH Instruments 382270	1	
Power Supply-	1	
USB Ni-6008 Dev3	1	
USB Ni-6008 Dev6	1	
PCI 6521 Relay Card	1	
Ignition Coil- MSD 8287 PN 121-8287 (or equivalent)	1	
12 V Battery / 11 amp	1	
BK Precision 4012A Signal Generator (or equivalent)	1	
KZ Valve EH2 Series (“P”)	4	
Jefferson Valve 1314 Series (“S”)	4	
Omega FMA Series 1700/1800 Flow meters (“FM”) 0-5 lpm	1	
Omega FMA Series 1700/1800 Flow meters (“FM”) 0-30 lpm	1	
Omega FMA Series 1700/1800 Flow meters (“FM”)0-500 lpm	1	
Omega FMA Series 1700/1800 Flow meters (“FM”)0-1000 lpm	1	
Video Camera (with TV connection)	1	
Television (with Video Camera Connection)	1	
120V wall connection		

Nomenclature

Instrument/equipment is identified with the following nomenclature:

Equipment/Instrument	Nomenclature
Proportional Control Valve	P
Solenoid Valve	S
Flow Meters	F
Needle Valve	N
High Pressure Combustor	HPC
Pressure transducer	PT

Assign a testing gas/fuel to a corresponding number. Refer to Set-up Diagram

Gas	Number Code
Hydrogen(H_2)	1
Carbon mono oxide (CO)	2
Air	3
Ignition, Methane CH_4	4

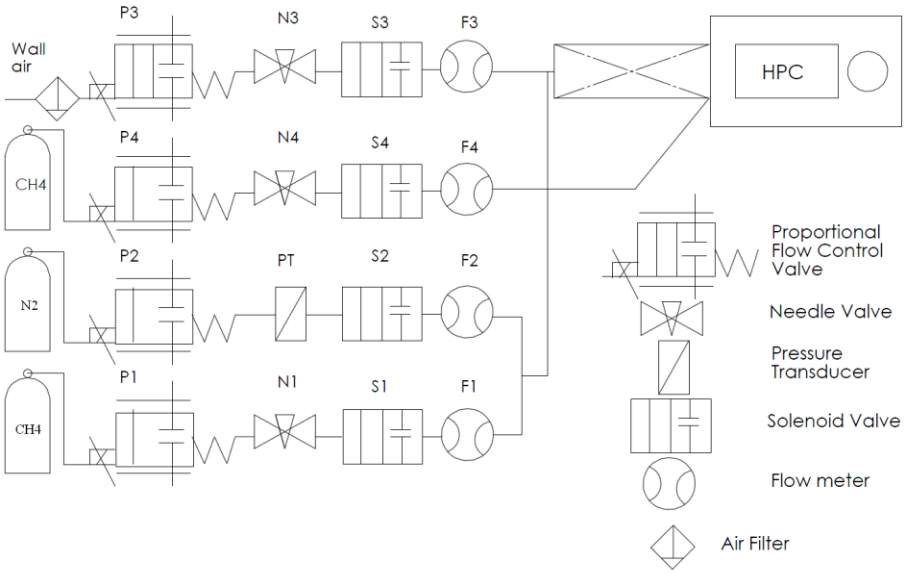

System set-up Diagram

Testing Requirements

Ensure that the following is available before testing. The amount of material/gas depends in the testing needs.

Gas	Quantity	X
Hydrogen(H_2)		
Carbon mono oxide (CO)		
Air	Wall	
Ignition, Methane CH_4		

SET-UP PROCEDURE

Follow these tasks in order to set-up the HPC system for testing.

#	TASK	RESULT	IF ADVERSE RESULT	X or N/A
COMPUTER SET-UP				
1	Turn ON Computer	Verity computer is ON	N/A	
2	Open "New_HPC" Lab View File	Lab view program appears in the computer desktop screen	▪ Verify lab view is installed ▪ Verify lab view is running	
EQUIPMENT SET-UP				
1	Connect the following equipment to 120V wall outlet: ▪ Power Supplies ▪ Signal Generator	N/A	N/A	
2	Turn ON Power Supplies	Verify numbers appear in screen	Check Electricity Connection	
3	Verify FM are turned ON	Check for numbers in the display screen	Refer to FM troubleshooting document.	
4	Allow FM to warm-up 10-15 min	Numbers in display screen approximate 0.0 +/- 5% of total volume flow rate of FM after warm-up	Refer to FM troubleshooting document.	
Locate MSD ignition coil				
5	Connect MSD ignition coil to the spark plug located at the HPC front cap if not connected.	N/A	N/A	
6	Connect cables to MSD ignition Coil if not connected. (Refer to Electrical diagram for MSD ignition coil)	N/A	N/A	
Locate 12V battery, Green and Red Alligator Clamps and Signal Generator				
7	Connect Green clamp to the (-) terminal of the 12V battery	N/A	N/A	
8	Connect Red clamp to the (+) terminal of the 12V battery	N/A	N/A	
9	Turn ON the Signal Generator	Check for Number in the screen display	Verify the signal generator is connected to the 120V outlet	
10	Set-up 100HZ frequency in the	"100" should be displayed	Adjust as necessary	

	signal generator using the knobs under the screen	in the screen		
#	**TASK**	**RESULT**	**IF ADVERSE RESULT**	**X or N/A**
11	Push the "Step Function" button	N/A	N/A	
EQUIPMENT TEST				
12	Run Lab View Program "New_HPC"	N/A	N/A	
The following tasks will be executed using Lab View				
13	Activate S1	Must hear "Click" sound and current should be supplied to the solenoid	Refer to the troubleshoot guide	
14	Deactivate S1	Solenoid will close and current is no being supplied	Refer to the troubleshoot guide	
15	Activate S2	Must hear "Click" sound and current should be supplied to the solenoid	Refer to the troubleshoot guide	
16	Deactivate S2	Solenoid will close and current is no being supplied	Refer to the troubleshoot guide	
17	Activate S3	Must hear "Click" sound and current should be supplied to the solenoid	Refer to the troubleshoot guide	
18	Deactivate S3	Solenoid will close and current is no being supplied	Refer to the troubleshoot guide	
19	Activate S4	Must hear "Click" sound and current should be supplied to the solenoid	Refer to the troubleshoot guide	
20	Deactivate S4	Solenoid will close and current is no being supplied	Refer to the troubleshoot guide	
21	Supply 5V to P1 (enter value in Lab View)	▪ Must hear opening sound for P. ▪ Verify the Red arrow on top of the P is not perpendicular to the line.	Refer to the troubleshoot guide	
22	Enter value 0 volts for P1 in Lab View	▪ Must hear closing sound for P. ▪ Verify the Red arrow on top of the P is perpendicular to the	Refer to the troubleshoot guide	

		line.		
23	Supply 5V to P2 (enter value in Lab View)	▪ Must hear opening sound for P. ▪ Verify the Red arrow on top of the P is not perpendicular to the line.	Refer to the troubleshoot guide	
24	Enter value 0 volts for P2 in Lab View	▪ Must hear closing sound for P. ▪ Verify the Red arrow on top of the P is perpendicular to the line.	Refer to the troubleshoot guide	
#	**TASK**	**RESULT**	**IF ADVERSE RESULT**	**X or N/A**
25	Supply 5V to P3 (enter value in Lab View)	▪ Must hear opening sound for P. ▪ Verify the Red arrow on top of the P is not perpendicular to the line.	Refer to the troubleshoot guide	
26	Enter value 0 volts for P3 in Lab View	▪ Must hear closing sound for P. ▪ Verify the Red arrow on top of the P is perpendicular to the line.	Refer to the troubleshoot guide	
26	Supply 5V to P4 (enter value in Lab View)	▪ Must hear opening sounds for P. ▪ Verify the Red arrow on top of the P is not perpendicular to the line.	Refer to the troubleshoot guide	
27	Enter value 0 volts for P4 in Lab View	▪ Must hear closing sound for P. ▪ Verify the Red arrow on top of the P is perpendicular to the line.	Refer to the troubleshoot guide	
28	Activate Ignition Coil Button	Must observe spark generated from spark plug. • Spark plug is located inside in	Refer to the troubleshoot guide	

		the front cap inside HPC		
SET UP VIDEO CAMERA				
29	Locate video camera and stand	N/A	N/A	
30	Locate screen for video camera	N/A	N/A	
31	Set-up camera and monitor	The injector face and pilot flame port should be clearly visible.	N/A	
Once these tasks have been completed, proceed to "HPC Leak Test procedure"				

HPC Leak Test Procedure

Note: The valve names are defined in the Lab VIEW program generated by the HPC team. As of 10/24/2013 the file name is "New_HPC". The file can be found in the cSETR lab computer designated to this experimental setup. For additional information refer to the Lab VIEW block diagram.

1. Open the exhaust damper and ensure the exhaust system is running

2. Connect the shop airline hose to the main airline regulator (Refer to the plumbing diagram. The air supply should be connected to the line that has the P3, N3, S3 and F3 installed. Set the regulator pressure to 40 psig).

   I. Open P3

      - Apply snoop leak detection solution to all line joints between the airline hose connection and N3.
      - Tighten necessary joints or apply Teflon accordingly until leak has sopped.

   II. Open N3

      - Apply snoop leak detection solution to all line joints between N3 and S3.

- Tighten necessary joints or apply Teflon accordingly until leak has sopped.

III. Open S3

- Plug the HPC exhaust hole in order to ensure a pressure buildup across the line and combustor
- Apply snoop leak detection solution to all line joints between S3 and inlet manifold.
  - A through leak test of the combustor can be performed now by applying the leak detection solution to all the combustor joints and window panels. This step is recommended before initial experimentation and is thereafter left to the discretion of the user.

3. Repeat step 2 for all the remaining lines that will be utilized during experimentation

Setting Desired Flow Rates

1. Connect the shop airline hose to the main airline regulator (Refer to the plumbing diagram. The air supply should be connected to the line that has the P3, N3, S3 and F3 installed. Set the regulator to the desired pressure).

I. Turn on and allow the flow meters to stabilize.

- Turn on both power supplies (one for flow meters and another for valves)
- The flow meters will initially read a value near their maximum. No flow should be allowed to pass through until they have stabilized at a value of 0 L/min.

II. Open P3 and S3

- Set N3 so that F3 reads the value dictated by the test matrix

2. Repeat step 1 for all the lines with needle valves installed in them

Test Procedure

Note: The leak test procedure and the flows must be set based off the experimental test matrix before performing the experimental procedure. Two separate methane cylinders are used in the setup, one for the main fuel line and another for the pilot flame. This test procedure is meant for a maximum flow rate of air of 50 L/min and a maximum CH_4 flow rate of 10 L/min at an equivalence ratio of .9.

1. Connect the shop airline hose to the main airline regulator (Refer to the plumbing diagram. The air supply should be connected to the line that has the P3, N3, S3 and F3 installed. Set the regulator to 40 psig).
2. Connect the main CH_4 cylinder tank to the main fuel line
    I. As of 10/24/2013 the main fuel line is the one with P1, N1, S1 and F1 installed (Refer to plumbing diagram)
3. Connect the CH_4 tank to the pilot flame line
    I. As of 10/24/2013 the pilot fuel line is the one with P4, N4, S4 and F4 installed (refer to plumbing diagram)
    II. The flow meter for the pilot flame line should not exceed 5.5 L/min or be less than .5 L/min
4. Connect the N_2 tank to the emergency purging line

I. As of 10/24/2013 the N_2 purging line is the one with P2, PT, S2 and F2 installed (refer to plumbing diagram)

II. The N_2 tank could be replaced by standard shop air and it is left up to the user discretion.

5. Ensure the HPC exhaust damper is open and the exhaust system is running and functioning properly
    I. The HPC exhaust damper should be the only one open at the time of experimentation. All other dampers should be closed with the consent of the other students working in the lab
    II. No other experiment should be using the exhaust while HPC experimentations are taking place.
6. Set the camera and ensure a clear image in the remote monitor is visible. The injector face and pilot flame port should be clearly visible
    I. Camera should always be set to recording to keep it from switching to sleep mode
7. Place Kevlar walls around the set up
    I. A total of 4 Kevlar walls should be placed around the HPC
8. Open the CH_4 tanks and N_2 tank and set line pressure to 40 psig
9. Activate the ignition coil
    I. A spark should be heard and seen through the remote monitor
10. Open S4 and P4 (Pilot line)
    I. A diffusion flame should be visible and anchored to the pilot flame port after 3 seconds of opening P4
11. Open S3, then open P3

12. Open S1, then open P1

    I. A flame should be generated at the injector face for evaluation after 5 seconds of opening P1

References:

Ardha, V., Dam, B., Love, N., Choudhuri, A., Effect of Local Flow Field Fluctuations on Characteristics of Turbulent Flames, Int. Energy Conversion Engineering Conference 2011, DOI: 10.2514/6.2011-5595.8.

Bell, J.B., Cheng, R.K., Day, M.S., Shepherd, I.G., "Numerical simulation of Lewis number effects on lean premixed turbulent flames," Lawrence Berkeley National Laboratory, Berkeley, CA 94720, USA.

Blanc, M.V., Guest, P.G., Von Elbe, G., Lewis, B., "Ignition of Explosive Gas Mixtures by Electric Sparks: Minimum Ignition Energies and Quenching Distances of Mixtures of Hydrocarbons and Ether with Oxygen and Inert Gases", Symposium on Combustion and Flame, and Explosion Phenomena. 1949; 3: 393-367.

Bouvet, N., Lee, S.-Y., Gökalp, I., Santoro, R. J. "Flame Speed Characteristics of Syngas (H2-CO) with Straight Burners for Laminar Premixed Flames", Third European Combustion meeting, 2007.

Cai, J., Jeng, S.M., Tacina, R., "Multi-swirler Aerodynamics: Comparison of Different Configuration, ASME Turbo Expo 2002, doi: 10.1115/GT2002-30464.

Dam, B., Love,N., Choudhuri,A., "Flashback Propensity of Syngas Fuels," Fuel,2011; 90: 618–625.

Dam, B., Corona, G., Hayder. M., Choudhuri, A.,"Effects of Syngas Composition on Combustion Induced Vortex Breakdown (CIVB) Flashback in a Swirl Stabilized Combustor", Fuel,2011;90:3274-3284.

Daniele, S.,Jansohn, P., Boulouchos, K., "Experimental Investigation of Lean Premixed Syngas Combustion at Gas Turbine Relevant Conditions: Lean Blow Out Limits, Emissions and Turbulent Flame Speed", Combustion Colloquia, 2009.

Daniele, S., Jansohn, P., Boulouchos, K., "Flashback Propensity of Syngas Flames at High Presuure: Diagnostic and Control,"ASME Turbo Expo, 2010,DOI: 10.1115/GT2010-23456.

Davidson, P. A. Turbulence: an Introduction for Scientists and Engineers. Oxford, UK: Oxford UP, 2004. G

Davu, D., Franc, R., Choudhur,i A., Lewis, R., "Investigation on Flashback Propensity of Syngas Premixed Flames, Joint Propulsion Conference and Exhibit, 2005, DOI: 10.2514/6.2005-35859.

Description of PSU's High Pressure Combustion Lab Capabilities and Projects, Pennsylvania State University, http://www.hpcl.psu.edu/_notes/CPIAC%20Bulletin.doc.

Dodo,S., Asai,T., Koizumi,H., Takahashi,H., Yoshida,S., Inoue,H., "Performance of a Multiple-Injection Dry Low NOx Combustor With Hydrogen-Rich Syngas Fuels", Journal of Engineering for Gas Turbines and Power ,2013;135 /:011501.1.- 011501.7.

Durbin, Paul A., and B. A. Pettersson. Reif. Statistical Theory and Modeling for Turbulent Flows. Chichester, West Sussex: Wiley, 2011.G

Edwardsport Integrated Gasification Combined Cycle plant (IGCC) Station, http://www.duke-energy.com/about-us/how-igcc-works.asp.

Eichler, C., Baumgartner, G., Sattelmayer, T., "Experimental Investigation of Turbulent Boundary Layer Flashback Limits for Premixed Hydrogen-Air Flames Confined in Ducts", Journal of Engineering for Gas Turbines and Power, 2012; 134:011502.1-11502.8.

FACT SHEET: "Clean Coal" Power Plants (IGCC), ENERGY JUSTIC.net, http://www.energyjustice.net/files/coal/igcc/factsheet-long.pdf.

Ferrières,S., Bakalia,A., Gasnota, L., Monterob,M., Pauwelsa, J.F., " Kinetic Effect of Hydrogen Addition on Natural Gas Premixed Flames",Fuel,2013;106:88–97.

Fluent Inc.2001-11-29,http://combust.hit.edu.cn:8080/fluent60_help/html/ug/node579.htm

Frank J, Miller M, Allen M, "Imaging of laser-induced fluorescence in a high pressure combustor", Aerospace Sciences Meeting and Exhibit 1999, DOI: 10.2514/6.1999-773.

Fritz, J., Kroner, M., and Sattelmayer, T., "Flashback in a Swirl Burner with Cylindrical Premixing Zone," Journal of Engineering for Gas Turbines and Power, 2004; 126:276-283.

Fu, J., Tang, C., Jin, W., Thi,L., Huang,Z., Zhang ,Y., "Study on Laminar Flame Speed and Flame Structure of Syngas with Varied Compositions using OH-PLIF and spectrograph," International Journal of Hydrogen Energy, 2013;38,2013:1636 -1643.

Ghenai, C., "Combustion of Syngas Fuel in Gas Turbine Can Combustor,"Indawi Publishing Corporation, Advances in Mechanical Engineering,2010,DOI:10.1155/2010/342357.

Giles, D.E., Som, S., Aggarwal ,S.K., "NOx Emission characteristics of Counterflow Syngas Diffusion Flames with Airstream Dilution", Fuel,2006; 85 (2006):1729–1742.

Griebel, P., Boschek, E., Jansohn, P., "Lean Blowout Limits and NOx Emissions of Turbulent, Lean Premixed, Hydrogen-Enriched Methane/Air Flames at High Pressure," Journal of Engineering for Gas Turbine and Power, 2007; 129; 404-410.

Guo,H., Smallwood, G.J., Liu,F., Ju,Y., Gülder, O.L.,"The Effect of Hydrogen Addition on Flammability Limit and NOx Emission in Lean Counterflow CH4/Air Premixed Flames", Proc. Combustion Institute, 2004;Vol.30.

Hariharan,P., Periasamy,C., Gollahalli, S.R. "Effect for Elliptical Burner Geometry and Air Equivalence Ratio on the nitric oxide emissions from turbulent hydrogen flames", International Journal of Hydrogen Energy, 2007; 32:1095–1102.

Hayashi, S., Yamada, H., Makida, M, "Extending Low-NOx Operating Range of a Lean Premixed–Prevaporized Gas Turbine Combustor by Reaction of Secondary Mixtures Injected into Primary Stage Burned Gas ",Proceedings of the Combustion Institut,2005;30 :2903–2911.

High Pressure combustion Facility, Cambridge University, Department Of Engineering, Combustion of Gas Turbines, http://www-g.eng.cam.ac.uk/gtcombustion/facilities/index-facilities.html

High pressure Combustion Facility,NETL, http://www.netl.doe.gov/onsite_research /Facilities/high-pressure.html.

Hollon, B., Steinthorsson, E., Mansour, A., McDonell V, Lee H, Ultra-Low Emission Hydrogen/Syngas combustion with a 1.3 MW injector using a micro-mixing lean-premix system, ASME Turbo Expo,2011, doi:10.1115/GT2011-45929.

Hu, E., Huang, Z., He, J., Miao, H., "Experimental and Numerical Study on Laminar Burning Velocities and Flame Instabilities of Hydrogen–air Mixtures at Elevated Pressures and Temperatures", International Journal of Hydrogen Energy,2009 ;34 ,2009: 8741–8755.

Juste, G.L "Hydrogen Injection as Additional Fuel in Gas Turbine Combustor. Evaluation of Effects", International Journal of Hydrogen Energy, 2006; 31; 2112–2121.

Khalil,A., Gupta, A.K.,"Hydrogen,"Addition Effects on High Intensity Distributed Combustion", Applied Energy, 2013;104:71–78.

Kiesewetter, F., Kirsch, C., Fritz, J., Kroner, M., and Sattelmayer, T., 2003, "Two-Dimensional Flashback Simulation in Strongly Swirling Flows," Proceedings of ASME Turbo Expo, 2003.

Kono, M., Kumagai, S., Sakai, T., 1977. “The optimum Condition for Ignition of Gases by Composite Sparks”, Synposium on Combustion, 1977; 16:757–766.

Kröner, M., Fritz, J., and Sattelmayer, T., “Flashback Limits for Combustion Induced Vortex Breakdown in a Swirl Burner”, Journal of Engineering for Gas Turbines and Power, 2003; 125:693-700.

Lewis, B., Elbe V.G., “Stability and structure of burner flames”, The Journal of Chemical physics 1943; 75.

Liewen, T, Novel, D.R., Zhang, Q, 2007 “Characterization of Fuel Composition Effects in H2/CO/CH4 Mixtures upon Lean Blowout”, Journal of Engineering for Gas Turbines and Power, 2006; 129; 688-694.

Marek, J.C., Smith, T.D., Kunudu, K., “Low Emission Hydrogen Combustors for Gas Turbines using Lean Direct Injection,” Joint Propulsion Conference and Exhibit,2005; paper no.3776.

Mcmillan, R., Marriot, D., Ri Han, S., “Fuel -Flexible –Gas turbine –cogeneration”, Siemens,http://www.energy.siemens.com/br/pool/hq/energy-topics/pdfs/en/gas-turbines-power-plants/Fuel-Flexible-Gas-Turbine-Cogneration.pdf.

Morsy, M.H., Chung, S.H., “Laser-induced Multi-point Ignition with a Single-shot Laser Using Two Conical Cavities for Hydrogen/air Mixture.” Experimental, Thermal and Fluid Science, 2003; 27: 491-497.

Noble, D.R., Zhang, Q., Shareef, A., Tootle, J., Meyers A., Lieuwen, T., “Syngas Mixture Composition Effect on Flashback and Blowout,” ASME Turbo Expo,2006, DOI: 10.1115/GT2006-90470.

Paschereit,C., Gutmark,E., Schuermans, B., “Performance Enhancement of Gas-Turbine Combustor by Active Control of Fuel Injection and Mixing Process-Theory and Practice, RTO AVT Symposium on Active Control Technology for Enhanced Performance Operational Capabilities of Military Aircraft, Land Vehicles and Sea Vehicles”, RTO AVT Symposium 2000.

Peters, N., Turbulent Combustion. Cambridge [England: Cambridge UP, 2000].

Pope, S. B., Turbulent Flows. Cambridge: Cambridge UP,

Ptasiński, L., Żegleń, T., “Ignition Investigation of Methane-air Mixtures by Multiple Capacitor Discharges.” Journal of Electrostatics, 2001; 51-52: 395-401.

Putnam, A., Jhonson, R., "Application of Dimensionless Numbers to Flash-back and other Combustion Phenomena", Symposium on Combustion and Flame, and Explosion Phenomena 1949; 3:89-98.

Richards, G.A., McMillian, Gemmen, R.S., Rogers, W.A., Cully, S.R., "Issues for Low-Emission, Fuel-flexible Power Systems," Progress in Energy and Combustion Science, 2001; 27:141–169.

Rizk, N.K., Mongia, H.C., "Lean Low NOx Combustion Concept Evaluation,"Twenty-Third Symposium (International) on Combustion/The Combustion Institute, 1990,pp. 1063-1070.

Sato, J., Konishi, K., Okada, H. Niioka, T."Ignition Process of Fuel Spray Injected into High Pressure High Temperature Atmosphere," Symposium (International) on Combustion, 1988; 21: 695-702.

Schefer R.W, "Combustion of Hydrogen-enriched Methane in a Lean Premixed Swirl Burner", Proceedings of the 2001 DOE Hydrogen Program Review, NREL/CP-570-30535.

Shaffer, B., Duan, Z., McDonell, V., "Study of Fuel Composition Effects on Flashback using a Confined Jet Flame Burner", Journal of Engineering for Gas Turbines and Power 2013; 135:011502.1-011502.9.

Som, S., Ramirez, A.I., Hagerdorn, J., Saveliev, A., Aggarwal, S.K. "A numerical and Experimental Study of Counterflow Syngas Flames at Different Pressures", Fuel, 2008; 87:319–334.

Starkey, P., Sidewall, T., Ontko, J., "Investigation of the Effects of Hydrogen Addition on Lean Extinction in a Swirl Stabilized Combustor", Proceedings of the Combustion Institute 2007; 31:3173-3180.

Swaminathan, Nedunchezhian, and K. N. C. Bray,Turbulent Premixed Flames. Cambridge: Cambridge UP, 2011.G

Tabor,G., and H.G. Weller, "Large Eddy Simulation of Premixed Turbulent Combustion Using Xi Flame Surface Wrinkling Model", Flow, Turbulence and Combustion,2004;72:1-28.G

Tacina, K.M., Lee, C.M., Wey, C., NASA Glenn High Pressure Low NOx Emissions Research, NASA/TM—2008-214974.

Tomezak, H., Benelli, G., Carrai, L., Cecchini, D., Investigation of a Gas Turbine Combustor System Fired with Mixtures of Natural Gas and Hydrogen, IFRF combustion journal 2002, 395 ISSN: 1562479X.

UCI Combustion Laboratory, University Of California –Irvine, http://www.ucicl.uci.edu/2/RESEARCHPROJECTS/CombustionScienceResources/TestCells/Index.aspx

Wang,J., Huang,Z., Tang, C., Miao,H., Wang,X., "Numerical Study of the Effect of Hydrogen Addition on Methane–air Mixtures Combustion", International Journal of Hydrogen Energy, 2009;34;1084–1096.

Wang, J., Huang, Z., Tang, C., Zheng, J,. "Effect of Hydrogen Addition on Early Flame Growth of Lean Burn Natural Gas–air Mixtures", International Journal of Hydrogen Energy, 2010;35:7246–7252.

Weinrotter, M., Kopecek, H., Tesch, M., Wintner, E., Lackner, M., winter, F., "Laser ignition of ultra-lean methane/hydrogen/air mixtures at high temperature and pressure." Experimental Thermal and Fluid Science, 2005; 29:569-577.

Whitty, K.Z.,. Zhang, H.R., Eddings, E.G., "Emissions from Syngas Combustion", Combust. Sci. and Tech., 2008; 180: 1117–1136.

Wohl, K.,"Quenching, flashback, blow-off theory and experiment", Symposium on Combustion 1953;4:68-89.

Wu, J., Brown, P., Diakunchak, I., Gulati,A., Lenze, M., Koestlin,B., "Advanced Gas Turbine Combustion System Development for High Hydrogen Fuels", ASME Turbo Expo, 2007;paper no.28337.

York, W.D., Ziminsky W.S., Yilmaz,E., "Development and Testing of a Low NOx Hydrogen Combustion System for Heavy-Duty Gas Turbines," Journal of Engineering for Gas Turbines and Power, 2013; 135: 022001.1-022001.8.

Yousefian, S., Ghafourian, A. , Darbandi, M., "Numerical Study of Syngas Premixed Flame Structure and Extinction", 7th Mediterranean Combustion Symposium,2011.

Zhang, Q., Noble, D.R., Lieuwen,T., "Characterization of Fuel Composition Effects in H2/CO/CH4Mixtures Upon Lean Blowout," Journal of Engineering for Gas Turbine and Power ,2007;129:688-694

Zhang,H., Lilik,J.K., Boehman, A.L. , Haworth, D.C. , "Effects of Hydrogen Addition on NOx Emissions in Hydrogen-Assisted Diesel Combustion," 2009 International Multidimensional Engine Modeling Users Group Meeting Detroit, MI, 2009.

Zhang,Y., Yang,T., Liu,X., Tian,L., Fu,Z., Zhang ,K., "Reduction of Emissions from a Syngas Flame Using Micromixing and Dilution with CO2," Energy Fuel,s 2012;26: 6595−6601.

Zhu, S., Acharya,S., "An Experimental Study of Lean Blowout With Hydrogen-Enriched Fuels", Journal of Engineering for Gas Turbines and Power, 2012 ;134: 041507.1-041507.10.

Vita

Sudipa Sarker received her Bachelor of Science degree in Chemical Engineering and Polymer Science from ShahJalal University of Science and Technology. She earned her Masters of Science degree in Mechanical Engineering in May, 2010 from University of Texas at El Paso. She started the Doctoral program in 2010 in Environmental Science and Engineering program concentrating on the Energy Science and Engineering track at the University of Texas at El Paso (UTEP).

Sudipa Sarker was awarded the University Turbine System Research (UTSR) Fellowship, 2012 by Department of Energy. She was also the recipient of the GAANN Fellowship from the Department of Education in 2013. While pursuing her degrees she worked as a Research Assistant in the NASA Center for Space Exploration Technology Research (cSETR). She also worked with Parker Hannifin Corporation as a UTSR fellow in 2012. She has published her research findings in multiple conference proceedings.